In presenting this dissertation as partial fulfillment of the requirements for an advanced degree at Idaho State University, I agree that the Library shall make it freely available for inspection. I further state that permission to download and/or print my dissertation for scholarly purposes may be granted by the Dean of the Graduate School, Dean of my academic division, or by the University Librarian. It is understood that any copying or publication of this dissertation for financial gain shall not be allowed without my prior written permission.

Signature _____

Date _____

Detection and Identification of Fissionable Materials: A Study in Delayed Neutrons

A dissertation presented

by

Heather A. Seipel

to

The Department of Physics

in partial fulfillment of the requirements

for the degree of

Ph.D.

in the subject of

Applied Physics

Idaho State University

Spring 2016

To the Graduate Faculty:

The members of the committee appointed to examine the dissertation of Heather A. Seipel find it satisfactory and recommend that it be accepted.

Dr. Alan W. Hunt,
Major Advisor

Dr. Daniel Dale,
Committee Member

Dr. Khalid Chouffani,
Committee Member

Dr. Philip Cole,
Committee Member

Dr. Andrew Holland,
Graduate Faculty Representative

For my greatest teacher, my mother. Thank you for never letting me think that there was anything in this world which I couldn't do, so long as I wanted to accomplish it.

And for Edward. Thank you for being such an amazing partner, personally and professionally - you make my world better.

Acknowledgments

I have been blessed in my life with many phenomenal educators and mentors, and I would never have reached the completion of this work without their support and encouragement. I owe specific thanks to a few key people. First, I had a fabulous calculus instructor many years ago, Mac McElfresh, who strongly encouraged me to consider applications of math, such as engineering and physics. I will never understand how he knew that I would so appreciate the mathematics of science, but I will be forever indebted for the path which he set me on - Mac, you were absolutely right. Mark Daily, my first physics instructor, introduced me to the art of problem solving and to what the world of physics could teach me - his courses are what made me want to grow up to be a physicist. Thank you Mark.

Much of my academic interest has focused on experimental research, and the work which I have been able to participate in has shaped my understanding. I owe specific thanks to John Kalivas, who supported undergraduate research efforts, thank you John. I also owe specific thanks to Christoph Boehme at the University of Utah, where I began my graduate career. I learned a great deal about my own research style and about the types of experimental work I would come to love during my time in Christoph's research group, and I would never have been able to gain this at such an early point in my career without his support. Thank you Christoph.

And finally, I come to my time at Idaho State University and in Alan Hunt's research group. It is incredibly challenging to separate guiding the development of understanding and supervising the execution of work during the course of research, and yet my research adviser, Dr. Alan Hunt, managed to achieve this while still allowing me the freedom of finding my own path to discover the answers; I am honored to be joining the ranks of his former students. Thank you Alan, for all of your guidance and for your support.

I have had the true privilege to work with a number of exceptional people during my time at Idaho State University, whose support and expertise contributed to the completion of this work, and to whom I owe sincere thanks. I am particularly grateful to the engineering staff at the Idaho Accelerator Center, especially Chad O'Neill, Kevin Folkman, and Brian Berls, for all of their efforts. I owe considerable thanks to Maxwell Ankrah, for his contributions to the shielded target studies; this campaign

was a compressed time frame and would never have been accomplished without his efforts. I would also like to extend my gratitude to my faculty committee members, Dr. Dan Dale, Dr. Phil Cole, Dr. Khalid Chouffani, and Dr. Andrew Holland, for their support.

I have had a great life during my time at ISU, and I owe much of that to my friends and family; thank you all for your love and for your support. I am especially grateful to my fellow graduate students in Alan Hunt's group. Anna Hoskins, Edward Reedy, Edna Cárdenas, and Ben Satterwhite: you guys ROCK, and I love you all. Anna, instant pudding friend (even though water is all we need to set, we are old enough now to realize that we prefer wine!), thank you for providing a voice of reason and for always being willing to lend a helping hand. Edna, thank you for bringing levity and for never being afraid to ask the right questions; our discussions have given me better perspective and have made me a better researcher.

I spent a final year before the completion of my program in the NNSA Graduate Fellowship Program, detailed to Washington D.C.; this year allowed me incredible opportunities to better organize my 'big picture' perspective and to further my knowledge of nuclear nonproliferation. I would like to extend my sincere gratitude to the NGFP Team at PNNL, especially Jana Fankhauser, Ryan Boscow, and Heidi Hamling, and to my supervisor during my time in D.C., Dr. Marco DiCapua, thank you for the opportunities which you provided. I am also particularly grateful to my colleagues in D.C. for their support and encouragement of my technical development.

Edward Reedy, perhaps last by certainly not least, I owe you an incredible debt. You have been not only a fabulous colleague to work with but the best partner a person could ask for, and it has been a great privilege to work with you. You have incredible talent and experimental insight, and your frankness has always helped to keep me on track. I will be forever grateful for all of your contributions. Thank you for all of your support, but also for always challenging me; you make me strive to be a better person.

Contents

List of Figures

List of Tables

Dissertation advisor
Dr. Alan W. Hunt

Author
Heather A. Seipel

Detection and Identification of Fissionable Materials: A Study in Delayed Neutrons

Abstract

The use of β–decay delayed emissions as distinctive signatures of special nuclear materials has been shown for application to the detection of objects under active inspection. These active inspection techniques utilize a probing source of radiation to induce fission and then monitor for signatures of the inspection material. In this work, a series of experimental campaigns investigated time delayed neutron yield techniques utilizing relatively small fission masses, ∼10-100 grams, to establish detection means and ensure isotopic characterization techniques for low fission mass targets of interest. Experimental studies were undertaken utilizing both aqueous solution targets containing ∼10-100 g ^{238}U and/or ^{232}Th, and silicon oxide targets containing ∼10-100 g ^{238}U and/or ^{232}Th, 2.0 g ^{239}Pu, or 2.73 mg ^{235}U. The measurements were performed in a high background rate environment with limited inspection time in order to assess the feasibility of method application for security considerations such as cargo screening. The experimental work utilized pulsed photofission techniques, where bremsstrahlung photons produced by a pulsed RF LINAC are utilized to induce fission. Inspection times are on the order of several minutes and time delayed neutron analysis techniques will be presented and reviewed; experimental results for the aqueous targets and for the silicon oxide targets will be considered. Consideration of quantifiable detection limits is included, and relevant system detection thresholds including minimal detectable mass are developed for the signature. In addition to the detection of materials, delayed neutrons may be used to provide isotope specificity. Historic analysis methods and experimental results will be considered for delayed neutron lifetime, along with more recently developed dual energy relative yield methods to determine specificity and isotopic ratios for samples which contain two fissionable

isotopes. Having characterized delayed neutron signature suitability for the detection and identification of fissionable materials within this experimental regime, the effects of target shielding on the signature and detection means will then be further investigated. This characterization focuses on experimental studies, and considers the delayed neutron signature as well as the parallel delayed γ-ray signature, where detection is from a target shielded on all sides by the selected shielding configuration; the shielding materials are either borated polyethylene (steps of 5.08 cm up to 30.48 cm) or lead (steps of 5.08 cm up to 20.32 cm). The experimental results for both delayed signature will be considered in detail, and the signature responses compared and contrasted. The delayed γ-ray signature will be shown to be highly complementary to the delayed neutron signature, capable of contributing added confidence to target detection characterization.

Chapter 1

Introduction

1.1 Introduction and Historical Applications of Delayed Neutrons

Efforts have sought to develop or exploit potential signatures of fission as means to address growing concerns regarding national security applications such as securing against the unwanted movement of nuclear materials. Among the many approaches is the development of signatures based on delayed neutrons. Upon inducing fission in a target, a (small) fraction of the fission fragments produced will undergo β-decay and produce additional neutrons on time scales much longer than that of scission. Approximately 0.3% - 5% of fissions result in the emission of delayed neutrons; although only a small fraction of the total fission events, the potential for undesired interferences from non-fissionable isotopes is relatively small, due to the comparatively long time scales involved. This allows one to form a strong detection method for fission using delayed neutrons. Previous studies have demonstrated delayed neutrons to be a robust signature of fission although only a limited number have focused on small mass targets and/or rapid interrogation times for isotope specificity [9–12], the intents of this study.

The end of the 1930's saw the first observations of the emission of time-delayed neutrons which followed the splitting of heavy atoms such as uranium and thorium,

the process now understood to be fission [13, 14]. Intensive study of delayed neutrons as well as the general assimilation of knowledge of the fission process continued for much of the next several decades. As the development and expansion of nuclear energy grew into a fully fledged industry, delayed neutrons played a significant role in reactor technology and design, as they contribute significantly to sustained fission and criticality concerns [15, 16]. Delayed neutron counting as well as total neutron counting became integral aspects of reactor and fuel monitoring techniques as well as nuclear fuel assay methods [11, 17], however, the need for novel applications for delayed neutrons dwindled. In the late 1990's and early 2000's the changing global security environment led to an increased awareness of the need for new technologies to detect potential nuclear threats, including increased safeguards measures to prevent unwanted diversions of materials and improved detection methods to enable greater security against the unwanted transport of materials. Delayed neutrons quickly gained traction within nuclear safeguards and nuclear security communities as a means to address a number of these situations [18–23]. Of specific interest to today's security climate are studies which (1): utilize small masses to investigate the detection thresholds of a system and (2): further examine material identification tools in addition to detection, in order to offer more rapid isotopic composition determination. This work seeks primarily to investigate delayed neutron techniques in low mass fissionable targets in order to better understand detection limits, and to attempt to further develop these rapid isotopic composition techniques.

1.2 Motivations for Detection Needs

There are a number of reasons to motivate further interest in the detection and identification of small mass fissionable targets, but this discussion will be constrained to two primary areas of interest: nuclear safeguards and nuclear forensics.

The framework of safeguards programs, whether through international oversight such as the IAEA or through state overseen domestic policy or facility protocols, generally speaking, all seek to do the same thing: to detect and deter the diversion, misuse, or undesired proliferation of nuclear technologies or materials. The

breadth of concerns spanned within this community is vast, and encompasses everything from specific aspects of facility procedures to global transport or global monitoring concerns. However, there are a number of generalized difficulties of safeguards implementations which may be pointed out. Typically, obtaining accurate and precise fission mass and/or isotopic contribution is a central monitoring desire, although many environmental and procedural requirements complicate this goal, aside from the technological limitations or difficulties faced. Relevant measurements within facilities must often be performed in high radiation environments and may therefore generally require semi-autonomous operations as well as contend with complicating background radiation levels likely to affect instrumentation performance and measurement capabilities. Many facilities, particularly in the application of reprocessing technologies (the U.S. currently has no commercial potential for nuclear fuel reprocessing), process extreme quantities of divertable material – systematic limitations may preclude the immediate or near-immediate detection of unwanted diversions. Reliance on monitoring techniques which require lengthy assay times present a significant and immediate concern. The on-line or continuous monitoring and verification of the fissionable mass in these situations is very desirable, in order to ensure continuity in deterrant systems. However, proven science methods can fail to perform in these environments and thus may not always provide rapid live time or near live time monitoring techniques.

The nuclear forensics community faces many of the same challenges as the safeguards community: the need for increased detection and identification techniques, but for a very different situational context. The primary focus of the nuclear forensics community seeks to identify the composition and therefore determine the history and origin of nuclear materials. This includes analysis of found potentially suspect nuclear material as well as post-detonation analysis needs [24], and often centers on samples with minute quantities of fissionable materials or of fission products. The ability to provide reliable information to decision makers regarding the origin or intended use of any found device, or to provide additional device characterization in a detonation response scenario, is vital to security interests. The time pressures which would exist under such a scenario cannot be overstated, nor can the requirement of certainty in the scientific results. The need for rapid analysis measures, which present

immediate information or serve to confirm subsequent lengthier analysis methods in order to provide greater decision confidence, are clear. Although it is highly unlikely that traditional debris analysis techniques will ever give way to newly purposed approaches such as delayed signature identification, the use of these approaches may prove useful as rough sample characterizations. Even for relatively straightforward sample screening, or binning, alternate methods such as delayed neutron signatures could potentially provide prioritization for much more accurate but dilatory destructive analysis methods, and thereby contribute greatly to the timeline of response and to the broader realm of nuclear forensics.

Attempts to discern information about items with larger amounts of more readily transportable fissile content, such as spent nuclear fuel (SNF) or nuclear warheads, may also be hampered by environmental constraints. Many applications to SNF, including material accountability such as ensuring storage protocols or tracking movement, may be severely hampered by the intense background radiation present, limiting capabilities. Additionally, desireable measurements of the fissile content, to inspect for missing pins or to acquire necessary parameters for reactor burnup calculations, may also be challenged by this background [12,25–27]. Applications to potential items of interest for treaty verification are also of renewed interest, and many potential approaches have been suggested [28–33]. Although nuclear warhead inspection regimes may be challenged, ensuring compliance for an arms control partner's surety would be paramount [34].

Adjacent to the previous nuclear material considerations are the potential ramifications of unauthorized nuclear or radiological material use. The International Atomic Energy Agency (IAEA) established the Incident and Trafficking Database (ITDB) in 1995,

> "to record and analyse incidents of illicit trafficking in nuclear and other radioactive material. It incorporates all incidents in which nuclear and other radioactive material is out of regulatory control."

The IAEA ITDB 2013 Fact Sheet [35] reported that from January 1993 - December 2012, there were a total of 2331 confirmed incidents listed within the ITDB. These

incidents include, for example, "reported theft or loss" of material, and "unauthorized possession and related criminal activities", as well as "unauthorized disposal" or "unauthorized movement" of material. The potential threat(s) presented by the transport of illicit material is clear. The continued need for means of detection to secure against the unwanted transport of materials is crucial to global security. Incidents of theft or illicit transport complicate the geo–political environment within which the framework of security must operate. The need to detect the presence of materials, particularly at borders in order to ensure domestic securities, is paramount to the continuing global security climate. Improved technology to help implement detection measures is currently at the forefront of the nuclear security research community, with many avenues being simultaneously investigated. Increased detection and identification techniques certainly are central to these research paths.

The need for screening methods for freight transport, such as the tens of thousands of intermodal shipping containers which enter the United States each day through numerous sea ports, became a focus of growing public scrutiny of potential U.S. security vulnerabilities. The U.S. Department of Transportation reported more than 110 million metric tons of containerized goods entering the U.S. in the first half of 2009 alone, accounting for more than 9% of all worldwide container traffic as originating in or destined for the U.S. [36]. This potential vulnerability resulted in Congressionally mandated cargo inspection to mitigate the threat [37], and spawned precipitous study and development of technologies which could be deployed to counter this potential nuclear security gap. Achieving inspection of every cargo container entering U.S. seaports thorough enough to detect significant quantities of nuclear material is a daunting prospect (*IAEA standards for significant quantities,* 8 *kg Pu or* 25 *kg* ^{235}*U (HEU)*, [38]). Achieving these inspections in a timely fashion would require established automated systems that rely on sensing the radiation signatures of the nuclear material.

Development of potential methods for national cargo screening systems has had many approaches and is the focus of many continuing research efforts [39–49]. Many challenges emerged as the research approaches evolved. System environments ensure that backgrounds might vary widely across port locations, thus complicating instal-

lation and standard operating procedures, as accounting for these backgrounds could prove critical to establishing accurate detection capabilities. Additionally, environmental factors such as heat or humidity, changing with the weather or seasonally, could have drastic impact on some of the proposed systems; development to field deployability independent or auto-correcting of these effects remains challenging, even at advanced development stages of systems. The technical expertise necessary to understand anomalies in the system and to correctly interpret results can be difficult to automate and may require advanced training; these potential requirements strain the consideration of monitoring personnel, and may require additional resources. Mitigating these effects by implementing larger detector arrays or multiple detector locations in order to maximize the detected signals and reduce the potential for uncertainty in the measured response, that is, to increase the overall probability of a clear source detection, may serve to improve the overall system confidence but is a costly and technically difficult solution. Establishing large area detector arrays can increase the system hardware and signal processing requirements, as well as requiring larger system design footprint and potentially further restricting the transit requirements within the system. A number of large- and full-scale test systems have been constructed to test approaches and capabilities, but a single solution remains elusive. However, since the late 1990's, numerous radiation monitors have been developed for deployment and/or deployed at strategic entry and travel points around the U.S. and abroad, along with radiography inspection systems [50–53], in order to mitigate the risk. Improving material detection capabilities, whether through newly developed systems or improved sophistication of currently deployed systems, remains a current and active point of research. Characterization of the capabilities of developed techniques retains relevance for potential adaptation of historic signatures to the new and continuing detection needs mandated today.

1.3 Active versus Passive Needs

In passive screening systems, naturally occurring decays within the screening target result in radiation which may then be detected. While there may be cases in

which passive detection systems can do quite well [52, 54, 55], even low-level naturally occurring background radiation can prove problematic, often resulting in a high false-positive rate and therefore reducing the potential effectiveness of the system. Fissile materials of interest such as ^{235}U may have an undetectable rate of emission due to very low natural (spontaneous) fission rates, impeding their detection. Additionally, even minimal shielding can effectively defeat the system, mitigating any passive signatures and resulting in a false-negative conclusion, a further undesirable situation.

For an application such as cargo screening, required signal acquisition time has direct impact on commercial goods' transit time and therefore a high potential for economic ramifications. Consideration of the economic impacts on commerce resulting from delays required to accomplish lengthy scans or to resolve potentially anomalous detections predicate rapid inspection. As the detected signal rate may be improved by inducing fission signals in a target, rather than reliance on spontaneous event detection, many approaches utilize radiography beam sources to induce reactions in concealed nuclear material, in order to improve the potential signal rate.

In active interrogation systems, a probing beam of radiation (typically neutrons or photons) is used to induce fission reactions in a target; resultant radiation may then be detected and identified as the signature(s) of fissionable materials. Initial considerations of the cargo screening application led many within the nuclear detection and border security communities to begin to argue in favor of active interrogation systems - passive measurement systems for desired scenarios simply prove too constraining and therefore inadequate. There are potential complications to the use of probing radiation for cargo screening applications, including unintended dose delivery effects to any unknown stowaway passengers; established guidance regulates common practice for active inspection system implementation. (U.S. domestic guidance is governed by the National Council on Radiation Protection (NCRP) [56–58] as well as international guidance by the International Council for Radiation Protection (ICRP) [59–61].) In the U.S., deployed cargo screening systems are operated by (DHS) Customs and Border Protection (CBP); CBP operates radiographic systems to screen potentially suspicious cargo through the Container Security Initiative [62].

Many considerations may go into the design of an active inspection system, including technical details such as type and energy of probing radiation, ideal interrogation or detection distances, or detector system design parameters, as well as potential implementation factors such as operator or environmental dose constraints. Some basic aspects of system design and implementation, such as geometry considerations, were utilized for establishing realizable experimental constraint for this work; however, much of this discussion lies outside the consideration of this project: the goal of this work is to investigate the nature of the basic signatures of fission. The performance of these signatures, even under the basic pertubations of shielding effects considered here, is intended as a means to better understand the signatures themselves, and is not intended as a method to establish an inspection system. Questions of optimal system design and implementation are left to the work of potential intended applications and their specific requirements.

1.4 Results Overview

This dissertation presents the results of several experimental campaigns which have been made on small masses of ^{238}U and ^{232}Th both in aqueous solution and in silica matrix. The purpose of these studies was to investigate the application and adaptation of well known delayed signatures of fission to small mass detection and isotope identification. Understanding quantitatively the threshold of detection is crucial in any detection scheme. The historic concept of minimal detectable level is therefore reviewed in some detail, and adapted to provide a minimal detectable mass which more accurately reflected and incorporated the relevant experimental parameters pertinent to these studies. Critical to this is a detailed discussion of assumed constants and experimental parameters, including a thorough understanding of the background and environmental contributions to the signal. These subtleties will be discussed in Chapter 2: Relevant Theory and touched upon again somewhat in the experimental results sections of Chapter 4.

The experimental results can be further subdivided into two categories which will be considered individually: near geometry results and results at standoff screening

geometry as for cargo-screening-like distances. The first experimental phase sought to investigate details of the delayed neutron signature response of the small mass targets, and thus a very close experimental geometry was used in order to maximize signal. The relevant delayed neutron results, including investigation of potential signal self-absorption and overall delayed neutron yields, will be reviewed first, in Chapter 4. The conclusions as to material detection and material identification techniques, including isotopic identification of a target, will be discussed, and the experimental results considered for a number of fissionable isotope targets.

The second phase of the experimental work investigated the delayed neutron signature in a larger geometry using near cargo-screening distances, in order to assess the methodologies in a more real–world realizable scenario. This experimental work further sought to investigate the effects of target shielding on detection capabilities, seeking to understand how these perturbations affected the overall detection capabilities achievable. A second signature of fission was therefore investigated within this campaign, in order to potentially enhance detection capabilities under these circumstances. A limited discussion to introduce the parallel technique of delayed γ-rays as a signature of fission will thus begin the latter campaign results, Chapter 5. A final discussion of the comprehensive study of signature results under shielded target effects will then be presented for both the delayed neutron and the delayed γ-ray signatures. The simultaneous signature results obtained from this campaign highlights the complimentary nature of these signatures, which will be developed and shown as a culmination of the experimental work.

Chapter 2

Relevant Theory

The relevant signature central to this work, delayed neutrons, are a by-product of fission. Fission may be spontaneous, or it may be induced by excitation either by a γ-ray or through the capture of a particle, provided that the nucleus achieves enough energy to overcome the fission barrier. Following the scission into two fission fragments, the fragments often remain in an excited state and may undergo additional decay processes. If these neutron-rich fission products retain enough energy to overcome the neutron separation barrier, then additional neutrons may be emitted at relatively long times, orders of magnitude longer than the scission event. Appearing milliseconds to tens of seconds after the fission event, these late time neutrons are referred to as delayed neutrons.

2.1 The Fission Process

The process of fission, or the splitting of an atom, typically releases ~ 200 MeV of energy per fission event [63]. This energy is divided among the by–products. A simple graphic, Figure 2.1, depicts a cartoon schematic of the fission process and emitted by–products; the typical pair of fission fragments may be observed along with neutrons and γ-rays. The two fission fragments are sometimes accompanied by an additional light particle (often an alpha particle), a process known as ternary fission and first observed in 1947 [64], which occurs roughly $2-4$ times per 1000 events [65]. This alpha

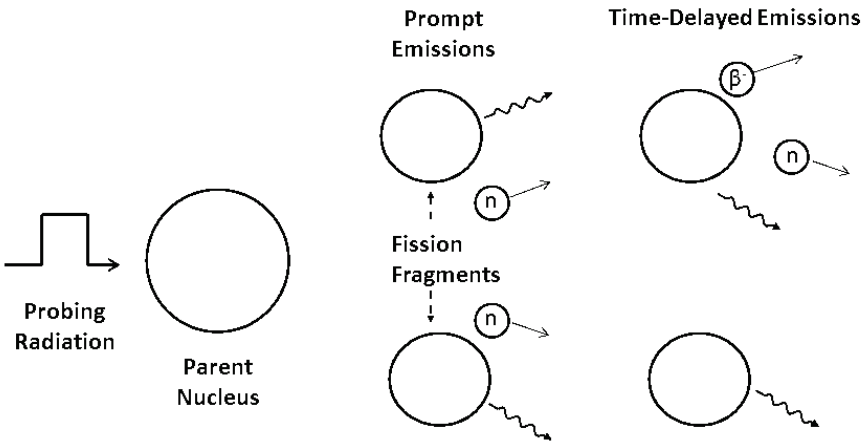

Figure 2.1: A simplified schematic depicting the fission process and characteristic products, as well as typical time–scales of the fission process.

particle reduces the remaining nucleons available to constitute the larger fragments, and alters the kinetics, but otherwise is not inherently different from a standard scission process. Although a statistically rarer process, ternary fission products are accounted for in databases of fission product yields.

A typical scission event on average emits $6-7$ γ-rays per fission event and $2-3$ neutrons per fission event, which come after the fragments are fully accelerated but within $\sim 10^{-14}$ s of the scission, while the fission fragments carry away a great deal of kinetic energy [65, 66]. These initial γ-ray and neutron emissions following fission are typically referred to as prompt emissions. The unstable and energetically excited fission fragments then continue to undergo decay processes in order to shed excess energy as they seek stability. In the case of neutron–rich fragments, the fragments soon reach a point where the only decay path remaining is to undergo β^-–decay, emitting an electron and a neutrino while converting an excess neutron to a proton, ${}^{A}_{Z}\mathrm{N} \rightarrow {}^{A}_{Z+1}\mathrm{N'} + \mathrm{e}^- + \overline{\nu}_\mathrm{e}$. β-decay is a weak nuclear process and thus is inherently a slower process than reactions dominated by strong or electromagnetic forces. The exponential decay of the delayed product precursor determines the time to continued

decay and therefore to any further emissions, but decay constants often range from milliseconds up to tens of seconds for delayed neutron precursors, and can reach to hours, days, or even years for delayed γ-ray precursors. A typical fission event on average emits an additional $6-7$ (delayed) γ-rays per fission while $\sim 0.03-5\%$ of fission events result in an additional (delayed) neutron emission.

Although more complex models have evolved, two relatively simplistic historic models which were developed to describe the fission process remain incredibly informative: the liquid drop model of the fission process, and the shell model. The liquid drop model considers the nucleus as a '*drop*' of viscous material, with properties of a liquid such as volume and surface tension related to the amount of nucleons (A) present in the drop, and additional properties due to the confinement of the nucleons which compose the drop, such as Coulombic repulsion of the protons or symmetry/pairing effects of the nucleons. A semi-empirical formula was developed from the relative contributions of constituent properties [67]. Although the liquid drop model serves to characterize many observed nuclear properties such as nucleon binding energy, and can be used as a tool to understand more complex nuclear reactions, including oscillations resulting in a drop division or scission event, it fails to describe observed complexities of a nuclear structure. Continuing experimental studies historically began to indicate the presence of a much more complicated nuclear shell structure, that is, of various levels inside of the nucleus which could be filled to achieve a much more stable state than that of a partially filled level. These magic numbers of nucleons form the basis for the now-understood nuclear shell model of the nucleus, which serves to further define more complex nuclear processes and has been experimentally confirmed through numerous observations. Although much more sophisticated mathematics are typically used for current theoretic studies, these models still form the fundamental basis of our understanding of the nucleus and of nuclear processes.

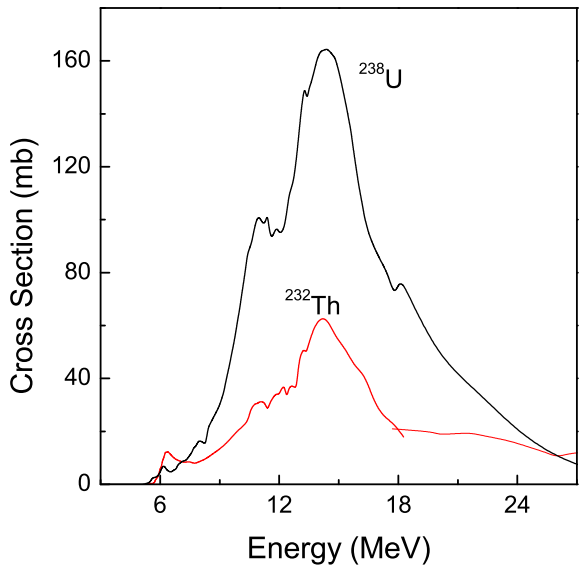

Figure 2.2: The photofission cross section shown for ^{238}U (shown black) and ^{232}Th (shown red), as a function of incident photon energy. The results shown utilize Evaluated Nuclear Data File (ENDF) database results. [1].

2.1.1 Cross Section of the Fission Process

Induced fission is inherently an energy dependent process. The excitation energy available to initiate the fission process is due almost entirely to the incoming particle's kinetic energy. The availability of this energy to excite a fission reaction is directly measurable in the probability of fission, or the cross section of the fission reaction. Cross section is a measure of the statistical likelihood of a reaction to occur; increased cross section means increased probability of a reaction. For fixed experimental conditions (i.e. appropriate target and detection capabilities), this implies that with increasing cross-section, increasing reactions would be observed.

The photofission cross section for two materials of interest, ^{238}U and ^{232}Th, are shown in Figure 2.2 as a function of the energy of the incident photons. Cross section is typically measured in barns, a unit of area which is representative of the cross sectional scattering area of nuclei; a barn is defined as 100 fm^2, approximately the cross sectional area of a large nucleus such as uranium. In Figure 2.2, the photofission cross section appears negligible below ∼6 MeV, indicating the reaction threshhold, or

the minimum incident energy necessary for the reaction to occur. Above this value, the cross section begins to rise for both ^{238}U and ^{232}Th, although the increase is much more significant for the ^{238}U, indicating a much higher reaction probability in uranium as compared to thorium. The photofission cross sections peak for both isotopes near 15 MeV and then begin to fall away. This decreased probability occurs as alternate reactions begin to be more favorable in the materials with increasing photon energy (above 15 MeV), and thus fission is less likely to occur overall. The cross section data shown utilize Evaluated Nuclear Data File (ENDF) database results [1].

2.1.2 Isotopic Uniqueness of Emissions

The process of nuclear fission has been very well-studied and is now understood to be experimentally inducible in many targets using a wide array of probing radiation sources, as well as a spontaneously occurring process observable within some isotopes. Although each fission event is a random event, the overall statistical distribution of the resultant fission products are predictable. This is illustrated in Figure 2.3, which shows the expected fission product yields as a function of the A for the daughter products, given for two fissionable isotopes of interest, ^{238}U and ^{232}Th. The relevant data presented were taken from the Evaluated Nuclear Data Files (ENDF) library records [1]; the high energy neutron fission records were utilized for ^{238}U and ^{232}Th. Relevant photofission product yield libraries do not exist for both ^{232}Th and ^{238}U, and even the neutron induced fission yield libraries are limited. Of the available libraries, thermal energy, fast-pooled, and high-energy neutron fission records, the high energy (14 MeV) neutron induced fission libraries are most representative of the photofission excitation energies utilized for these studies [68]. Ideally neutron induced fission libraries would be utilized for (n,f) of ^{231}Th and ^{237}U as the compound nuclei would then be equivalent to (γ,f) of ^{232}Th and ^{238}U respectively; however, fast pool fission records are unavailable for ^{231}Th and ^{237}U. All fission product yields utilized throughout this work thus refer to the cumulative fission product libraries of the ENDF high energy neutron fission records for ^{238}U and ^{232}Th.

Of significance, the product distributions shown in Figure 2.3 are not only statisti-

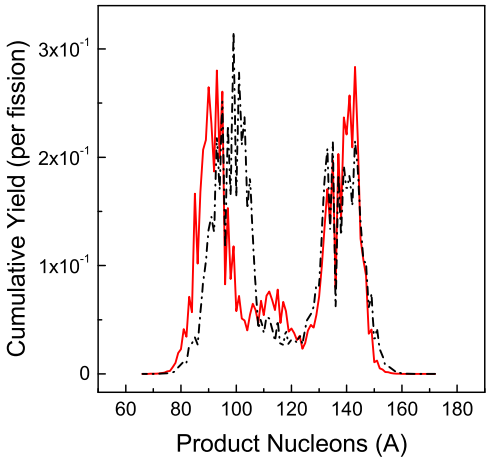

Figure 2.3: The cumulative fission product yield distribution, as a function of the nucleons A of the products, shown for two isotopes, ^{232}Th (red, solid line), and ^{238}U (black, long dash dot line). The data utilized the ENDF cumulative yield records for high energy neutron fission; please see text for further ENDF details and discussion regarding the fission yield library selection.

cally predictable but are unique to each fissioning system, that is, to each parent isotope. This uniqueness of fission yield product distributions (distribution of daughter products) is incredibly paramount. These discretely characterizable differences play a role in the resultant delayed neutron group parameters of the system, and therefore directly impact the capability to identify and distinguish different fissioning systems. As the distribution of daughter products is unique to each fissionable isotope, the distribution of delayed neutrons is thus correlatable. The impact to experimentally observable information about the fissioning system will become apparent in Chapter 4, when these distribution differences are exploited for isotopic identification.

As illustrated by the previous Figure 2.3, the fission process does not typically result in an even 'splitting' into two equal mass nuclei daughter products. Rather, light and heavy product pairs tend to be observed, characterized in Figure 2.3 by the low and high mass peaks. This is due in large part to the influence of the shell structure of the nucleus, although defining an exact nuclear process model which explains the product distribution still remains elusive to theoretical nuclear physics. However, this influence may be overcome with increasing incident particle or probing radiation

energy, resulting in more symmetric fission product pairs. As more energy is available to instigate fission, rarer products tend to be formed, resulting in a filling-in effect in the valley between the observed low- and high-mass peaks; a trend towards more symmetric fragment (distribution) is thus experimentally observed with increasing incident energy [65,66]. These filling-in effects tend to be observed for photofission at relatively large photon energies; the photon energies utilized for these experimental campaigns are low enough that only typical asymmetric fission will occur.

The product distributions illustrate the results of the typical high-mass/low-mass fission product pairs, with a low-mass product centroid and a high-mass product centroid. If, for a number of fissioning systems, the mass centroid values are plotted as a function of the nucleons, A, of the fissioning isotope, Figure 2.4 is obtained. The results in Figure 2.4 indicate (a) the low-mass centroid behavior and (b) the high-mass centroid behavior, as a function of the number of nucleons A of the incident reaction system. It is clear that the low-mass peak centroid varies with increasing A, as indicated in Figure 2.4(a), while the high-mass peak centroid does not have such systematic variance, Figure 2.4(b). This effect is referred to as pinning of the heavy mass peak, and indicates that much of the observable variances utilized to distinguish isotopic information is a direct result of the low-mass fission product distributions. As the heavier fission product distributions remain relatively unchanged for distinct isotopes, extrapolating unique distribution information in this region is much more difficult.

The relative distribution of delayed neutron precursors can be seen in Figure 2.5, which illustrates the delayed neutron precursor distributions for ^{238}U and ^{232}Th as compared to the cumulative fission product yields. The weighted delayed neutron precursor contributions shown were calculated using the values tabulated by Waldo et al. [2,3]. It is apparent that the delayed neutron precursors tend to lie in the peaks of the fragment distributions, and thus the photofission energy dependent region of the valley does not tend to impact the results [69, 70].

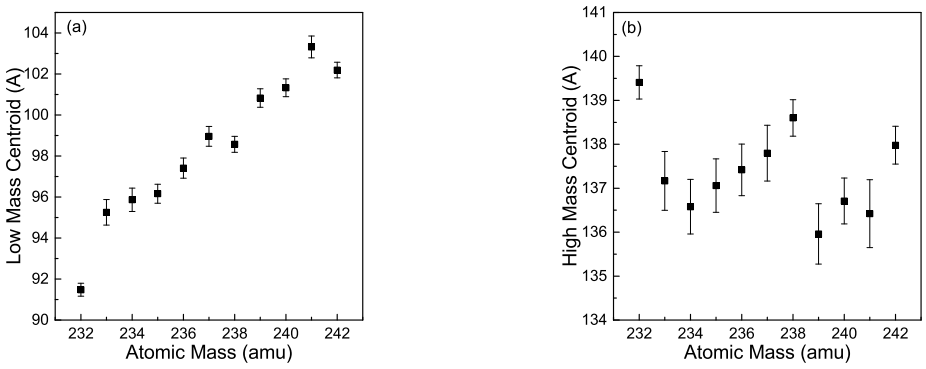

Figure 2.4: The locations of the centroids of the fission product yield distribution, given for a number of fissioning isotopes. The location of (a) the low-mass centroid and (b) the high-mass centroid is shown. The distribution indicates the dependence of the low-mass centroid location on the fissioning (or parent) system; the high-mass centroid location in comparison is scattered, without as tight of a correlation to the fissioning isotope, an effect known as pinning of the high-mass peak. The data utilized was taken from ENDF records [1].

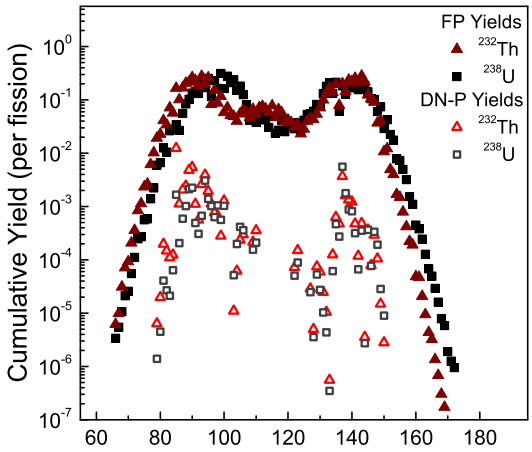

Figure 2.5: The fission product and delayed neutron precursor yield distributions shown for two isotopes of interest, ^{232}Th and ^{238}U. The results utilized ENDF cumulative yield records [1]; the weighted delayed neutron precursor contributions were calculated utilizing the emission probabilities reported by Waldo et al. [2, 3].

2.1.3 Photofission by Bremsstrahlung

Historically, much of the early investigations into the fission process were studied using neutron induced fission. As the field progressed and experimental tools evolved, increasing studies were performed using photon induced fission (photofission) to characterize the fission process [71–73]. Strauch's paper of 1953, a review of much of the field of photonuclear reactions in 1951 and early 1952, including experimental photofission studies, stated that "[t]he majority of experiments concerned with photonuclear reactions are carried out with bremsstrahlung emitted by artificially accelerated electrons." [72]. This utilization of bremsstrahlung continues today.

Bremsstrahlung, derived from the German origins *bremsen*, meaning "to brake" and *Strahlung*, meaning "radiation," thus 'braking radiation,' is the electromagnetic radiation which is produced by the sudden deceleration of a charged particle due to the field of a nearby charged particle, typically an atomic nucleus or an electron. Modern reference to bremsstrahlung tends to often cite the radiation produced by the interactions of electrons slowing within matter; sources of bremsstrahlung may be generated by impinging accelerated electrons against material. In many cases, including the setups utilized for this experimental work, an electron linear accelerator is used for the charged particle source. In this case, the beam of electrons incident on the radiator material results in a forward directed beam of photons (bremsstrahlung) with maximum photon energy equal to the incident electron energy. The fraction of energy which is converted into bremsstrahlung as electrons interact with matter depends upon the electron energy, and increases as the energy decreases; thus a lower energy (fast) electron is more likely to be fully slowed and stopped within a radiator, converting all of its kinetic energy to bremsstrahlung radiation, than a higher-energy electron to which the radiator will appear more transparent. For a mono-energetic electron source energy, a continuous energy spread of bremsstrahlung photons will result, with characteristic shape as for that observed in Figure 2.6, a Monte Carlo calculation of the bremsstrahlung photon distribution obtained from electron parameters similar to those utilized for the experimental campaigns, 16 MeV electrons incident on a 2.18-mm thick tungsten target located 2.54 cm from the electron source. As can

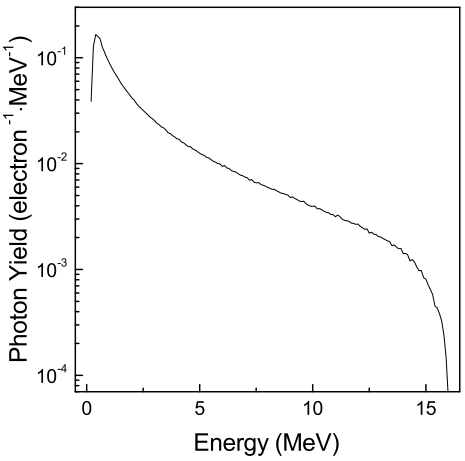

Figure 2.6: Bremsstrahlung energy spectrum, calculated by Monte Carlo simulation of an electron beam incident on a tungsten radiator. Simulations were representative of the experimental setup, and utilized 16 MeV electrons incident on a 2.18-mm thick tungsten target located 2.54 cm from the electron source.

be observed from the simulation results, the yields of the highest high energy photons are orders of magnitude lower than the yields for the lower energy photons, indicating the strong favorability of the bremsstrahlung process to the lower energy photon production. The bremsstrahlung target parameters will strongly influence the resulting photon beam. The bremsstrahlung yield is highly dependent on the radiator material, and is most responsive to materials of high Z which are strongly absorbing of the electrons. To produce a strong yield, the high Z radiator should be thick enough such that a significant fraction of the electrons interact within the material to produce the desired bremsstrahlung photons, but thin enough to allow the bremsstrahlung to pass through the remaining material without significant attenuation, where 'thick' and 'thin' are derived from comparison of the electron path length within the material to the radiator thickness. Radiator requirements may be experimentally constrained; radiator considerations and effects of the resulting bremsstrahlung due to the radiator have been well studied [74, 75]. For the experimental series here, all bremsstrahlung production utilized so-called thick radiators of tungsten; target specifics are covered in the Experimental Overview, Chapter 3.

2.2 Delayed Neutron Production

The emission of delayed neutrons occurs immediately following the β-decay process such that the neutrons may be characterized by the precursors' decay constant. As overcoming the neutron separation barrier requires a fair amount of energy, the emission of a neutron is energetically favorable to the precursor, the immediate daughter of the scission process, as it continues to move towards the valley of stability through decay. To date, more than 271 delayed neutron precursors have been identified [5, 76]. The production of delayed neutrons from all nuclides may be considered explicitly for pulsed irradiations.

2.2.1 Pulsed Production and Decay of Isotopes

To characterize the delayed neutron rates, the decay of isotopes following pulsed production must first be considered. If the production rate of an isotope is defined as $\mathbb{P}$, then the rate of change in the number of isotopes N during the irradiation would be given by

$$\frac{dN}{dt} = \mathbb{P} - \lambda \cdot N, \tag{2.1}$$

where λ is the isotope decay constant. The number of isotopes produced for a single pulse of width t_p may be found by integrating Equation 2.1,

$$N = \frac{\mathbb{P}}{\lambda}(1 - e^{-\lambda t_p}), \tag{2.2}$$

provided that $\mathbb{N}:= 0$ at $t = 0$. The number of isotopes present at time t' measured from the end of the pulse would be given by the decay,

$$N = N_0 e^{-\lambda t'}. \tag{2.3}$$

Substituting that $t = t_p + t'$, the decay may be rewritten as

$$N = N_0 e^{-\lambda \cdot (t - t_p)}, \tag{2.4}$$

or, combining Equations 2.4 and 2.2, the number of isotopes present at time t for a single pulse of width t_p would be given by,

$$N = \frac{\mathbb{P}}{\lambda}(1 - e^{-\lambda t_p}) e^{-\lambda \cdot (t - t_p)}. \tag{2.5}$$

Expanding this result from a single pulse to many pulses, i.e. pulsed irradiation, consider a summation over a large number of pulses η,

$$\mathbb{N}_{total} = \mathbb{N}_1 + \mathbb{N}_2 + \cdots + \mathbb{N}_\eta. \tag{2.6}$$

For an accelerator based production of isotopes where the accelerator is operating with repetition rate or frequency f and time $\Delta t = 1/f$ between pulses, the pulses would occur at times $t_1 = t - (\eta - 1)\Delta t$ (pulse 1), $t_2 = t - (\eta - 2)\Delta t$ (pulse 2), ... , $t_\eta = t$ (pulse η), or, in summation form,

$$\begin{aligned} \mathbb{N} &= \sum_{n=0}^{\eta-1} N(t - n\Delta t) \\ &= \sum_{n=0}^{\eta-1} \frac{\mathbb{P}}{\lambda}(1 - e^{-\lambda t_p})e^{-\lambda\cdot(t - n\Delta t - t_p)}, \end{aligned} \tag{2.7}$$

where the pulse width t_p is assumed to be much much smaller than Δt and the measurement or time t always occurs after some number of pulses and does not begin during a pulse. Considering now the decay following the end of the irradiation period, where time t' is again measured from the end of the last pulse, the total number of isotopes would be,

$$\mathbb{N}(t') = \sum_{n=0}^{\eta-1} \frac{\mathbb{P}}{\lambda}(1 - e^{-\lambda t_p})e^{-\lambda[(t' + (\eta-1)\Delta t) - n\Delta t - t_p]} \tag{2.8}$$

where the time t would be defined as

$$t = t' + (\eta - 1)\Delta t + t_p. \tag{2.9}$$

Reindexing Equation 2.8, the number is,

$$\begin{aligned} \mathbb{N} &= \frac{\mathbb{P}}{\lambda}(1 - e^{-\lambda t_p}) \sum_{n'=0}^{\eta-1} e^{-\lambda(t' + n'\Delta t)} \\ &= \frac{\mathbb{P}}{\lambda}(1 - e^{-\lambda t_p})e^{-\lambda t'} \sum_{n'=0}^{\eta-1} e^{-\lambda n'\Delta t}. \end{aligned} \tag{2.10}$$

A generalized geometric series such as that in Equation 2.10 may be defined as a function,

$$\sum_{n=a}^{b} r^n = \frac{r^a - r^{b+1}}{1 + r}. \tag{2.11}$$

Using $r = e^{-\lambda\Delta t}$ from $a = 0$ to $b = \eta - 1$, the series solution becomes

$$\sum_{n=0}^{\eta-1}(e^{-\lambda\Delta t})^n = \frac{1 - e^{-\lambda\Delta t\cdot\eta}}{1 - e^{-\lambda\Delta t}}, \tag{2.12}$$

and for a large number of pulses, $\eta \gg \lambda\Delta t$,

$$\lim_{\eta\to\infty} \frac{1 - e^{-\lambda\Delta t\cdot\eta}}{1 - e^{-\lambda\Delta t}} = \frac{1}{1 - e^{-\lambda\Delta t}}. \tag{2.13}$$

The expression for the number of isotopes $\mathbb{N}$ present at time t following the end of a pulsed irradiation period is,

$$\mathbb{N}(t) = \frac{\mathbb{P}}{\lambda}\frac{1 - e^{-\lambda t_p}}{1 - e^{-\lambda\Delta t}}e^{-\lambda t}. \tag{2.14}$$

Assuming a very small pulse width t_p as compared to the time between pulses Δt and the half-life, the above equation may be reduced,

$$\mathbb{N}(t) = \frac{\mathbb{P}}{\lambda}\frac{1}{1 - e^{-\lambda\Delta t}}e^{-\lambda t}. \tag{2.15}$$

2.2.2 Delayed Neutron Emission Rates

For the case of delayed neutron precursors, the relevant production rates, $\mathbb{P}$, of Equation 2.14 would be given by the integrated product of the target fission products per fission event and the probability of emission of a delayed neutron for each fission product. The production rate $\mathbb{P}$ for any i-th nuclide due to a fission rate R_F is,

$$\mathbb{P}_i \propto \mathbb{Y}_i R_F, \tag{2.16}$$

where $\mathbb{Y}_i$ is the fission product yield for each i-th nuclide. The probability of the emission of a delayed neutron from any i-th nuclide may be denoted as P_n. The production rate for delayed neutrons from each i-th nuclide explicitly is thus,

$$\mathbb{P}_i = \mathsf{P}_n\mathbb{Y}_i R_F \ . \tag{2.17}$$

The total delayed neutron precursors may be formed by summing the result of Equation 2.14 for pulsed isotope production over all delayed neutron precursors,

$$N_{DN}(t) = \sum_{i:DN} \frac{\mathsf{P}_n\mathbb{Y}_i R_F}{\lambda}\frac{1 - e^{-\lambda t_p}}{1 - e^{-\lambda\Delta t}}e^{-\lambda t}. \tag{2.18}$$

For photofission, the target fission rate is,

$$R = N \int_E \frac{d\Phi}{dE} \sigma(E) dE, \tag{2.19}$$

where N is the number of fissionable atoms in the target, $\sigma(E)$ is the photofission cross–section and $\frac{d\Phi}{dE}$ is the photon flux on the target.

In the case of a target which contains multiple fission isotopes, the total fission rate can be deconvoluted to the sum of the individual isotopic contributions to the fission rate. The fission rate for a target containing multiple isotopes is,

$$R_F = \int_E \frac{d\Phi}{dE} [N_A \sigma_A(E) + N_B \sigma_B(E) + \cdots + N_X \sigma_X(E)] dE, \tag{2.20}$$

given that the target composition is,

$$\tilde{N} = N_A + N_B + \cdots + N_X + N', \tag{2.21}$$

where N' would be the number of atoms of the isotope(s) of the target with negligible fission contribution. The respective number of fission atoms for each target component, N_x, can be found from the fractional target mass m_x for a target of total mass $\mathbb{M}$ using Avogadro's number ($\mathcal{N}_{Avog}$) and the isotopic molar mass (M_x),

$$N_x = \mathcal{N}_{Avog} M_x m_x \quad \ni \quad m_x := f_x \mathbb{M}, \tag{2.22}$$

if f_x is the fractional content of the component. Thus the total target fission rate is,

$$R_F = N_A \int_E \frac{d\Phi}{dE} \sigma_A(E) dE + N_B \int_E \frac{d\Phi}{dE} \sigma_A(E) dE + \cdots + N_X \int_E \frac{d\Phi_X}{dE} \sigma_X(E) dE, \tag{2.23}$$

or,

$$R_F = R_A + R_B + \cdots + R_X, \tag{2.24}$$

the total fission rate in terms of each x-th component's fission rate, R_x.

The expected delayed neutron decay rate, $\mathcal{R}_{DN}$, from any i-th precursor is determined by the precursor decay rate and decay constant and by the corresponding neutron emission probability, P_n,

$$\mathcal{R}^i_{DN} = \frac{dN}{dt} = \lambda^i N^i P^i_n. \tag{2.25}$$

The corresponding neutron emission probabilities, P_n^i, may be found in the literature using experimental data and/or theoretical model predictions [5, 76]. The total expected number of delayed neutrons for a target containing $\mathcal{X}$ different fissionable isotopes can be calculated for any target at time t using the target composition, the fission rate contributions (Equation 2.24), and the individual delayed neutron precursor probabilities of decay,

$$N_{DN}(t) = \sum_{\mathcal{X}:\ {}^{A}_{Z}X} \sum_{i\ :\ DN} \mathbb{Y}_i^{(\mathcal{X})} P_n^i R_F^{(\mathcal{X})} \lambda_i^{-1} \frac{1 - e^{-\lambda_i t_p}}{1 - e^{-\lambda_i \Delta t}} e^{-\lambda_i t}. \tag{2.26}$$

2.3 Delayed Neutron Group Representations

The work of Keepin et al. [4], published in 1957, defined the approach to studies of the time-domain of delayed neutrons. Keepin et al. assumed that the time behavior of delayed neutron emissions could be represented by the linear superposition of a limited number of exponential decay periods, reducing the required number of summation terms from the total number of delayed neutron precursors to just the i representative terms. Through iterative optimization it was determined that six distinct time regions were typically required to reconstruct the time decay of delayed neutron spectra, with each time region constituting a *group*, categorized by decay constant λ and abundance α. It has become conventional to categorize the precursors of delayed neutron emissions based upon their decay process half-lives according to six groups [7, 9], although some work supports more groups [70, 77–80]. The characteristic total delayed neutron precursors can then be described by summing the individual decay groups; the total number of delayed neutrons as a function of time, as Equation 2.18, may instead be represented as,

$$N_{DN}(t) = \sum_{i=1}^{6} \alpha_i e^{-\lambda_i t}, \tag{2.27}$$

where $t = 0$ is the fission event, and in this case the group representation is selected to be six. Each delayed neutron group may be characterized by the dominant precursor or emitter in each time region. Pulsed production and decay response may be

developed for the individual groups utilizing the isotope treatment in Section 2.2.1, resulting in a summation of terms with form as for that of Equation 2.14,

$$N_{DN}(t) = \sum_{i=1}^{6} \frac{\mathbb{P}}{\lambda} \frac{1 - e^{-\lambda t_p}}{1 - e^{-\lambda \Delta t}} \alpha_i e^{-\lambda_i t}. \tag{2.28}$$

2.3.1 Delayed Neutron Groups: Selected Historic Efforts

A number of historic efforts have sought to determine the parameter values for delayed neutron group representation. Early historic efforts utilizing neutron induced fission included those by Keepin et al. [4], largely formalizing the group parameterizations of delayed neutrons, Tuttle [81], Waldo [2, 3], and England and Brady [5, 6], among others. The results of the work of Brady and England built on previous efforts and sought primarily to improve the delayed neutron spectral data for application to nuclear decay libraries; the work was widely impactful and many of the calculated results formed the basis for the delayed neutron information which is incorporated in the ENDF [1] libraries. The group parameter values reported in the work of Brady and England will therefore be considered for reference; however, these results were not reported with associated errors in the measured values and the comparability to the later experimental results is therefore limited. The relevance of the remaining neutron induced fission group parameter values is limited; comparison to results obtained through photofission is much more appropriate. Even if the interrogation energy differs, the compound nucleus state is reflected, e.g. ^{238*}U and not ^{239*}U, and the delayed neutron production is likely to more closely resemble the true experimental distribution, certainly as compared to neutron induced fission. A number of more recent efforts have considered the study of delayed neutron group parameters by photofission, including one of the more detailed efforts by Kinlaw [9] at relevant energies. Additional photofission studies on uranium are relevant as well, including work by Dore et al. at ∼15 MeV [8] and by Kull et al. at 8–10 MeV [7].

Reference values are summarized in Table 2.1 for relevant isotopes ^{238}U, and ^{232}Th; values reported by Keepin et al. for (n, f) [4], by Brady and England for (n, f) [5,6], by Kull et al. for (γ, f) [7], by Doré et al. for (γ, f) [8], and by Kinlaw for (γ, f) [9], are included. This representation of delayed neutrons as groups serves several

purposes, primary of which is that the linearized average emission regions can be used to characterize the time spectra of delayed neutron emissions.

Table 2.1: Summary of historic group parameter values for reference. The values shown are as reported by Keepin et al. [4], by Brady and England [5, 6], by Kull et al. [7], by Doré et al. [8], and by Kinlaw [9], for relevant isotopes ^{238}U and ^{232}Th. The appropriate authors and interrogation techniques are noted.

Isotope	Author Method	Group Number	λ (s^{-1})	α
^{232}Th	Keepin et al. 1957 (n_{fast},f)	1	0.01237 ± 0.00021	0.034 ± 0.002
		2	0.0334 ± 0.0011	0.150 ± 0.005
		3	0.1208 ± 0.0051	0.155 ± 0.021
		4	0.321 ± 0.011	0.446 ± 0.015
		5	1.21 ± 0.090	0.172 ± 0.013
		6	3.29 ± 0.30	0.043 ± 0.006
^{238}U	Keepin et al. 1957 (n_{fast},f)	1	0.01323 ± 0.00033	0.013 ± 0.001
		2	0.03212 ± 0.00058	0.137 ± 0.002
		3	0.1386 ± 0.0053	0.16 ± 0.02
		4	0.359 ± 0.013	0.388 ± 0.012
		5	1.41 ± 0.066	0.225 ± 0.013
		6	4.03 ± 0.21	0.075 ± 0.005
^{232}Th	Brady and England 1989 (n_{HE},f)	1	0.013	0.0326
		2	0.035	0.0997
		3	0.1307	0.1431
		4	0.3274	0.5062
		5	0.9638	0.1336
		6	3.1667	0.0848

continued on next page

Table 2.1 Summary of group parameters, *continued from previous page*

Isotope	Author Method	Group Number	λ (s^{-1})	α
^{238}U	Brady and England 1989 (n_{HE},f)	1	0.0135	0.0195
		2	0.032	0.1184
		3	0.1214	0.149
		4	0.3142	0.3978
		5	0.9109	0.2081
		6	3.0196	0.1072
^{238}U	Kull et al. 1970 (γ,f)	1	0.0126	0.021 ± 0.001
		2	0.0347	0.163 ± 0.001
		3	0.1386	0.167 ± 0.003
		4	0.3465	0.364 ± 0.004
		5	1.155	0.181 ± 0.01
		6	3.465	0.105 ± 0.011
^{238}U	Doré et al. 2006 (γ,f)	1	0.0125 ± 0	0.017 ± 0.002
		2	0.0317 ± 0.0010	0.165 ± 0.005
		3	0.138 ± 0.014	0.183 ± 0.007
		4	0.335 ± 0.023	0.373 ± 0.007
		5	1.19 ± 0.10	0.18 ± 0.004
		6	3.98 ± 0.43	0.085 ± 0.008
^{238}U	Kinlaw 2007 (γ,f)	1	0.0125 ± 0.0001	.0496 ± 0.0007
		2	0.0339 ± 0.0003	0.177 ± 0.002
		3	0.122 ± 0.006	0.19 ± 0.02
		4	0.34 ± 0.01	0.43 ± 0.02
		5	1.6 ± 0.1	0.14 ± 0.005
		6	4.9 ± 0.7	0.011 ± 0.008

continued on next page

Table 2.1 Summary of group parameters, *continued from previous page*

Isotope	Author Method	Group Number	λ (s^{-1})	α
^{238}U	Kinlaw 2007 (γ,f)	1	0.0125 ± 0.0001	0.0170 ± 0.0004
		2	0.0312 ± 0.0002	0.144 ± 0.001
		3	0.122 ± 0.005	0.15 ± 0.01
		4	0.34 ± 0.01	0.418 ± 0.008
		5	1.5 ± 0.06	0.209 ± 0.005
		6	4.4 ± 0.02	0.060 ± 0.006

Table concluded

2.3.2 Linearized Decay Rates

The neutron decay rate is defined by the time derivative of the delayed neutron precursors function,

$$\begin{aligned} R_{DN}(t) &= \frac{dN_{DN}(t)}{dt} \\ &= -\lambda N_{DN}(t). \end{aligned} \tag{2.29}$$

The counts C detected by a system may be found for an emitted signal rate R by integrating over time,

$$C = \epsilon \int R dt, \tag{2.30}$$

where ϵ is the detector efficiency. The total delayed neutron counts obtained for a measurement time of width τ which occurs at time T after the fission event may be found by integrating Equation 2.30; the relevant delayed neutron rates utilizing pulsed production (i.e. pulsed photofission) is defined by Equations 2.29 and 2.14,

$$\begin{aligned} C_{DN} &= \epsilon \mathbb{P} \frac{1 - e^{-\lambda t_p}}{1 - e^{-\lambda \Delta t}} \int_{T-\frac{\tau}{2}}^{T+\frac{\tau}{2}} e^{-\lambda t} dt \\ &= 2\epsilon \mathbb{P} \frac{1 - e^{-\lambda t_p}}{1 - e^{-\lambda \Delta t}} e^{-\lambda T} sinh \frac{\lambda \tau}{2}. \end{aligned} \tag{2.31}$$

Any exponential of this form may be approximated as a linear function on very short time scales as compared to λ^{-1}, thus resulting in a linearized decay rate. The

group parameter representation, as Equation 2.27, may also be utilized; the previous equation for the expected delayed neutron counts is then simply,

$$C_{DN} = 2\epsilon\mathbb{P}\sum_{i=1}^{6}\frac{1-e^{-\lambda_i t_p}}{1-e^{-\lambda_i \Delta t}}e^{-\lambda_i T}sinh\frac{\lambda_i \tau}{2}. \tag{2.32}$$

In the case of group representation, a sum of linearized decay rates results, according to the time scale of each group.

This result for the detected counts may be normalized to the initial emissions, resulting in a common y-intercept of 1 and removing the dependency of the detector efficiency,

$$\frac{dC_{DN}}{dt} = \sum_{i=1}^{6}\frac{1-e^{-\lambda_i t_p}}{1-e^{-\lambda_i \Delta t}}\cdot\alpha_i\lambda_i e^{-\lambda_i T}sinh(\frac{\lambda_i \tau}{2}). \tag{2.33}$$

where the minus sign resulting from the derivative has been suppressed as the results are understood to be a decay. The expected signal response decay rate for the delayed neutron emissions may thus be found for any isotope from the time behavior of the precursors. Experimental measurements of the delayed neutron decay rates for materials of interest will be discussed in the results section, and contrasted to the predicted decay rates utilizing delayed neutron group parameters.

In a mixed target where two isotopes are present, the total delayed neutron decay rate may be developed from the constituent linearized decay rates. If the fraction f of the total mass is defined for one of the components, then the mixed target decay rate would be found from the contributions of each component, given by,

$$\lambda_{mix}(f_1) = \frac{f_1\lambda_1^2 C_1 + (1-f_1)\lambda_1^2 C_2}{f_1\lambda_1 C_1 + (1-f_1)\lambda_2 C_2}\ , \tag{2.34}$$

where the C-values indicate calibration factors which relate the measured response of each isotope to the amount of the isotope which is present; these values may be obtained experimentally and will be discussed in the results sections.

Beyond two components this constituent composition approach becomes excessively difficult to fit, and the results are unreliable. However, if further sample knowledge is available or systematics can provide a route to better sample characterization, i.e. a third component exists in the the sample but the isotopic content can be pinned

to the concentration of one of the two previous components, then the approach may be applicable. As with any data fitting methodology, an increase in the free parameters which can be fit heightens the risk of inaccuracies in the result.

2.3.3 Derivation of Dual Energy Relative Yield (DERY), an Alternative to Linearized Decay Rate

In addition to considering the differences in the rates of delayed neutron emissions for potential isotopic specificity of materials, consideration of the differences which may arise at distinct interrogation energies may also be made. Specifically, it can be seen from Figure 2.2 that the photofission cross sections of ^{232}Th and ^{238}U not only vary with energy but are considerably different from each other. The target fission rate given by Equation 2.19 represents these differences when considered for two different fissioning isotopes, or for the same fission isotope utilizing two distinct photon flux distributions. If a material is considered at two distinct interogation energies, the ratio of the signature responses may be considered. This Dual Energy Relative value would simply be,

$$D = \frac{S_{E1}}{S_{E2}}, \tag{2.35}$$

where the signal response S is measured at two distinct energies *E1* and *E2*. If delayed neutron emissions are considered, then the Dual Energy representation would become,

$$D = \frac{R_{DN}(t, E_1)}{R_{DN}(t, E_2)}. \tag{2.36}$$

The photofission fragment yield distributions may be considered to be approximately equal within the bremsstrahlung beam energy region of interest. In reality, the distributions are unlikely to be exactly equal at distinct interrogating photon energies; given the limited fragment yield libraries available this is however a reasonable approximation. From Equation 2.26 it follows that the fission rate, R_F, which changes with the distinct bremsstrahlung energies directly effects the delayed neutron emission rate. Thus the Dual Energy Relative value becomes,

$$D \propto \frac{R_F(E_1)}{R_F(E_1)}, \tag{2.37}$$

directly dependent on the distinct fission rate responses. However, the photofission fragment yield distributions are unlikely to be exactly equal at distinct interrogating photon energies.

2.3.4 Optimal Repetition Rate

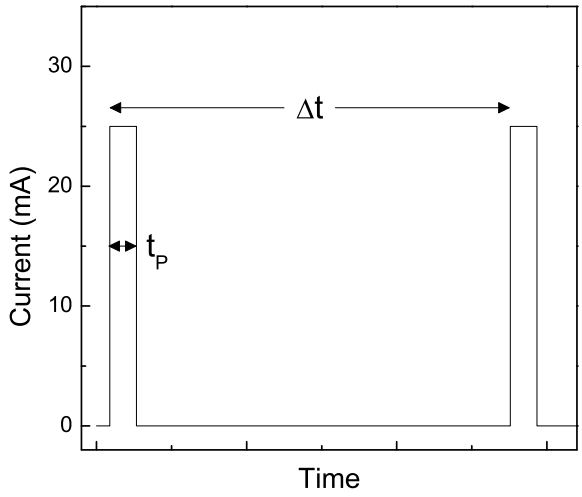

Figure 2.7: A pulsed interrogation timing schematic, where *t=0* marks the arrival of the probing radiation which induces fission in the target. Data is then acquired between pulses. The length of time between interrogation pulses is determined by the repetition rate of the system, and the arrival of the next pulse marks the end of the acquisition time window.

In pulsed interrogation systems, fission is induced in the target of interest and the time window available to measure the resultant decay products is determined by the length of time between accelerator pulses, which is simply the inverse of the system repetition rate, Figure 2.7. To form the delayed neutron signal a portion of the early time response may be removed from the data, as these neutron responses are not strictly delayed neutrons; this reduces the length of the acquisition time of the desired (delayed neutron) signal. It is of course desirable to optimize the collected signal with respect to the production window.

If the net signal count, η_S, obtained is (by definition) the difference between a measurement of an unknown target of interest, η_U, and a background sample, η_B,

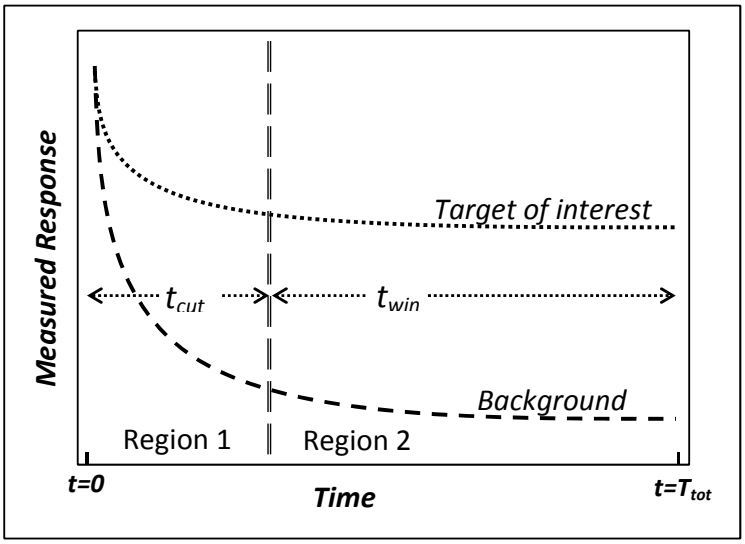

Figure 2.8: The measured response illustrated for a target of interest and a background. Two distinct time regions, Region 1 and Region 2 are defined, with corresponding times t_{cut} and t_{win}, respectively, and the total time T given by their sum.

then the error in the signal rate is defined as,

$$\sigma_{SR} = \sqrt{(\sigma_{UR})^2 + (\sigma_{BR})^2} \ , \tag{2.38}$$

where the rate is simply the detected number of counts divided by the acquisition time. The error of the rate would be related to the square root of the number of counts, i.e. the error in the unknown target rate would be given by,

$$\sigma_{UR} = \sqrt{\eta_U}/T. \tag{2.39}$$

If two distinct time regions of interest are defined, as Figure 2.8, then the error in the net signal measured in the late time region of interest (t_{win}) would be given as,

$$\sigma_{SR_{R2}} = \sqrt{\frac{U_{R2}t_{win}}{T^2} + \frac{B_{R2}t_{win}}{T^2}} \ , \tag{2.40}$$

where the relative rate has been defined to be approximately constant for each target within the region of interest, i.e. U_{R2} for the unknown target in *Region 2*, $\eta_{U_{R2}} = U_{R2} \cdot t_{win}$, and the total time is the given by the sum $T = t_{cut} + t_{win}$. To optimize the detection parameters, the signal rate variance is then minimized with respect to time; taking the derivative as a function of time, it can be shown that,

$$t_{win} = \frac{1}{2} T_{tot} \tag{2.41}$$

as the optimal operating conditions. The selected accelerator repetition rate will be further discussed in the experimental results.

2.4 Minimal Detectable Mass

Establishing the minimal sensitivity of the detection method would be very useful. Historically, such detection limits of a system are established through the development of "*minimum detectable levels*," the statistically measurable detection thresholds of a system [82, 83]. L.A. Currie [82, 84] formalized much of the methodology and terminology for establishing the statistically reliable detection limits of activity by a measurement system, agnostic of the technology, as determined by the associated mathematics and statistics of signal counting; a thorough review of this work is strongly recommended to the reader for further study, as it forms the basis for the development and treatment of the minimal detectability of targets for the remainder of these experimental studies.

It is standard to consider any assessment of detection as the capability to distinguish between the desirable signature over that of the background signal. To identify the potential for detection success, the crucial capability then becomes in establishing the level at which this comparison is no longer meaningful; that is, at what signal level is it no longer reasonable to compare the two measurements with confidence in the result? The approach of L.A. Currie (and others) is first to define the detection level in terms of this critical decision level. A similar approach follows here, which will be expanded to the application of this methodology in later discussion regarding

experimental results.

2.4.1 Quantitative Detection Limits

It is assumed that a Gaussian is sufficient to describe the distribution of the measured responses, i.e. that there is sufficient acquisition time to obtain a high number of counts and thus to form a statistically strong signal basis. For any given detection system, the net signal (i.e. counts) is defined as the difference between the gross signal measured from a target of interest and a companion background signal,

$$\eta_{net} = \eta_g - \eta_{bkg}, \tag{2.42}$$

and the associated error or standard deviation in this measurement would be given by,

$$\sigma_{net} = \sqrt{(\sigma_g)^2 + (\sigma_{bkg})^2}, \tag{2.43}$$

where the standard deviation of the measured gross and background values derive directly from the data. The background signal may contain both active inspection and passive rate contributions. Paired measurement conditions which assume that an active background measurement is obtained for each target of interest are relevant to these studies, and may be assumed for defining the detection limits.

Figure 2.9 illustrates the expected Gaussian probability distribution where the distribution is shown centered at zero, as for the case where no material is present in the system and the net signal would on average be zero. The net signal may be compared to a selected decision level, indicated in the shown distribution figure as the *critical level*, L_C; a net signal value greater than the critical level indicates a positive conclusion. For the case illustrated, where no material is present in the system and the background measurement is therefore equivalent to the gross measurement, the standard deviation in the net signal reduces to,

$$\sigma'_{net} = \sigma_0 = \sqrt{2\sigma^2_{bkg}}\ , \tag{2.44}$$

a function of the error in the companion background measurement which is attributable to the statistical deviations of the measurement. As there is no true signal

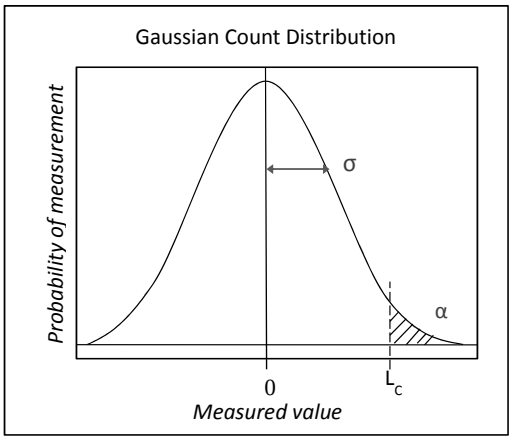

Figure 2.9: A gaussian distribution of measured responses where the distribution shown is centered at zero, which represents the case where no material is present in the system and the net signal measured would on average be zero.

present in the system for this case, any detection of a net signal above the critical level would represent a false positive. Clearly the critical level needs to be selected such that the false positive occurrence rate is low. Using standard Gaussian distribution statistics, it is given that only 10% of measurements will lie outside of 1.64σ. As this is a symmetric distribution about zero, only 5% of all measurements would represent a false positive detection. The α-value of the system, the false positive tolerance, is thus defined to be 0.05 in this case, which is often a standard selection. The abscissa of the probability distribution, $1 - \alpha$, or for α =0.05, 1.64, is commonly noted as k_α; α is indicated as the integrated area under the distribution curve in Figure 2.9. Note that only the tolerance for false positive detection rates and the standard deviation of the measurement with a true value of zero is needed to construct the critical level,

$$L_C = k_\alpha \sigma_0, \tag{2.45}$$

where for paired measurements the standard deviation reduces to $\sigma_0 = \sqrt{2\sigma_{bkg}^2}$, as in Equation 2.44.

In parallel to the definition of the allowable false positive detection rate of the

system, a false negative tolerance rate needs to be defined. This value, β, is the tolerance of a missed threat which is incorporated into the system. The a priori detection limit, L_D, of the system may then be defined as,

$$L_D = L_C + k_\beta \sigma_{net}, \tag{2.46}$$

where the abscissa of the distribution k_β corresponds to the $1-\beta$ probability, again where β is the false negative system tolerance. The tolerance values are often selected such that $\alpha = \beta$ in order to form symmetric false positive and false negative detection tolerances within a system, but will still be treated explicitly here.

The detection limit L_D represents the minimal detectable value of the system. There are two principle measurement cases of import, the null signal with variance σ_0 which has been utilized to define L_C, and the gross signal which is just equal to the detection limit L_D. The error in the net signal at this detection limit would be,

$$\begin{aligned} \sigma_{net}^2 &= \sigma_g^2 + \sigma_{bkg}^2 \ , \\ &= L_D + \sigma_{bkg}^2. \end{aligned} \tag{2.47}$$

The detection limit as defined by Equation 2.46 in this case becomes,

$$\begin{aligned} L_D &= L_C + k_\beta \sigma_{net}, \\ &= L_C + k_\beta \sqrt{(L_D + \sigma_{bkg})}. \end{aligned} \tag{2.48}$$

Solving the preceding two equations yields the detection limit,

$$L_D = L_C + \frac{k_\beta^2}{2}\left[1 + \left(1 + \frac{4L_C}{k_\beta^2} + \frac{4L_C^2}{k_\alpha^2 k_\beta^2}\right)^{1/2}\right] \ , \tag{2.49}$$

$$L_C = k_\alpha \sigma_0. \tag{2.50}$$

If symmetric false tolerances are defined, $k = k_\alpha = k_\beta$, under paired measurements the previous results may be reduced,

$$L_D = 2L_C + k^2, \tag{2.51}$$

$$L_C = k\sqrt{2}\sigma_{bkg}. \tag{2.52}$$

2.4.2 Defining Minimal Detectable Mass

The detection limit discussion to this point has considered the ability to identify detection limits for generic counting systems; the relevant intended experimental signature of interest however concerns yield, and not counts. The previous result of L.A. Currie for paired measurements with symmetric false tolerances which is given by Equation 2.51 needs to be adapted to incorporate normalization factors appropriate to the yield results for active interrogation measurements. Unlike many traditional counting systems, an active interrogation application requires consideration of the effects of the interrogation aspects of the measurement. In order to arrive at an appropriate and logical result, the results need to be normalized to account for changes in the induced rate of the signature; in the case of photofission, the total bremsstrahlung flux on target would be an appropriate normalization factor, as the rate of fission would scale directly with this. Selecting appropriate active interrogation parameters for measurements and assuming that measurements are made with corresponding backgrounds, i.e. paired measurement conditions, the critical limit and the corresponding detection limit terms will be scaled by the normalization factor,

$$L_D = \frac{k^2}{\phi} + 2\sqrt{2}k\frac{\sigma_B}{\phi} \ , \tag{2.53}$$

where ϕ is the calculated normalization factor which accounts for the signature response to the active inspection. An unknown target mass may be extracted for a given measured response, S, given an experimentally determined relation between the measured response and the mass. For the case where the net signal is just equal to the detection limit and a linear relation occurs between the measured response and the fissionable mass, the minimal detectable mass would be defined as,

$$\begin{aligned} m_{min} &= \left(\frac{dS}{dm}\right)^{-1} [L_D] \\ &= \left(\frac{ds}{dm}\right)^{-1} \left[\frac{k^2}{\phi} + 2\sqrt{2}k\sigma_B\right] \ . \end{aligned} \tag{2.54}$$

It is significant to note that the minimal detectable mass depends only upon the fluctuations in the background. This is a logical outcome, as the environmental

conditions should indeed dictate the system's detection limits. A very well-known system with low background and minimal deviations in the background signatures would be expected to have a much lower minimal detectable mass than a system with very high background levels and much higher deviations; the background within a system environment directly affects the capability of the system to detect extremely small masses of interest.

2.5 Neutrons: Interactions and Detection

The primary factor which dominates neutron interactions is the energy of the neutron. For this discussion, the incident neutron energy may be divided into several principle regions of interest: thermal/epi–thermal neutrons (energy 0.025-$\sim$0.5 eV), slow neutrons (energy $1-100$ eV) and fast neutrons (energy >1 MeV); neutrons with energy which lies between the slow and fast energy regions are simply characterized as intermediate energy neutrons. Further characteristic neutron energy subdivision may often be seen, particularly with respect to specific applications such as nuclear reactor criticality calculations, and the exact energy ranges often vary among references and application; the somewhat simplified principle energy regions will suffice for the purpose of this discussion. Interactions for neutrons with low energies, including thermal and slow neutrons, are limited to scattering and neutron–induced reactions. Scattering serves as a primary interaction of neutrons with matter. Typically, as neutrons interact within a material, multiple scattering events take place within a very short time window, typically microseconds – milliseconds, resulting in the loss of much of the energy of the neutron, a process known as thermalization [16, 85]. With increasing kinetic energy, the neutron scattering probability decreases. This relation is observed below ~ 1 keV as scattering $\propto v^{-1}$, an inverse relation to the velocity of the neutron; this is illustrated in Figure 2.10 which shows the total neutron scattering and absorption cross section for a neutron on hydrogen nucleus (^{1}H(n,*) reaction). However, for high-energy or fast neutrons, when scattering does occur, although much less probable, the significance is therefore greatly increased, as the neutron is able to impart much more kinetic energy to a scattering center. Hence, the neutron is slowed

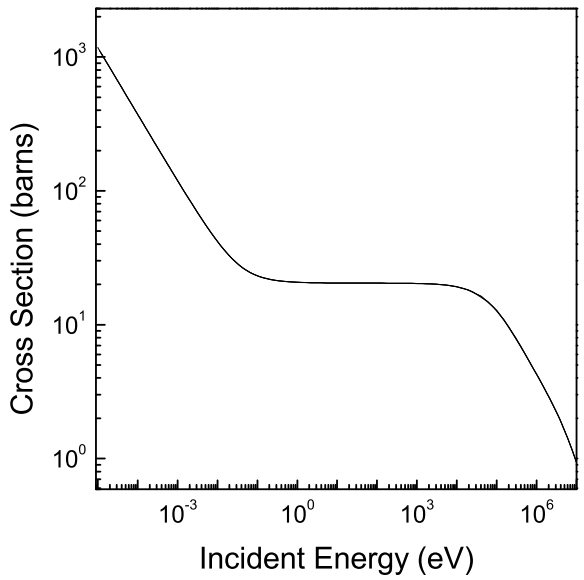

Figure 2.10: Neutron scattering cross-section for hydrogen.

significantly, or *moderated*, by these scatterings to lower energies. The most effective moderators of high-energy neutrons contain great deals of hydrogenous materials, as a single collision of a neutron with a hydrogen nucleus can result in the total loss of the neutron kinetic energy. Conversely, increasing atomic number in a scattering target implies a neutron is unable to impart as much kinetic energy in a collision and more collisions are required to thermalize or slow a neutron. These effects play a significant role in shielding considerations of neutron emissions: a thin layer of material of very low atomic number may result in very effective scatterings of a neutron, thus slowing it significantly and challenging detectability, while scattering events in even a thicker layer of material of higher atomic number will have less impact on the neutron kinetic energy and therefore on the detectability of the neutron. The resulting subtleties of these shielding considerations for neutrons will be considered in depth in Chapter 5 where shielded target results will be presented.

The initial development of theories and calculations on neutron scattering and neutron slowing down effects were first reported in the early 1930's and included significant contributions by Bonner [86], Fermi (and Amaldi) [87–89], Dunning and Pegram [90, 91], and Breit and Wigner [92], among others. Many of the early prin-

ciples of neutron slowing down effects first discussed in the 1930's survive today, incorporating more sophisticated mathematics and advances in understanding, and now include the study of slow neutrons, neutron thermalization effects, and slow neutron interactions/effects on matter.

The more significant contributors to neutron detection are induced nuclear reactions [83], such as (n,γ), (n,p), (n,α), or (n,*f*) reactions, which subsequently produce particles that are much more readily detected. Often, (n,γ) reactions are undesirable detection schemes for neutron identification due to the difficulties associated with distinguishing the resultant γ-rays. However, the production of heavier charged particles is often much more easily detected. A huge advantage of neutron detection through secondary reactions is the relation of rapidly increasing neutron capture cross–section to the neutron energy decrease as the neutron slows, since scattering scales as $\propto \frac{1}{v}$. This fact is illustrated by Figure 2.11 which shows the total neutron scattering cross-section as a function of incident energy, for several materials commonly used in neutron secondary reaction detection, including ^{3}He and ^{7}Li, as well as for ^{1}H and ^{208}Pb, for comparison. In all cases, we may readily see that the cross–section falls rapidly with increasing kinetic energy, until we begin to observe resonances above $\sim$ 1 keV [66]. The significance of these resonances is outside the scope of this work; it suffices to state that these sharp resonance peaks are discrete and characteristic, and are indicative of the nuclear structure.

The body of the experimental work of this project relies on the reaction $^{3}\mathrm{He}(\mathrm{n},\mathrm{p})^{3}\mathrm{H}$ for detection, and so the remainder of our discussion of secondary reaction neutron detection will focus on this; however, the underlying principle is the same for any charged particle detection and may thus be adapted accordingly. In the case of ^{3}He a neutron interacts with the nucleus producing a proton and a triton pair, which may then be detected, as for any charged particle pair, in a proportional counter.

Proportional counters are gas–filled tubes which rely on the effects of gas multiplication in order to amplify an incident particle charge to a detectable electronic signal. A high electric field is applied to the gas within the tube, serving to create drift of any charged particles to their respective electrodes. As the charged particle drifts within the electric field, it collides with surrounding gas molecules. If the particle has suffi-

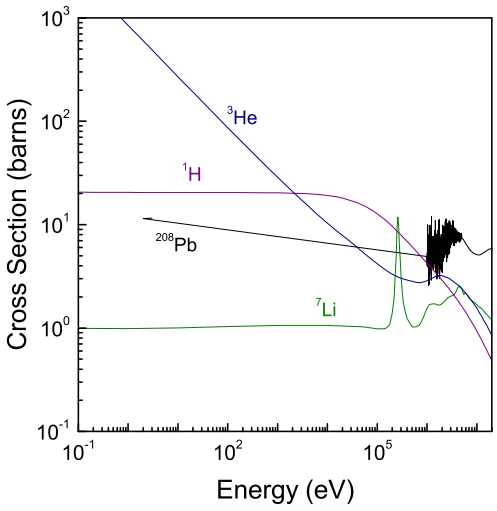

Figure 2.11: Total neutron scattering cross-section shown for several materials of interest, ^{1}H, ^{3}He, ^{7}Li, and ^{208}Pb.

cient energy it can further ionize additional gas molecules upon collision, introducing further charges into the system and thus increasing the overall electric response at the electrode. Further, charged particle energy will increase between collisions in relation to the applied electric field strength. There is therefore a minimum threshold field energy for these secondary ionization to occur, above which an avalanche effect occurs, the Townsend avalanche effect. Shown in Figure 2.12 is the pulse amplitude response as a function of applied voltage for a generic (theoretical) gas–filled detector. The response may be easily subdivided into six regions, as is standard for most discussions of gas–filled detectors [83]. The first region illustrates an applied field that is insufficient to cause the desired drift, where the ion pair simply recombines, while with slightly increased field, region II, this effect is suppressed and ionization occurs. As applied field increases, region III, the gas multiplication effect dominates, and the charge collected is (linearly) proportional to the incident charge deposited in the detector. This is the typical operating region of proportional detectors. Under continued increase of applied field, region IV, the linearity of the proportional charge effect is lost, although the detected response is still amplified in relation to the incident charge. Above this, region V, the response is self-limiting and no longer proportional to incident charge, or is a continuous discharge region, region VI, where

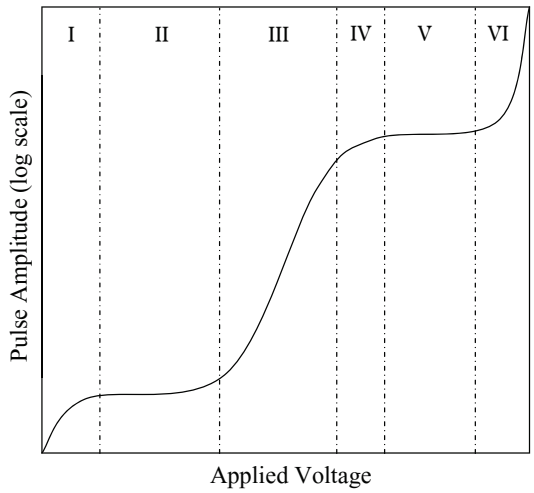

Figure 2.12: Generic Proportional Detector Regions

no useful information is obtained and in fact damage to the detector may occur.

The principle conclusions to neutron scattering effects include (1) the impact of multiple scatters of a neutron on its energy, a process resulting in the thermalization of the neutron, that is as it repeatedly scatters, losing energy, it reaches thermal (and therefore kinetic) equilibrium with surrounding matter, (2) the interaction of thermal neutrons with matter, which results in (3) capture or secondary nuclear reactions which may be subsequently used for detection. The lifetime of free neutrons is therefore limited, before decay to a proton, with accompanying β and anti–neutrino emissions, occurs. In air, where the probability of scattering is greatly diminished, this results in a lifetime of $\sim$ 10.6 minutes [66], while bound neutron lifetimes may be longer or even stable [66]. As a result, free neutrons play an often negligible role in detection, but pertinent timing details will be discussed in the experimental results.

Chapter 3

Experimental Overview

The experimental campaigns sought first and foremost to identify the basic signature responses for the low-mass targets, and to characterize detection capabilities potentially based on these signatures. Later phases of the project would investigate the signature(s) in more real-world scenarios such as cargo-screening-like configurations, some of the results of which will be presented in Chapter 5, Shielded Target Investigations: Delayed Neutrons plus Delayed γ-Rays, Companion Signatures.

3.1 Experimental Geometry I

The fission reactions and competing secondary reactions were induced by bremsstrahlung photons. The bremsstrahlung beam was produced using a variable frequency pulsed linear electron accelerator with a 4 μs pulse width, and experimental end point energy adjusted from $\sim$ 7 MeV to 19 MeV. Electrons exited the end of the beam line and impinged on a 4.2 g·cm^{-2} thick tungsten radiator. A 5.08 cm thick aluminum scrubber was selected and placed immediately following the radiator, in order to attenuate the photons and thus reduce the flux of undesirable very low-energy photons in the interrogation targets, as well as to ensure conversion of any electrons which escaped the radiator. The resultant uncollimated photon beam was used to interrogate the targets, which were placed 33.0 cm directly downstream from the tungsten radiator.

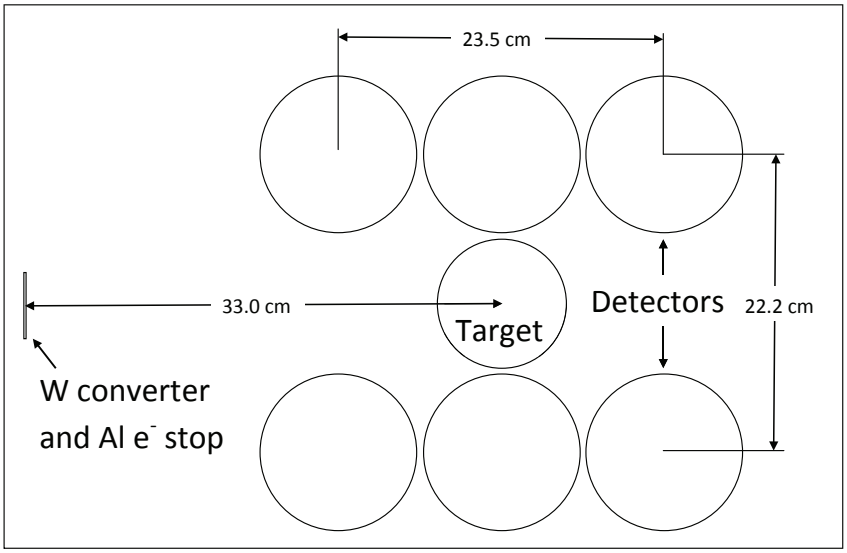

Figure 3.1: An overhead view of the delayed neutron signature experimental geometry. A very tight detector configuration was used in order to maximize the detected signal.

In the initial studies, a very tight geometry was employed in order to ascertain the greatest amount of detector response information. The experimental setup is summarized in the schematic shown in Figure 3.1. A set of six moderated ^{3}He neutron detectors (MHNDs) were arrayed around the interrogation target, with three detectors placed to either side of the target at a distance of 11.1 cm from target center to detector center. The general principles of neutron detectors were discussed in detail in Chapter 2. This series of six MHNDs each consisted of a 10 atm ^{3}He tube measuring 2.36 cm in diameter and 20.32 cm in active length, encased in three types of materials for moderation; the innermost moderation layer was 2.54 cm of virgin polyethylene, surrounded by a total of 15.85 mm of doped borated rubber, alternated between layers of cadmium, 0.22 cm in total thickness, which served to screen already thermalized neutrons from active detection. A detailed construction description and schematic of the detector may be found in M.T. Kinlaw's 2007 Ph.D. dissertation [9].

3.2 Signal Timing Parameters

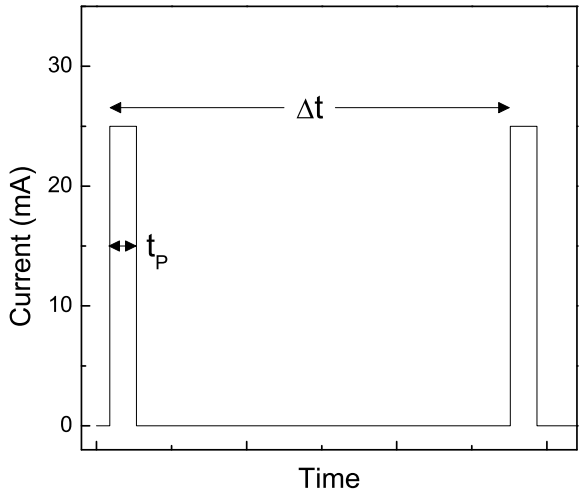

Figure 3.2: The experimental timing schematic, where *t=0* marks the accelerator gun pulse trigger. Data was acquired between accelerator pulses. The length of time between accelerator pulses is determined by the repetition rate of the accelerator; the arrival of the next pulse marks the end of the time window.

Neutron time spectra were collected using a multi-parameter data acquisition system. Results were recorded between photon pulses and summed over many accelerator pulses. A view of the timing schematics is shown in Figure 3.2. A latched scalar start was triggered by a signal corresponding to the electron gun pulse, and subsequent detector responses were recorded in time-adjustable bins, with bin-width determined by desired experimental parameters such as the accelerator repetition rate and the desired count time between pulses. The majority of the experiments were conducted at an accelerator repetition rate of 15 Hz with a scalar bin-width equal to 32 μs per channel over 2048 channels, resulting in a total time spectra width of 65.5 ms, just less than the 66.67 ms interval between photon pulses.

3.3 Experimental Targets

The series of low-mass aqueous targets were created by dissolving actinide salts in water, either uranyl nitrate or thorium nitrate, or a combination thereof, in order to achieve the desired actinide mass targets. A total of six aqueous pure uranium targets and six aqueous pure thorium targets were created, as well as four mixed aqueous targets which contained both thorium and uranium. Relevant target information is summarized in Table 3.1 (end of chapter), including target labels, fissionable mass content and concentrations. In addition to the aqueous targets, a series of low-mass oxide matrix targets were created by mixing uranium oxide and thorium oxide with sand (silicon dioxide) to produce a similar series of sand or oxide targets. In similar fashion to the aqueous targets, six pure uranium targets and six pure thorium targets were created, as well as four mixed oxide targets which contained both thorium and uranium content. The oxide target information is summarized in Table 3.2 (end of chapter), including target labels, fissionable mass content and concentrations. Note that the oxide targets provide a slightly wider mass range for consideration, as compared to the aqueous targets.

It is worthwhile to note that several general issues were observed with the targets throughout the experimental campaigns. First, there was some experimental inconsistencies with target measurements which were determined to be attributable to uneven fissionable material distribution within the targets. This was initially observed in the aqueous targets, particularly in the higher mass targets, where expected signals measured significantly lower than anticipated, based on previous measurements and calculations, and varied under repeated measurements. The issue was identified as incomplete dissolution of the fissionable material within the target, likely due to settling or salting when the target sat or remained unused for long periods of times. Simply agitating the targets to ensure dissolution before the experimental collections resolved the issue and variance between repeated target runs, even with months between experimental campaigns, became minute. A single exception was the with the aqueous target labeled Th-2, which eventually failed and began to leak (thorium 'salt' was discovered on the exterior of the container in storage), forcing target removal.

Further inspection of the container revealed what appeared to have been a minor manufacturing defect (likely a pinhole or perhaps a thin spot), which then led to the container failure. It is likely that the solution chemistry which allowed the thorium to begin to salt out and would have been acidic, attacked this defect and degraded the surface. All other containers were inspected, but no other issues were noted; no further container degradation has since been observed in the series. In addition to the noted issues with fissionable material dispersion within the aqueous targets, some issues were observed with the oxide series as well. Due to the nature of the oxides, there was concern about obtaining even distributions of the fissionable material within the sand matrix, especially given that the particle sizes were different. Early experimental work looked for indications of issues (utilizing signal yield, yield will be discussed in the following results chapters); some distribution issues were noted. Namely, in some of the early results, the observed target yield was noted to vary with target placement; the simple rotation of a target could alter the yield by significant amounts (10's of percents). The variance was quickly attributed to settling of the fissionable oxide, allowing the material to collect against a single wall or the bottom of the target can; rotating the target adjusted the overall target fission rate and the detected signature as the amount of fissionable material directly in the beam was varied. Awareness of the potential for uneven distribution largely solved the issue. By adequately mixing the target prior to use, the issue was largely resolved; however, some of the early results obtained did not account for this, and the overall target yields thus reflect this. In the later target studies, as for the aqueous targets, incorporating systematic target agitation before the interrogations seemed to alleviate any data inconsistencies attributable to uneven fissionable mass distributions within the targets.

3.4 Experimental Geometry II

The combined signatures' experimental campaigns utilized the same accelerator and similar beam parameters for interrogation as for Experimental Geometry I, but employed much longer separation or stand-off distances. The experimental setup

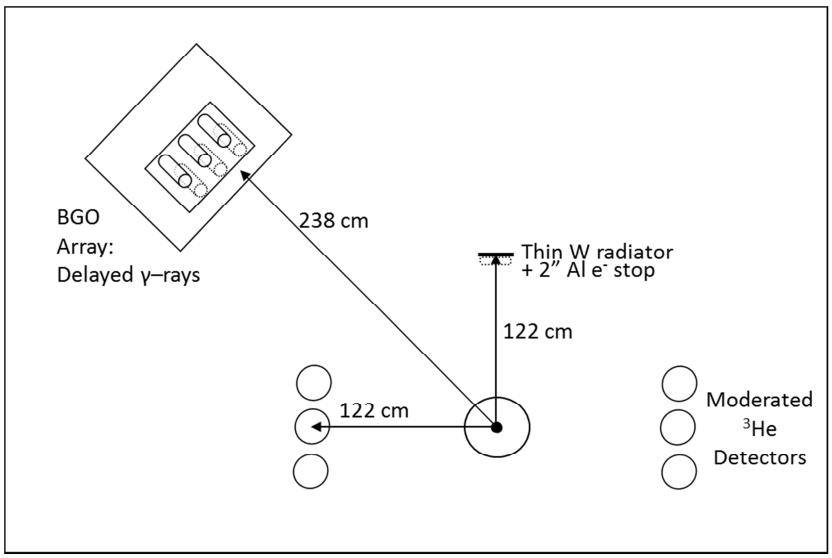

Figure 3.3: An overhead view of the experimental setup utilized for the combined signatures studies.

is summarized in the schematic shown in Figure 3.3. The neutron response was measured utilizing the series of six moderated ^{3}He neutron detectors (MHNDs), which were arrayed around the interrogation target, with three detectors placed to either side of the target at a distance of 122 cm from target center to detector center; the MHND specifics were discussed in Section 3.1.

A series of five bismuth germinate ($Bi_4Ge_3O_{12}$ or simply BGO) detectors were also deployed to detect γ-ray signatures of the targets. The BGO detector array was heavily shielded and placed at a back angle to the forward beam direction, as illustrated in Figure 3.3, an overhead schematic of the setup. The BGO detectors were housed in individual channels inside of a large borated polyethylene block which served primarily to provide shielding from the large active neutron background of the acquisitions. Each channel of the polyethylene was lined with 5.08 cm thick lead rings, and the BGO detectors were placed inside, with the face of the detectors in direct line of site to the target location. The lead rings served to provide shielding of the BGO detectors from photons arriving from directions other than the target location and thus to reduce the measured (non-target) γ-ray background rates attributable

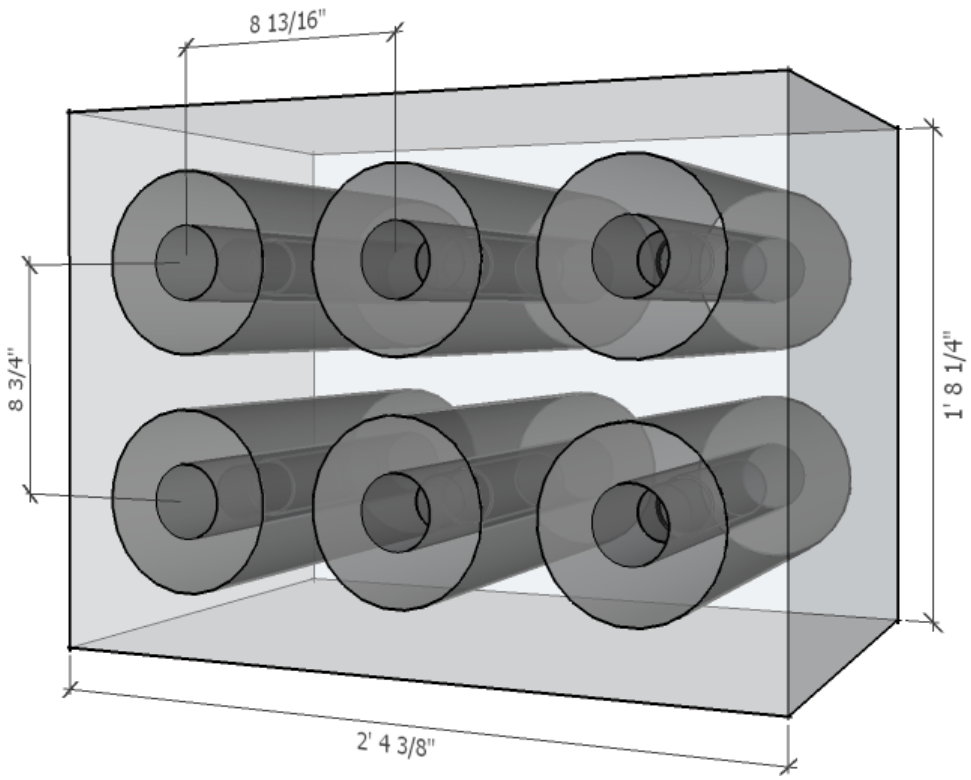

Figure 3.4: A representation of the shielding array utilized for the BGO γ-ray detectors in the combined signatures studies. The large rectangular borated polyethylene structure housed cylindrical slots for 2" thick lead rings into which individual BGO detectors are fitted.

to the environment; the BGO detectors were set back inside of the lead rings by 3" to provide collimation. This shielding array is illustrated in Figure 3.4. To further reduce the undesirable radiation effects on the detectors, the entire array was then wrapped in an additional 10.16 cm of lead on all sides except for that facing the targets (i.e. the side containing the detector faces), and an additional 10.16 cm of borated polyethylene blocks on all sides including the detector faces. Additional shielding walls (*not illustrated*) were constructed to further shield the γ-detector array from direct view of the end of the accelerator and the radiator, in order to shield the BGO array from view of the electrons impinging on the radiator; these shielding walls consisted of lead and concrete.

Neutron signals were recorded exactly as for the previous measurements, Experi-

mental Geometry I. Photon time and energy information was recorded for each of the BGO detectors using a multi-parameter data acquisition system. Each detector signal was processed through a spectroscopy amplifier (and corresponding pre-amplifier) and input to an ADC (analog-digital-converter) read out by the computer controlled data acquisition system. The ADCs (and thus the gamma detectors) were triggered by each accelerator gun pulse; data was collected in an event-by-event mode (list mode) which recorded the time stamp and energy information of each incident photon, allowing for significant post-processing options for analysis. The BGO detectors were uniformly gated off for a set time window of 6 msec in order to mitigate any data acquisition during the recovery period immediately following the large photon flash on the target, when the detectors might initially be saturated. Results were thus acquired between photon pulses and summed over many accelerator pulses. The majority of the experiments were conducted at an accelerator repetition rate of 7.5 Hz, resulting in a total time window of $\sim$133 msec between photon pulses. The timing structure is thus as was shown in Figure 3.2.

Table 3.1: Description of experimental ^{232}Th and ^{238}U aqueous targets.

Target	^{232}Th Mass (g)	^{238}U Mass (g)	Concentration	Relative ^{232}Th	Relative ^{238}U
^{232}Th-1	9.8	0.0	0.95%	100%	0%
^{232}Th-2	18.1	0.0	1.7%	100%	0%
^{232}Th-4	37.9	0.0	3.5%	100%	0%
^{232}Th-5	59.6	0.0	5.2%	100%	0%
^{232}Th-7	83.4	0.0	7.0%	100%	0%
^{232}Th-9	109.7	0.0	8.7%	100%	0%
^{238}U-1	0.0	10.0	0.98%	0%	100%
^{238}U-2	0.0	16.2	1.6%	0%	100%
^{238}U-3	0.0	33.6	3.1%	0%	100%
^{238}U-5	0.0	52.2	4.7%	0%	100%
^{238}U-6	0.0	72.3	6.3%	0%	100%
^{238}U-8	0.0	94.0	7.8%	0%	100%
Mixed-A	11.4	30.8	3.9%	27.0%	73.0%
Mixed-B	23.4	31.7	4.9%	42.5%	57.5%
Mixed-C	32.5	21.1	4.8%	60.6%	39.4%
Mixed-D	34.6	10.4	4.1%	76.9%	23.1%

Table 3.2: Description of experimental ^{232}Th and ^{238}U silicon oxide (sand) targets.

Target	^{232}Th Mass (g)	^{238}U Mass (g)	Concentration	Relative ^{232}Th	Relative ^{238}U
^{232}Th-0.5	8.25	0.0	0.5%	100%	0%
^{232}Th-1	16.59	0.0	1.0%	100%	0%
^{232}Th-2	33.56	0.0	2.0%	100%	0%
^{232}Th-4	68.73	0.0	4.0%	100%	0%
^{232}Th-6	105.61	0.0	6.0%	100%	0%
^{232}Th-8	144.34	0.0	8.0%	100%	0%
^{238}U-0.5	0.0	8.25	0.5%	0%	100%
^{238}U-1	0.0	17.21	1.0%	0%	100%
^{238}U-2	0.0	34.81	2.0%	0%	100%
^{238}U-4	0.0	71.35	4.0%	0%	100%
^{238}U-6	0.0	109.74	6.0%	0%	100%
^{238}U-8	0.0	150.14	8.0%	0%	100%
Mixed-A	21.17	84.66	6.0%	20.0%	80.0%
Mixed-B	42.31	63.47	6.0%	40.0%	60.0%
Mixed-C	63.43	42.29	6.0%	60.0%	40.0%
Mixed-D	84.54	21.14	6.0%	80.0%	20.0%

Table 3.3: Summary of experimental ^{239}Pu and ^{235}U targets in oxide (sand).

Target	Mass
^{239}Pu	2.0 g
^{235}U	2.73 mg

Chapter 4

Delayed Neutron Results: Detection and Identification

This chapter begins the review of the experimental results achieved. The results presented in this chapter will focus on the delayed neutron signature, investigated through the use of the series of low–mass aqueous and oxide targets summarized at the end of Chapter 3. These results were obtained primarily through compact detector configuration around the target, in order to maximize the signal to noise response. It is appropriate to begin first by analyzing how the delayed neutron signal is defined.

4.1 Delayed Neutron Time Response

As noted in Figure 3.2 from the preceding chapter, the accelerator gun pulse marks the $t = 0$ position in our experiment. Consider now the detector response as a function of time after the incident bremsstrahlung pulse, Figure 4.1, where the detector is the array of six MHNDs and results are summed over many accelerator pulses. The yield responses are shown for three targets, two targets containing fissionable material, ^{238}U or ^{232}Th, and a pure water target utilized for an active background measurement; responses for each target have been normalized by the time bin width and the total charge incident on the radiator, as a proxy for the bremsstrahlung intensity.

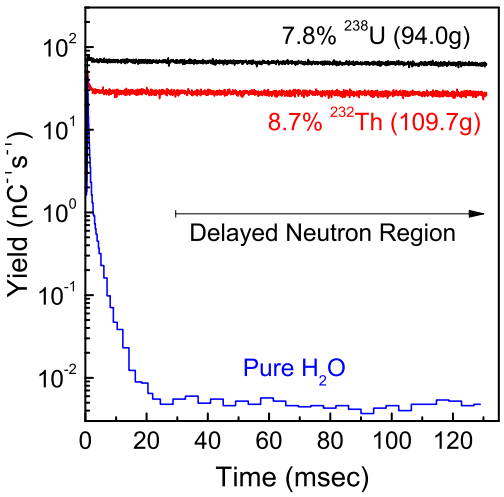

Figure 4.1: The detector response, indicating neutron yield, as a function of time after the incident bremsstrahlung pulse, $t = 0$. The data shown were recorded for ∼300 s per target with beam parameters of 16 MeV and 7.5 Hz, with the results summed over all accelerator pulses. Results for each target have been normalized by the time bin width and the total charge incident on the radiator as a proxy for the bremsstrahlung intensity.

Even when only relatively small amounts of fissionable material are present, the neutron response is elevated for long periods of time. The actinide targets shown in Figure 4.1 contain only ∼100 grams of material, and yet the responses remain elevated by at least three orders of magnitude above that of the pure water target throughout the entire time collection shown, extending to 133 ms or the end of the window defined by the accelerator pulse rate. In contrast, the yield falls rapidly for the non-fissionable water target, dropping several orders of magnitude within the first few tens of milliseconds; a factor of more than 4400 is observed between the water response at just 0.6 ms as compared to 30 ms. The early time neutrons may be attributed to fission as well as to additional reactions. The target and the surrounding environment produce neutrons which then scatter back to the detectors, either directly or through indirect processes such as scattered photons resulting in (γ,n) reactions in the case of a non-fissionable target; these effects clearly fall away as the time from the incident bremsstrahlung pulse increases. Note that the target containing only water is used

Table 4.1: Summary of the delayed neutron yield results shown in Figure 4.1.

Target	Fissionable Mass (g)	Yield (nC^{-1})	Comparison to Pure H_2O Target (factor)
1 L H_2O	–	$(4.851 \pm 4.222) \times 10^{-4}$	–
Th-5	109.7 g ^{232}Th	2.799 ± 0.127	5751
U-5	94.0 g ^{238}U	6.480 ± 0.194	13358

as an active background target for all of the aqueous solutions in these studies.

This distinct time–response of the neutrons may be exploited. By selecting an appropriate time window over which to sum the neutron counts, one may form a raw yield signature. In the case shown, selecting a delayed time region from 30 ms and beyond is appropriate, as the background signal indicated by the pure water target has subsided to near–passive rates; summing from 30 ms forward to just prior to the next accelerator pulse forms the raw delayed neutron yield. The yield values obtained for the targets shown in Figure 4.1 are summarized in Table 4.1. The delayed neutron yield constitutes the basis of this signature of fission, and is used as defined here throughout the remainder of this work.

This elevated raw yield may itself be used as a signature to detect the presence of fissionable materials. In the case of the targets shown in Figure 4.1, the fissionable yields are more than 5700 (^{232}Th) and 13300 (^{238}U) times the equivalent active background yield value obtained; more than three orders of magnitude greater. Although this result clearly represents detection of the presence of fissionable material in the system, more sophisticated methods may also be formed.

4.1.1 Repetition Rate

Section 2.3.4 showed the optimal delayed neutron window to be half of the total available acquisition time window determined by the accelerator repetition rate (Equation 2.41, page 33). This indicates that for the experimental campaigns a higher

repetition rate could be used – for the case of $t_{cut} = 30$ msec this would indicate a maximum repetition of ∼16 Hz, nearly doubling the tolerable accelerator pulses within a defined interrogation time window. A lower repetition rate was selected for several reasons. First and foremost were considerations of the length of the discard window (i.e. the prompt window); if higher bremsstrahlung energies or greater beam current was desired for later portions of the experimental campaign, then the width of the cut window might need to be increased accordingly. In that case, the remaining signal window and accompanying count statistics might then prove impractical for analysis. As the risk of this potential was unknown, it was much more prudent to err on the side of experimental caution and utilize a lower repetition rate, in order to incorporate tolerance; however, given typical environmental neutron behavior, it is unlikely that the discard window length would need to increase by more than an additional ∼10 ms – the undesirable effects have a limited lifetime. Even in environments with higher bremsstrahlung energy resulting in material activation with significant (γ,n) contributions, the greatest potential cause for extending the time cut, it is unlikely that these contributions would survive longer than several tens of milliseconds.

More significantly, a longer time window enables greater acquisition of the delayed signature at late times far from the fission event. This allows for better fitting of the delayed neutron time series, which will be discussed in later sections. As this fitting was of primary concern for isotopic identification, incorporating the late time data proved of great benefit. The utilization of a longer time window, extending the count region to >∼80 msec, enables more accurate inclusion of the long-lived Group 1 delayed neutron precursor contributions. It can be noted from Table 2.1 that the Group 1 α-values differ by nearly a factor of three for ^{232}Th (0.0496 ± 0.0007) as compared to ^{238}U (0.0170 ± 0.0004), as defined by Kinlaw's Ph.D. dissertation, [9]; this indicates significant variation in the contribution rates to the long-lived group for these materials of interest. Inclusion of all of the delayed neutron group information differences allows for greater certainty in the isotopic identification. A repetition rate of 7.5 Hz was therefore utilized for the experimental campaigns. This selection of repetition rate also allows for direct comparison of the data which resulted from the combined signatures campaign, the results of which are the subject of Chapter 5.

Further considerations for potential application of the signature may benefit from additional investigation of the improved signal strength likely obtainable with increased accelerator repetition rate; additional reading of relevant work which directly investigated signature effects due to repetition rate would be strongly suggested [9,93]. Certainly, applications which might utilize a high repetition rate and short interrogation time window for initial screening, followed by lengthier interrogation at a lower repetition rate for characterization of any targets of further interest could be imagined to be a foreseeable interrogation structure. However, for the research purposes of this work a single repetition rate was maintained for all results.

4.2 Mass-Yield Relation

A significant consideration when forming any signature of fissionable material is whether it is reliable to quantify the amount of material present upon detection. The potential for reabsorption of neutrons within the target itself exists and such effects could pose serious consequences for material quantification. To examine this, the series of varying mass targets were further investigated at two of the bremsstrahlung end–point energies, 11 MeV and 16 MeV. The results are presented in Figure 4.2 and Figure 4.3. All data was collected at a repetition rate of 7.5 Hz and results were recorded on each target for a period of $\sim$ 5 minutes; these parameters were selected to represent a reasonable inspection time, while providing sufficient time between accelerator pulses to collect an optimal signature. Delayed neutron time regions were selected to be 30 ms and beyond.

Figure 4.2 illustrates the results for the aqueous uranium and aqueous thorium target series at two inspection energies of 11 MeV and 16 MeV. All yields are formed by integrating the neutron rates, like those presented in Figure 4.1, for the delayed region of 30 ms and beyond, are normalized to the total acquisition accelerator charge, and are active background subtracted. In all cases, the yield responses shown as a function of the fissionable mass present in the target appears to be highly correlated to the mass. Least squares linear regressions were obtained for each target series at each energy, and the fits are indicated in the figures; the fits show very little

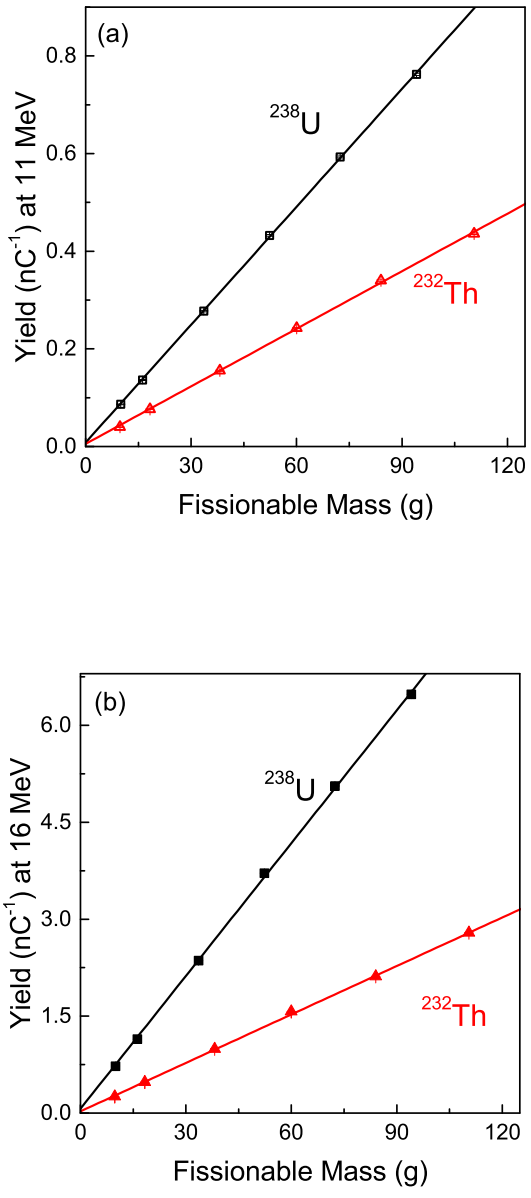

Figure 4.2: The delayed neutron yields shown as a function of fissionable target mass for two target materials, ^{238}U and ^{232}Th, in aqueous solution. The yields were investigated for the targets at (a) a bremsstrahlung beam end–point energy of 11 MeV and (b) a bremsstrahlung end–point energy of 16 MeV.

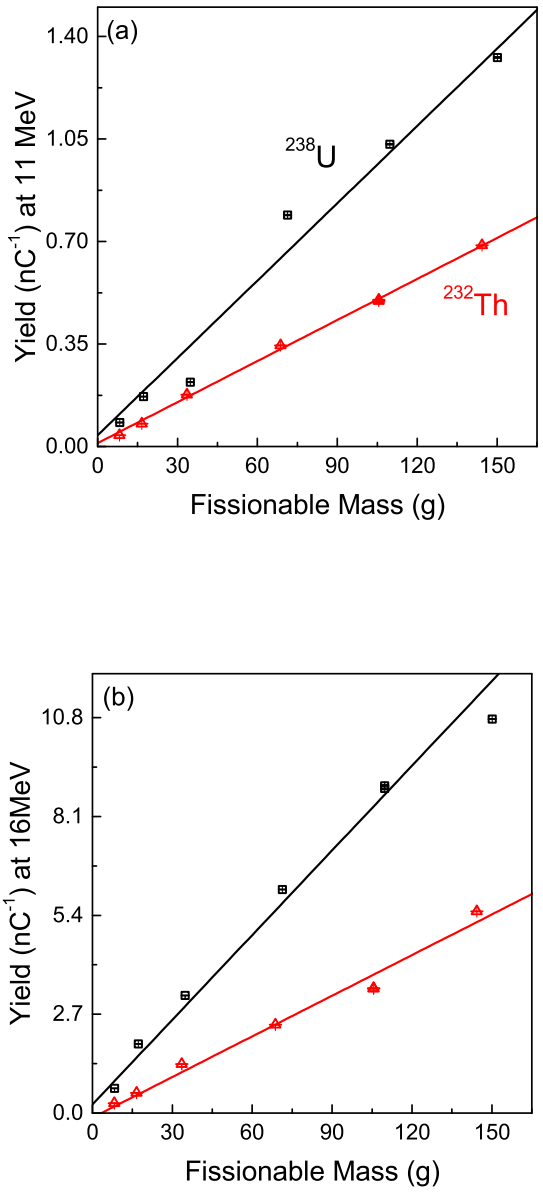

Figure 4.3: The delayed neutron yields shown as a function of fissionable target mass for the two given series of target material, uranium oxide and thorium oxide, in silicon oxide (sand) matrix. As for Figure 4.2, yields were investigated for the targets at (a) a bremsstrahlung beam end–point energy of 11 MeV and (b) a bremsstrahlung beam end–point energy of 16 MeV.

discrepancy. The linear regression values obtained are summarized in Table 4.2. Figure 4.3 illustrates the results for the second target matrix, silicon oxide, or sand. As for Figure 4.2, the responses are shown for two target mass series, uranium oxide and thorium oxide, at the two inspection energies, bremsstrahlung beam end–point energies of 11 MeV and 16 MeV. As compared to Figure 4.2, there is slightly more scatter observed in the individual mass yield points for the mass range, however there is still very high correlation observable between the measured yield responses and the target masses. Additionally, the oxide data indicated represents some of the earliest experimental silicon oxide results obtained; thus, awareness of the issues due to fissionable material distribution within the target was limited (discussed in Chapter 3). Much of the scatter observed in Figure 4.3 is likely attributable to an uneven distribution of fissionable material within the target. Least squares linear regressions were obtained for each of the target series at each energy, and the fits are also indicated in the figures. The R^2-values obtained again indicate very strong correlation between the fissionable oxide target masses and the yields obtained. The linear regression values obtained are again summarized in Table 4.2.

In this target mass region of interest, there is no appreciable self-attenuation of the neutron signature, and delayed neutron signals form a strong candidate for fissionable mass quantification. Note however that the linear response rate is dependent on both the probing beam energy and on the fissionable material of interest. The yield responses are stronger at the higher 16 MeV beam energy for both uranium and thorium independent of the target matrix, i.e. as compared to their respective 11 MeV responses; this is to be expected. As the photofission cross–section is greatly increased for both materials from 11 MeV to 16 MeV, it follows that the fission rate of the target material will be increased and thus that the delayed neutron production rate would also be greatly increased. The dependence of delayed neutron yield on the probing energy will be discussed further in the next subsection.

Also of note in Figures 4.2 and 4.3 are the relative differences in observed delayed neutron production rates between the uranium and thorium targets. The materials have distinguishable rate responses which are correlated to the specific isotopes, as indicated by Equation 2.33. This will be further investigated during the discussion

Table 4.2: Summary of the least squares linear fits shown in Figures 4.2–4.3.

Target	Intercept $nC^{-1} \cdot g^{-1}$	Slope $nC^{-1} \cdot g^{-1}$	Error $nC^{-1} \cdot g^{-1}$	R-value
11 MeV				
Th: H_2O Targets	$(5.37 \pm 3.45) \times 10^{-3}$	3.93×10^{-3}	5×10^{-5}	0.9993
U: H_2O Targets	$(8.07 \pm 2.90) \times 10^{-3}$	8.05×10^{-3}	5×10^{-5}	0.9998
16 MeV				
Th: H_2O Targets	$(2.61 \pm 1.51) \times 10^{-2}$	2.50×10^{-2}	2×10^{-4}	0.9997
U: H_2O Targets	$(6.75 \pm 4.19) \times 10^{-2}$	6.85×10^{-2}	7×10^{-4}	0.9996
11 MeV				
Th: Oxide Targets	$(1.16 \pm 0.79) \times 10^{-2}$	4.67×10^{-3}	8×10^{-5}	0.9982
U: Oxide Targets	$(3.83 \pm 7.70) \times 10^{-2}$	8.80×10^{-3}	8×10^{-5}	0.9649
16 MeV				
Th: Oxide Targets	$(-1.25 \pm 2.55) \times 10^{-1}$	3.70×10^{-1}	3×10^{-3}	0.9715
U: Oxide Targets	$(2.34 \pm 1.66) \times 10^{-1}$	7.71×10^{-1}	3×10^{-3}	0.9878

in later sections regarding the isotopic specificity of signatures.

4.3 Yield as a Function of End Point Energy

The response of the target series may next be considered as a function of changing bremsstrahlung end–point energies. The previous section illustrated the rate differences which result from the two different end–point energies of 11 MeV and 16 MeV. As the photofission cross section changes as a function of energy (i.e. Figure 2.2, page 13), investigating responses for many beam energies allows one to probe this dependency. However, the probing bremsstrahlung beam will have an associated distribution of photon energies; results will therefore be a convolution of the effects of the cross section energy dependence and the probing energy spectrum.

Figure 4.4 shows the recorded delayed neutron yields for a number of bremsstrahlung end–point energies from ∼6 MeV to 19 MeV, for two subsets of targets, in the aqueous and oxide matrix. For each of the aqueous and oxide target sets, a uranium and thorium target were selected along with the corresponding active background target for all measurements of interest. Each spectra was recorded for $\sim$ 5 minutes and the delayed neutron response results summed. An overall increase in yields is observed in the target responses with increasing probe energy. The fissionable target yields rise rapidly, increasing approximately two orders of magnitude per target response from 7 MeV to 15 Mev, until they begin to plateau. Again recalling the photofission cross section, this increasing fission response is an expected result; as the end–point energy continues to rise beyond the photofission cross section peak, an increased fraction of the resultant bremsstrahlung photons are able to induce fission, and the overall probability and therefore the rate of observed fission events increases. In contrast, the background target would be expected to remain fairly stable, perhaps rising slowly with energy given the increased probabilities of additional reactions such as photoneutron production or activation of materials in the surrounding environment, which may then interfere via artificial signals. However, the results clearly illustrate that the active background yield begins to rise above 16 MeV, the response increase dramatic. A secondary reaction which is specific to the background target(s)

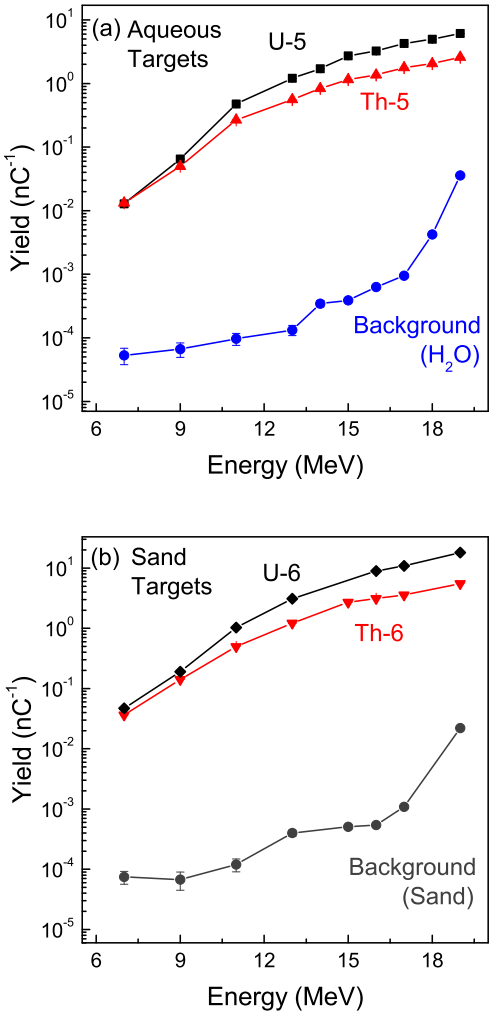

Figure 4.4: The delayed neutron yields as a function of the bremsstrahlung end–point energy, for (a) the aqueous targets and (b) the silicon oxide (sand) targets. The bremsstrahlung end–point energy was varied from ∼7 MeV to 19 MeV; data was recorded for each target for a 5 minute inspection at 7.5 Hz. A pure water target and a pure sand target were utilized as respective active background targets for all measurements of interest.

seems highly likely, contributing to the delayed neutron yield in the high-energy results; this is indeed the case.

4.3.1 Background Increase Due to Oxygen

The ^{17}N isotope is a delayed neutron precursor with a half-life of 4.17 seconds. This is produced by the $^{18}O(\gamma, p)^{17}N$ reaction, which has a threshold energy of 15.9 MeV; as the end point energy of the electron beam increases, more of the bremsstrahlung photons have enough energy to initiate this reaction and oxygen containing targets will begin to contribute increasing neutrons to the signal, which may interfere with the delayed neutron signature from fissionable isotopes. Oxygen contains only $\sim$0.2% ^{18}O, and a distribution of photon energies exists rather than a monoenergetic interrogation beam energy; the contributions will therefore begin to increase at beam energies above the threshold but may only become pronounced at higher interrogation energies. As the interrogation energy increases to the higher beam end point energies, a significant increase in the production of the ^{17}N delayed neutron precursor should be expected. This complicates the observed delayed neutron response due to fission isotopes. As the interrogation energy increases to the higher beam end point energies, a significant increase in the delayed neutron fission signature should also be expected, relative to the observed signal at lower energy.

Figure 4.5 illustrates the overlap of the photofission cross section for two fissionable isotopes, ^{232}Th and ^{238}U, with the simulated bremsstrahlung photon distribution shown for three relevant electron end point energies, 11, 16, and 19 MeV; the bremsstrahlung distributions were calculated with MCNP approximating the radiator setup. At 11 MeV the photofission cross sections are already reasonably large, and delayed neutrons can be utilized as a signature of fissionable materials within a target; however, the intersection of the bremsstrahlung photon distribution and the photofission cross section has not yet been maximized. The delayed neutron production will continue to rise as the electron beam energy is increased, due to the increasing photofission events. As the rise to higher beam energies continues, additional reaction paths will begin to turn on, competing with the desired photofission reactions or simply producing additional detectable reaction products; the distinct fission signature formed through delayed neutrons will become obscured and no longer be identifiable. The ^{17}N reaction is an example of such a case. The time–dependence

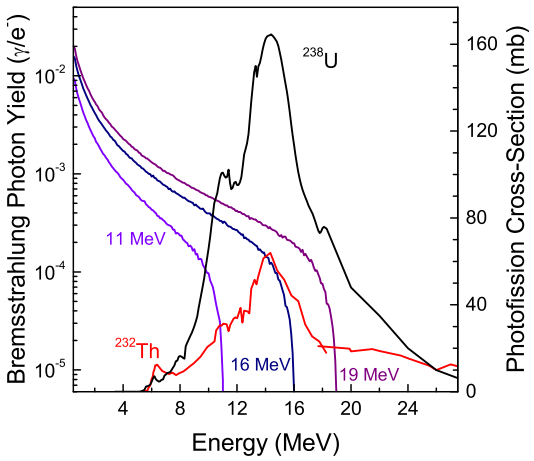

Figure 4.5: The ^{238}U and ^{232}Th photofission cross sections shown alongside the calculated bremsstrahlung photon spectra for three different beam end point energies, 11 MeV, 16 MeV and 19 MeV. The differences in overlap are reflected directly by differences in photofission rates, experimentally observed through differences in delayed neutron production rates in the targets of interest, as observed in Figure 4.4.

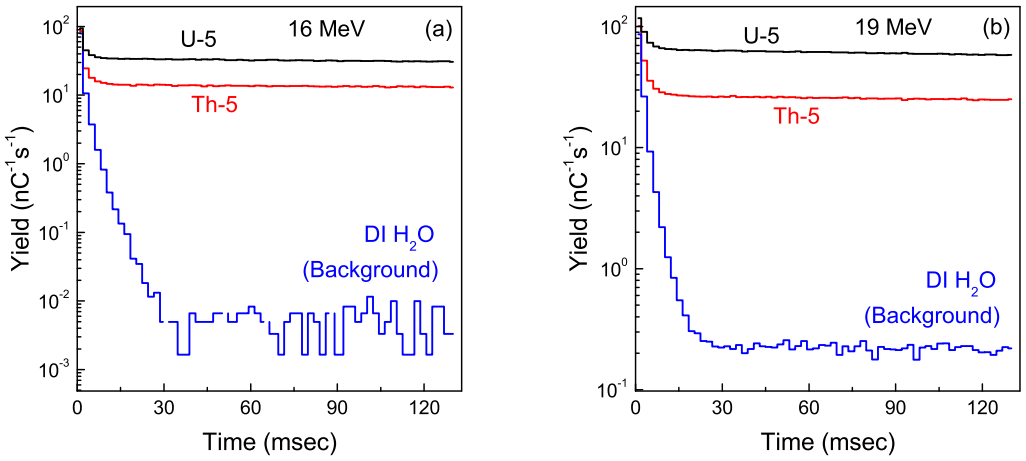

Figure 4.6: The measured delayed neutron rate responses shown for (a) 16 MeV and (b) 19 MeV for aqueous ^{238}U and ^{232}Th solutions and for a pure water target, utilized for active background. The values shown in Table 4.3 summarize the pertinent total delayed neutron yields obtained.

Table 4.3: Summary of the 16 MeV and 19 MeV delayed neutron yield results shown in Figure 4.6.

Target	Fissionable Mass (g)	Yield ($nC^{-1} \cdot sec^{-1}$)	Comparison to Pure H_2O Target (factor)
16 *MeV*			
1 L H_2O	–	$(4.852 \pm 0.406) \times 10^{-4}$	–
Th-5	59.6 g ^{232}Th	$1.364 \pm 3 \times 10^{-3}$	2811
U-5	52.2 g ^{238}U	$3.237 \pm 3 \times 10^{-3}$	6671
19 *MeV*			
1 L H_2O	–	$(2.242 \pm 0.025) \times 10^{-2}$	–
Th-5	59.6 g ^{232}Th	$2.586 \pm 3 \times 10^{-3}$	115
U-5	52.2 g ^{238}U	$6.134 \pm 4 \times 10^{-3}$	273

behavior observed in Figure 4.6(a) shows the response of several targets at 16 MeV. Contrasting this to the results of 19MeV, Figure 4.6(b), there is much less distinction between fissionable target yields and non-fissionable target yields at these higher energies; the delayed neutron yields shown are summarized Table 4.3, which makes the comparison clearer. Although the total yield has increased by moving to higher energy, the ability to draw conclusions about the target is reduced. For example, the total yield from the fissionable aqueous targets is increased by a factor of ∼2 between 16 MeV and 19 MeV, however, the background target yield has increased by a factor of nearly 50. Thus, at the lower 16 MeV probe energy, the delayed neutron yield due to the ^{238}U target was a factor of more than ∼6671 times the active background, but at the higher 19 MeV energy, the ^{238}U target yield is now only 273 times higher than the active background. This greatly increased background level jeopardizes the potential for the detection of small amounts of material. As the detection threshold is determined by the ability to separate elevated responses due to fissionable material from background levels, this reduced separation challenges that process. The higher

probe energies are thus not ideal for interrogation.

This is further illustrated in Figure 4.7, which shows the delayed neutron response as a function of energy for the two very low-mass fissile material targets, ^{239}Pu and ^{235}U in sand.

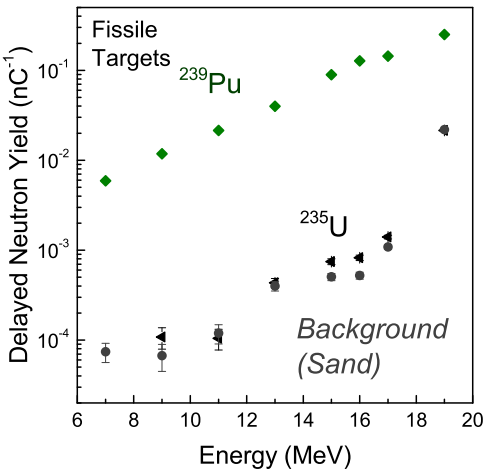

Figure 4.7: The delayed neutron response as a function of the bremsstrahlung end point energy for two very low-mass fissile targets, 2.0 g of ^{239}Pu in sand and 2.73 mg of ^{235}U in sand; the pure sand target utilized as an active background is also shown. The bremsstrahlung end point energy was varied from ∼7 MeV to 19 MeV; data was recorded for each target for a 5 minute inspection window at 7. Hz.

The plutonium target is clearly detectable, as the measured signal is nearly two orders of magnitude above the active background yields at all but the highest 19 MeV bremsstrahlung end point energy; as illustrated, even the 2 grams of material present is quite apparent. In contrast, the much smaller fissile mass ^{235}U target is clearly more difficult to detect; note that the target contains only 2.73 mg of ^{235}U. At low probe energies, there is not a distinguishable separation of the uranium target and the measured background rates; the targets are well within the measured errors of each other. At 15 MeV and 16 MeV, the measurements appear to become distinguishable from the active background target yield; the yield is a factor of just 1.199 or 3.478σ above active background at 15 MeV, and a factor of just 1.249 or 4.461σ

above active background at 16 MeV. These values are distinguishable from the active background sand target, but just barely, and might be likely to fall within systematic error tolerances. At the highest probe energies the separation between the targets is again reduced, due to the increasing background effects. Large masses of non fissionable material may result in an even higher background rate, further reducing the separation between a background signal and small fissionable masses of interest.

4.3.2 Conclusions Regarding End Point Energy

Consideration of the tradeoff between increased desired photofission signal and increased background signal is paramount, particularly if designing towards a detection system with the anticipated ability to induce a true or false conclusion regarding the presence of fissionable material in the target, i.e. real–world threat detection. Indeed, it is perfectly reasonable to infer that a large enough non fissionable target could have an equally observed signal to that of a small fissionable mass target; this would then result in a false positive detection by the system. Conversely, if a detection system threshold is set too high in attempting to avoid these issues, then false negative results may be unintentionally allowed. A discussion of detection threshold related aspects of a system will be presented in the following Minimal Detectable Mass subsection.

Given the initial end dependence results, it is worthwhile to highlight several regarding key inspection parameters. First, with respect to timing, the representative five minute interrogation window and 7.5 Hz repetition rate utilized clearly can result in a suitable signal and reasonable statistics for the purposes of material detection. Having reviewed the results for several interrogation energies, it is apparent that if the beam energy is too low, then the differential fission signature rate will be insufficient to produce conclusive target evidence; although increasing the interrogation window could potentially overcome this, for this case it is instead optimal to utilize a higher beam energy. Given the results of the end point energy target studies, a lower threshold of 11 MeV may be defined as a suitable parameter for the given inspection constraints. Similarly, in order to avoid the complications introduced by the use of higher end point energies, a maximum recommend energy of 16 MeV may be defined

for the remaining work.

4.4 Minimal Detectable Mass: Results

The delayed neutron yield has been shown to be a signature capable of detecting gram–level amounts of material of interest, including uranium, thorium, and plutonium, as demonstrated by the preceding experimental results. Given the demonstrated detection capability of even the very low mass (2.73 mg) ^{235}U target, it is apparent that this delayed neutron signature might be utilized to detect very minute amounts of material of interest. The minimal detectable mass results from Chapter 2 may be utilized to consider the detection limits of the system.

The detection limit discussion of Chapter 2 concluded with a relation of a measured signal response to mass and a result which was normalized to account for the active inspection response of the signature of interest, Equation 2.54. It was noted that for photofission, this normalization factor would be equivalent to the bremsstrahlung flux, as that has direct affect on the fission rate and thus on delayed neutron signal production. Further, the delayed neutron yield response has been demonstrated to be linearly proportional to target fission mass in the mass region of interest. In these experimental campaigns, the averaged accelerator charge on the radiator is utilized as a proxy for the bremsstrahlung flux. Thus for experimental parameters which result in an average charge $\mathbb{Q}$, the minimal detectable mass may be defined as,

$$\begin{aligned} m_{min} &= \left(\frac{dY}{dm}\right)^{-1} [L_D] \\ &= \left(\frac{dY}{dm}\right)^{-1} \left[\frac{k^2}{\mathbb{Q}} + 2\sqrt{2}k\frac{\sigma_B}{\mathbb{Q}}\right] \ . \end{aligned} \tag{4.1}$$

It is important to again highlight that the minimal detectable mass depends only upon the fluctuations in the background. In the case of delayed neutrons, it can be easily understood that a well-characterized interrogation construct which allows for paired measurements with limited background interferences would lend much stronger detection capabilities than a poorly studied system for which the potential background contributions and fluctuations were not well understood. A very well-known system

with low background and minimal deviations in the background signatures would be expected to have a much lower minimal detectable mass than a system with very high background levels and much higher deviations; the background within a system environment directly affects the capability of the system to detect extremely small masses of interest.

The minimal detectable mass can be calculated using Equation 4.1 and the measured yield response values of any known mass target. For the minimal detectable mass calculations and results presented here, operational parameters of $\sim$ 100 nC of charge per pulse for a 300 s inspection time at 7.5 Hz were selected. The calculated MDMs for each target are shown as a function of inspection energy in Figure 4.8 for (a) aqueous targets (b) for silicon oxide (sand) targets containing either ^{238}U or ^{232}Th. The aqueous and silicon oxide targets are again treated as distinct sets in order to compare the fissionable detection capabilities.

A minimum in the detection limits is observed across all targets at the mid-range energy values. Increasing the inspection energy from 7 MeV to 16 MeV decreases the minimal detectable mass, or MDM, for all materials of interest. The aqueous uranium target for example decreases from 315.1 mg at 7 MeV to 3.70 mg at 16 MeV, a factor of more than 85. The aqueous MDM values decrease slightly more as the energy increases to 17 MeV (3.30 mg, $\sim$ 10%) before rising rapidly with increasing energy. This upturn in values, as for all of the target MDMs, is due to the increasing background effects, the ^{18}O(γ,p)^{17}N reaction previously discussed. In contrast, the silicon oxide uranium target has a minimal detectable mass minimum at 16 MeV of 2.87 mg, versus 155.5 mg at 7 MeV, a decrease by a factor of only 17.5.

For the subset of targets of interest here, the thorium targets have a greater MDM value than the companion uranium targets, and the oxide MDMs are smaller than the corresponding aqueous targets. The variations in the MDM values is a direct result of the differing yield to mass responses of the target sets. The uranium targets have a stronger yield to mass response, that is, the increase in the yield due to increasing target mass is greater for uranium targets than for thorium targets, as observed in Figures 4.2 and 4.3. This results in slightly improved sensitivity of uranium targets as compared to thorium targets. Similarly, the silicon oxide target response are

Table 4.4: Summary of the calculated minimal detectable masses obtained, shown in Figure 4.8.

Target	Inspection Energy (MeV)	Minimal Detectable Mass (mg)
^{232}Th (H_2O)	7 MeV	348.8 mg
	11 MeV	35.23 mg
	16 MeV	9.969 mg
	17 MeV	9.040 mg
	19 MeV	34.42 mg
^{238}U (H_2O)	7 MeV	315.1 mg
	11 MeV	17.29 mg
	16 MeV	3.679 mg
	17 MeV	3.298 mg
	19 MeV	12.65 mg
^{232}Th (sand)	7 MeV	192.2 mg
	11 MeV	25.35 mg
	16 MeV	7.97 mg
	19 MeV	28.13 mg
^{238}U (sand)	7 MeV	155.5 mg
	11 MeV	12.69 mg
	16 MeV	2.870 mg
	19 MeV	8.884 mg

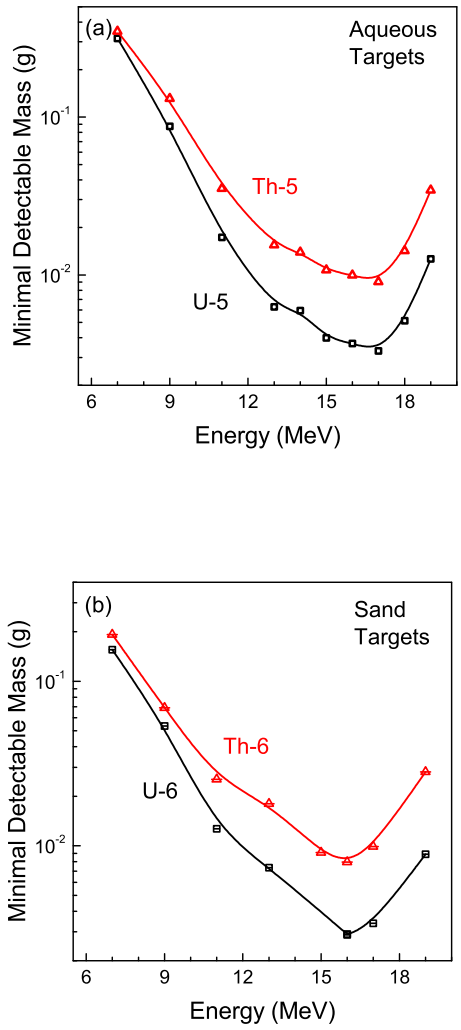

Figure 4.8: The calculated minimal detectable masses are shown as a function of the interrogation energy for (a) the aqueous targets and (b) the silicon oxide (sand) targets. Table 4.4 summarizes the minimal detectable mass values obtained. The calculations assumed experimental parameters of 7.5 Hz repetition rate with $\sim$ 100 nC charge per pulse for a 5 min inspection. The notable upturn at high energies is due to a competing background reaction and is discussed in detail in the text. The optimal operating energy was chosen to be 16 MeV where the detection thresholds are 9.970 mg for aqueous ^{232}Th, 3.679 mg for aqueous ^{238}U, 7.970 mg for oxide ^{232}Th, and 2.870 mg for oxide ^{238}U.

improved as compared to the aqueous responses, directly comparable using the least squares fit data summarized in Table 4.2. The stronger moderation of the neutrons within a water target results in decreased detection efficiency and thus decreased measured yield as compared to a silicon oxide target, and the MDM value is inversely proportional to dY/dm. The stronger yield response to target mass therefore results in decreased detection limits, and thus a lower minimal detectable mass is observed in the oxide targets as compared to the aqueous targets.

The optimal operating energy was chosen to be 16 MeV where the detection thresholds are 9.97 mg for aqueous ^{232}Th, 3.70 mg for aqueous ^{238}U, 7.97 mg for oxide ^{232}Th, and 2.87 mg for oxide ^{238}U. To clarify, these values conclude that the system and configuration utilized has a 95% probability of detecting a mass at this limit. In the case of the aqueous targets, this represents detection limits of 768 ppb ^{232}Th and 278 ppb ^{238}U. Although these values are incredibly low, it is reasonable to expect very sensitive detection capabilities for this system, given the very close experimental setup; the geometry utilized for these experiments is in large part responsible for the incredible sensitivity, and care must be taken that false conclusions regarding detection capabilities are not universally extrapolated. It is important to remember that these results are specific to the background measurements obtained and thus to the environment and experimental geometry of the measurements. The second experimental results chapter will focus on signature capabilities at greater stand off distances which more closely resemble real-world constraints for applications such as cargo inspection.

These detection limits clearly indicate the potential for successful application to the detection of materials. However, for many potential applications, material origin or attribution is desirable. This requires material identification; the previous approaches have not shown isotopic preference. Having identified a detection approach and quantified the potential limits to the detection capability, the experimental focus may now shift to the identification of the the materials detected, or of means of isotopic specificity of the target.

4.5 Isotope Specificity

The ability to detect nuclear materials is of principle concern, but beyond detection lies a principle desire to identify the material. Determining the isotopic specificity of an interdicted material has implications for origination determination or for informed decisions regarding the potential use intent of materials. Alternate potential scenarios such as material control or accountability may require explicit material composition information in addition to detection. Additionally, many post–detonation nuclear forensics capabilities rely first and foremost on isotopic content identification. The ability to improve rapid isotopic content identification capabilities, even in determining coarse content estimates for principle sample isotopics, is therefore of keen interest. Thus, beyond the established use of delayed neutron signatures to detect fissionable material, the application of delayed neutrons to the identification of nuclear materials is of significant interest; specifically, reference to identification for the remainder of this work will refer to the ability to identify isotopic content information about a target.

It is clear that the fission fragment distributions are unique to the fissioning systems or isotopes from which they originate, and thus the differences in the delayed neutron precursor distributions will be as well. Indeed, if the distribution differences are observable, then it should be expected that distinct temporal behaviors, distinguishable for isotopics, may be utilized to form a robust signature. Reexamining the time–response behavior as for the first results from the start of this Chapter, Figure 4.1, the detector responses to different fission isotopes, highlights additional information which may be utilized to form a more sophisticated signature.

4.5.1 Linearized Yield

Figure 4.9 illustrates the time response for two fissionable isotope targets, with behavior as for that shown in Figure 4.1, but utilizing smaller target masses, $\sim$50 g. Each measured response has been normalized by the initial rate response at $t = 0$, resulting in a common y-intercept of 1; the early time responses have been removed,

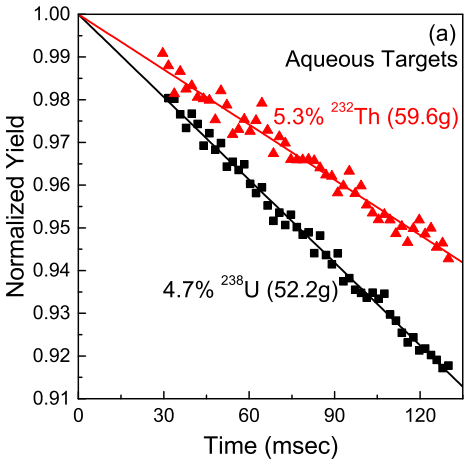

Figure 4.9: The time–responses for two aqueous targets containing fissionable isotopes, 59.6 g of ^{232}Th and 52.2 g of ^{238}U. E from Figure 4.1 shown normalized to the total signal yields. Each measured response is normalized by the total signal yield resulting in a common y-intercept of 1; the early time responses have been removed and the remaining results have been rebinned by a factor of 32 to improve the fitting and visual acuity. Data was recorded for a minimum of 1800 sec at 7.5 Hz.

and the remaining results have been rebinned by a factor of 32 in order to improve the fitting and visual acuity. The data clearly indicate linear rates of change in the yield on the measurement time scale; simple linear regression fits have been performed for each of the fissionable targets shown. The results of the regression fits obtained are summarized in Table 4.5. The fissionable targets exhibit distinct linear rates, even if it was not readily apparent in the initial time response view, Figure 4.1. As shown, the uranium target has a faster decay than the thorium target. Again, although this distinct isotopic time–response behavior is not surprising, the differences in the measured rates is clearly illustrated; the linearized decay rates are separated by more than $12.7\bar{\sigma}$. The fissioning isotopes result in unique fission product distributions, including the delayed neutron precursors, and thus in distinct delayed neutron emission rates, characterized by the distinct decay rates observable. These linearized decay rate values are incredibly strong indicators of the fissioning isotope(s) present in the system. Examining the sand targets provides an independent data set which can be

used to validate the results.

Table 4.5: Summary of the experimental ^{232}Th and ^{238}U linearized decay rate information obtained for aqueous targets shown in Figure 4.9.

Target	Decay Slope s^{-1}	Error s^{-1}	% Error
^{232}Th	0.4252	$\pm\ 1.23 \times 10^{-2}$	2.90%
^{238}U	0.6456	$\pm\ 8.1 \times 10^{-3}$	1.26%

4.5.2 Comparison to Calculated Decay Rates from Group Parameters

The expected decay rate values may be calculated for any isotope from delayed neutron group parameters by considering the response behavior of the delayed neutron emissions utilizing group parameter representation, Equation 2.33, within the acquisition time window. Delayed neutron group parameter values from a number of literature sources were cited in Chapter 2, Table 2.1. The results for the calculated decay rates utilizing group parameters from these sources are compared to the measured experimental values in Figure 4.10, treating the aqueous and sand targets as independent sets.

The measured experimental results indicate correlation to previously reported group parameter values. The indicated results show strong correlation between the measured linearized decay rate and the group parameters from photofission efforts, the results of Kull et al. and the results of Kinlaw. This is very logical, as the compound nucleus states and resultant fission fragment distributions are likely to be much nearer to these experimental studies than those of alternative neutron fission studies; the measured delayed neutron parameters under photofission conditions are the strongest against which to gauge the experimental linearized decay results. Although the results of Brady and England [5, 6] appear to differ from the experimental results obtained, error for the reference decay group group parameters are not reported; establishing

the true separation between these responses is not possible. Also detrimental, the Brady and England results are from emissions following neutron induced fission and not photofission production.

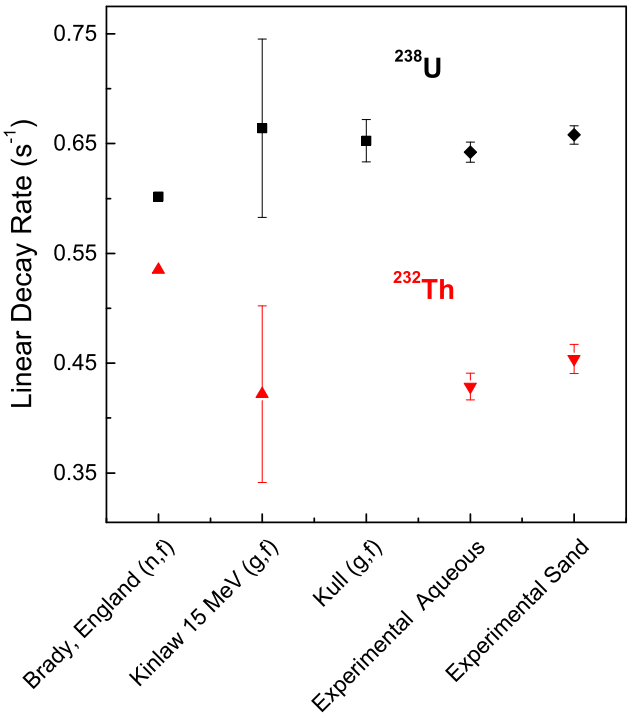

Figure 4.10: The calculated delayed neutron linear decay rates expected for a number of group parameter representations, Table 2.1, for the two isotopes of interest, ^{232}Th and ^{238}U. The measured experimental results for are shown for the aqueous targets and the silicon targets, in close agreement. The experimental data was collected at 16 MeV at a repetition rate of 7.5 Hz for ∼75 minutes for each target; the results are as for the linear decay rates in Figure 4.9 where least squares linear fits were performed to determine the linear decay rates of the targets.

4.5.3 Further Linearized Decay Rate Results

Using the optimally selected interrogation energy of 16 MeV as defined in previous results, further study was made on a subset of targets. Of interest are of course the series of pure component and mixed or bi–component targets identified at the end of

Table 4.6: Summary of the linear decay rate information obtained by least squares linear regression for each of the aqueous mixed component targets and the single component the 4.7% mass ^{238}U and 5.2% mass ^{232}Th targets. Data and the corresponding regression fits are shown for the ^{238}U, ^{232}Th, Mixed B, and Mixed D targets in Figure 4.11. Negative signs have been suppressed as the results are understood to be decays and thus decreasing yield responses as a function of time.

Target	^{238}U content	Linear Decay Rate	Error	R^2-Value
	%	λ : s^{-1}	s^{-1}	–
$U-5$	100	0.6423	9.2×10^{-3}	0.9908
Mixed A	73.0	0.6309	1.25×10^{-2}	0.9826
Mixed B	57.5	0.6070	9.43×10^{-3}	0.9893
Mixed C	39.4	0.5870	9.95×10^{-3}	0.9872
Mixed D	23.1	0.5496	1.55×10^{-2}	0.9656
$Th-5$	0	0.4287	1.23×10^{-2}	0.9645

Chapter 3. However, in order to be able to achieve good regression fits, long data acquisition times are needed, typically on the order of 30 minutes or more. Although much longer than is preferable for the detection of material presence, these acquisition times are more tolerable for obtaining isotopic information of targets known to contain fissionable material.

Figure 4.11 shows the results for the aqueous ^{238}U and ^{232}Th targets with two of the bi-component targets, again normalized to a common y-intercept of 1. Results were obtained for the full set of four mixed component aqueous targets, however, results for two of the targets are withheld from the figure to ease visual identification of the materials in the plot. Least squares fits were performed to determine the linear decay rate of each targets. The accompanying Table 4.6 summarizes the linear regression fit results for the mixed component aqueous targets.

As for the previous results, it is apparent that the uranium target has a faster decay rate than the thorium target. For the mixed component targets, this effect dominates as the content of uranium is increased; the decay rates accordingly increase for the mixed targets with increasing uranium mass. Consideration of how the decay rates

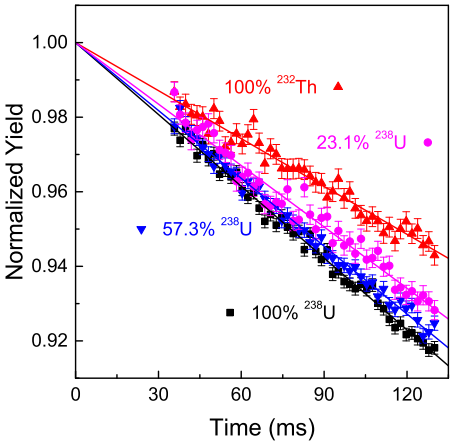

Figure 4.11: The normalized linearized delayed neutron responses shown for four aqueous targets of interest, the 4.7% mass ^{238}U target and the 5.2% mass ^{232}Th target, and two of the mixed targets containing differing combinations of ^{238}U and ^{232}Th, identified as Mixed B and Mixed D. Data was collected at 16 MeV at a repetition rate of 7.5 Hz for ∼75 minutes; data has been rebinned by a factor of 32 to reduce statistical spread of the responses and improve the fitting. Results were obtained for the full set of four mixed component aqueous targets, however, results for two of the targets are withheld to ease visual identification of the materials in the plot. Least squares linear fits were performed to determine the linear decay rates of the targets; results are summarized in Table 4.6.

change as a function of the uranium content of the targets results in Figure 4.12.

The normalized rates of the single component aqueous targets may be utilized to predict the expected decay rate for a given bi–component solution. The fit shown is a function of the fraction f of one of the components, chosen in this case to be the fraction of the uranium content. The function would be given explicitly by the results of Equation 2.34, where the calibration factors are derived from the dY/dm values, which relate the delayed neutron yield to the fission mass of each isotope; the experimental dY/dm values for the aqueous targets are summarized in Table 4.2. Denoting the terms by the isotopic A as subscripts, this result would be given by,

$$\lambda_{mix}(f) = \frac{f\frac{dY}{dm_{238}}\lambda_{238}^2 + (1-f)\frac{dY}{dm_{232}}\lambda_{232}^2}{f\frac{dY}{dm_{238}}\lambda_{238} + (1-f)\frac{dY}{dm_{232}}\lambda_{232}} \ , \tag{4.2}$$

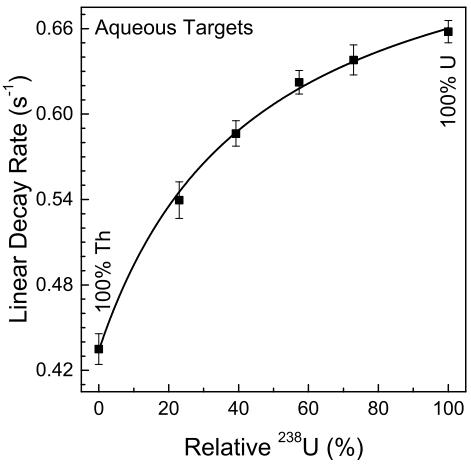

Figure 4.12: The normalized linear decay rates shown as a function of the fraction f of the ^{238}U component for the four aqueous mixed component targets and the single component ^{238}U (U-5) and ^{232}Th (Th-5) targets. The function shown is the predicted linear decay rate for a bi–component solution using the single component decay rate values obtained experimentally; the function form is given by Equation 4.2. Data was collected at 16 MeV at a repetition rate of 7.5 Hz for ∼75 minutes. Least squares linear fits were performed to determine the linear decay rates of the targets; results are summarized in Table 4.6. Error bars indicate 1σ for each target.

where f is again the fraction of the uranium content in the mixed isotopes target. Note that either isotope could be used for reference; for consistency, the ^{238}U isotope is maintained as the principle indicator throughout the remainder of the discussion.

In the case of the aqueous targets shown, there is strong separation between the composite targets, indicating isotopic identification capabilities. The single component targets have unique decay rates separated by more than 20σ. The mixed targets with the closest decay rate values are Mixed A and Mixed B, which are still separated by an average of 1.67σ from each other. For all of the bi-component targets, the decay rate may be predicted using the pure component rates; the curve shown is a fit of the date with functional as for Equation 4.2. The predicted decay rate may be utilized to estimate the minimal target separation which would be distinguishable. Utilizing the average experimental decay rate error for the results of Table 4.6, $\Delta\lambda = (9.86 \pm 1.89) \times 10^{-3}$ s^{-1}, the 1σ minimal separation be-

tween for example the thorium target and a low-mass uranium target would be $f_{U238} = (1.33 \pm 6.03) \times 10^{-2}$ or 1.33±6.03%. The statistical deviation in the decay rates obtained by regression clearly dominate the target separation capabilities, even at the long measurement times utilized for these results. A limitation ∼7.5% for isotopic concentration separability may well be acceptable in some scenarios. The implementation of a system for which very accurate isotopic content information is required should anticipate lengthy target measurement times.

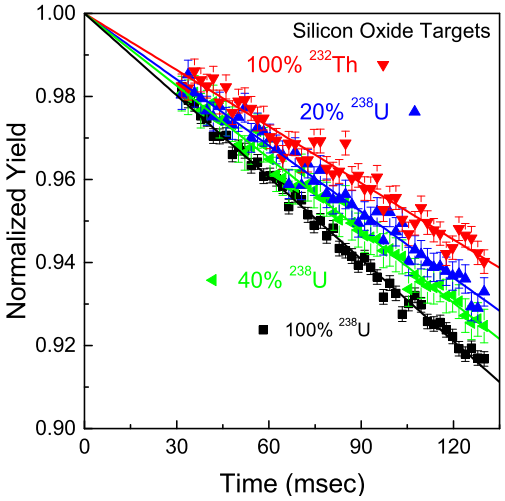

Figure 4.13: The normalized linear delayed neutron responses shown for four oxide matrix targets of interest, the *U*-6 ^{238}U target, the *Th*-6 ^{232}Th target, and two of the mixed targets, identified as *Mixed C* and *Mixed D*. Data was collected at 16 MeV at a repetition rate of 7.5 Hz for ∼75 minutes and has been rebinned by a factor of 32. Results were obtained for the full set of four mixed component oxide targets, however, results for two of the targets are withheld to ease visualization. Least squares linear fits were performed to determine the linear decay rates of the targets; results are summarized in Table 4.7. Error bars indicate 1σ for each target.

Similar linear decay rate analysis may be performed on the series of oxide targets. Figure 4.13 shows the results for the oxide 6.0% fissionable mass ^{238}U and ^{232}Th targets along with two of the bi-component oxide targets, again normalized to a common y-intercept of 1. Results were obtained for the full set of four mixed component oxide targets, but results are again suppressed for two of the targets to ease the visual identification of the materials in the plot. Least squares linear fits were performed to

Table 4.7: Summary of the oxide target linear decay rate information obtained; a subset of the targets indicated were shown in Figure 4.13. Negative signs have been suppressed as the results are understood to be decays, and thus decreasing yield responses as a function of time.

Target	^{238}U content	Linear Decay Rate	Error	R^2-Value
	%	λ : s^{-1}	s^{-1}	–
U-5	100%	0.6579	8.3×10^{-3}	0.9924
Mixed A	80.0	0.6539	1.02×10^{-2}	0.9884
Mixed B	60.0	0.6236	9.8×10^{-3}	0.9882
Mixed C	40.0	0.5810	9.1×10^{-3}	0.9883
Mixed D	20.0	0.5307	1.21×10^{-2}	0.9755
Th-5	0	0.4539	1.33×10^{-2}	0.9603

determine the linear decay rate of each targets. The accompanying Table 4.7 summarizes the linear regression fit results for the mixed component oxide targets. As for the aqueous targets previously, Figure 4.14 illustrates the oxide linear decay rates as a function of the relative uranium content in the targets, where a fit of the data is performed.

Comparison of the two sets of results indicates good agreement, well within error bars of each other, for the mixed component target series, as shown in Figure 4.15. The responses indicate that there is strong isotopic content identification. The decay rate is strongly correlated to the relative uranium content, and appears to be independent of the form of fissionable material or of the matrix material of the fissionable mass.

The linear decay rate results present an incredibly promising capability to identify isotopic information of fissionable material targets. However, the required acquisition times necessary to achieve discrepancy in the decay rates may prove too constraining for some applications. Thus, a more rapid analysis method for isotopic content is highly desirable. An alternative approach may be developed through the use of comparator yields.

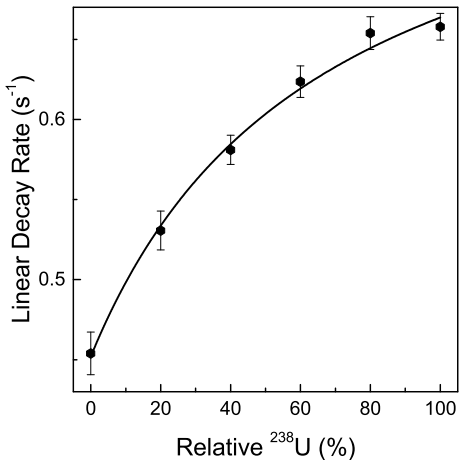

Figure 4.14: The normalized linear decay rates shown as a function of the fraction f of the ^{238}U component for the four oxide mixed component targets and the single component U-6 ^{238}U and Th-6 ^{232}Th targets. The function shown is a fit of the linear decay rate for a bi–component solution using the single component decay rate values obtained experimentally; the function form is given by Equation 4.2. Data was collected at 16 MeV at a repetition rate of 7.5 Hz for ∼75 minutes. Least squares linear fits were performed to determine the linear decay rates of the targets; results are summarized in Table 4.7. Error bars indicate 1σ for each target.

4.5.4 An Alternative Method to Specificity: Dual Energy Relative Yield (DERY)

Consideration of the delayed neutron response at distinct energies enables an analysis technique which takes advantage of the energy dependant photofission cross-section, observed in the Figure 4.4 experimental results. By comparing the yield at a selected inspection energy relative to a second fiducial energy, distinct isotope dependent behavior of the cross-section response may be highlighted and used to identify the material of interest.

In this case, a high end point inspection energy may be considered relative to a lower fiducial energy, and delayed neutron yield may be utilized for the signature. The Dual Energy Relative Yield, or *DERY* values, may then be considered. Since the yield response is linear to mass, at least for the target mass region of interest to

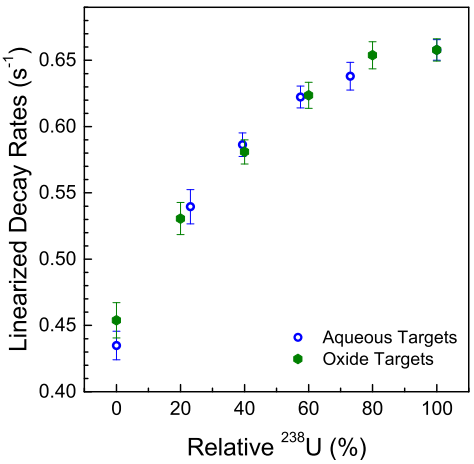

Figure 4.15: The normalized linear decay rates shown as a function of the fraction f of the ^{238}U component for the aqueous and oxide targets containing ^{238}U and $Th-6$, shown previously in Figures 4.11 and 4.13; regression values are summarized in Table 4.6 (aqueous targets) and Table 4.7 (oxide targets). The linear decay rates show close agreement for the responses for the two distinct matrix materials. This indicates strong isotopic identification capabilities, independent of the fissionable material form or of the matrix material. Error bars indicate 1σ for each target.

these results, the yield is a direct measurement of the target's fissionable mass. The fission response of a target is due essentially to the product of the fission mass and the photofission cross section; identical measurements of the fission response of a target at two distinct energies therefore assesses two unique photofission probabilities. The ratio of the yield at different energies thus directly extrapolates information about the ratio of the cross section at these energies.

The DERY responses for the mixed component target series were again investigated for both the aqueous and oxide target matrices. The DERY value may be calculated for any bi–component target utilizing the single component DERY values, as for the predicted linear decay rates previously. In the case of two pure fissioning isotope materials, where no background is present, the total yield would be given by the sum of the two isotopic yield contributions. The predicted DERY value for a target containing two materials, A and B, adopted from Equation 2.36, may be

defined as,

$$DERY = \frac{[Y_A + Y_B](E_{insp})}{[Y_A + Y_B](E_{fid})} \ , \tag{4.3}$$

where the subscripts indicate the material yield at either the inspection energy or the fiducial energy. The bicomponent solution fissionable masses may be defined by their isotopic contributions; the ^{238}U mass would be given by,

$$m_{238} = fM \ , \tag{4.4}$$

where M is the total fissionable mass of the target and f is again the fraction of the ^{238}U content of the target. The yield for a mixed component target at a given energy E is,

$$Y_{Total}(f) = fM\frac{dY}{dm_{238}} + (1-f)M\frac{dY}{dm_{232}} \ . \tag{4.5}$$

The DERY value then becomes a function the of the extracted mass-yield relations at two energies, and for mixed isotope solutions, a function of the fraction f of one of the components. With f as the fraction of the ^{238}U content, the mixed isotopic DERY value would be given as,

$$DERY(f) = \frac{[f\frac{dY}{dm_{238}} + (1-f)\frac{dY}{dm_{232}}](E_{ins})]}{[f\frac{dY}{dm_{238}} + (1-f)\frac{dY}{dm_{232}}](E_{fid})} \ . \tag{4.6}$$

A fiducial energy with near identical cross-section values for any material of interest would be ideal. For the relevant materials of these studies, ^{232}Th and ^{238}U, this would indicate a very low probe energy, as observed by the photofission cross-sections given in Figure 2.2. However, earlier studies of the measured delayed neutron response indicated the minimum recommended interrogation energy of 11 MeV. This value was therefore selected as the fiducial or reference energy in order to ensure sufficient statistics so as not to avoid systematic error. The higher inspection energy was selected to be 16 MeV, due again to the earlier results which suggest this as the maximum recommended inspection energy.

The yield responses for a 5-minute inspection window at each of the energies were utilized to analyze specificity by yield; thus a single target's identification constitutes a total of 10 minutes, much shorter than the required inspection times for specificity

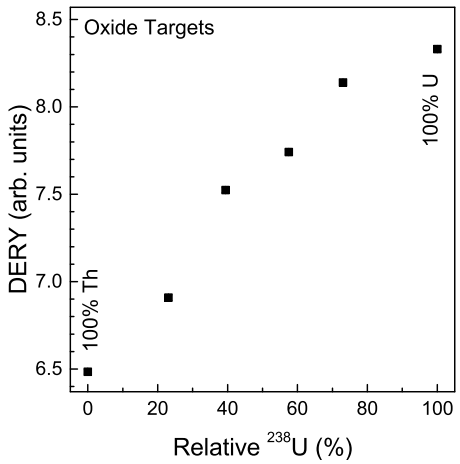

Figure 4.16: The predicted Dual Energy Relative Yield values for the aqueous target bi-component series, *U*-5 ^{238}U, *Th*-5 ^{232}Th, as a function of the relative ^{238}U content which they contain. DERY values are unitless and arbitrary. The data shown utilized a 5 min (7.5 Hz) inspection at each energy, 16 MeV and 11 MeV, for a total target inspection time of 10 minutes.

through linear decay rate values. Figure 4.16 shows the experimental DERY values obtained for the series of aqueous targets of interest as a function of the fraction f of ^{238}U content of the targets; the fit of the DERY values obtained is also indicated. It is clear from the results of Figure 4.16 that although there is more scatter between the relative uranium content and the experimental DERY values as compared to the linear decay rate results, there is still strong correlation and DERY still provides a strong means of isotopic identification despite the scatter in the observed results, with much shorter target inspection requirements. The DERY values for any bi-component compositions can be predicted utilizing the pure component DERY values; the fit obtained is indicated in the figure. The shape of the fit shows similar fit behaviour as observed for the linear decay rate responses, with a fairly rapid change in the predicted values with initial small relative contributions of uranium content, and decreasing impact to the predicted DERY value at high relative uranium contents.

Although the DERY approach represents a coarser means to isotopic content identification, it still presents a very rapid means for isotopic content estimate, and

may be employed in areas where significant deviations in relative concentration are of primary concern, or where rough isotopic composition can be utilized to determine further analysis steps.

4.5.5 Conclusions Regarding Specificity

Linear decay rates have been shown to be a strong approach to isotopic identification. Even dominated by fitting errors due to the limited experimental statistics observed, this approach still presents a capability for non-destructive isotopic content information to within $\pm\sim$7% of the relative content, for targets on the order of 10's of grams. The application of these techniques may be wide, especially for detection times on the order of 1.25 h needed to obtain the results shown here. For applications where shorter means to identification may be desirable, the alternative Dual Energy Relative Yield or DERY analysis method has been presented as a potential solution. This technique has also been shown to present a reasonable approach to isotopic identification, although there is more deviation from the predicted response. These observed scattering effects are likely due to experimental fluctuations not previously accounted for; fluctuations in the beam current during the data acquisition would for example have significant impact and may be neglected given the normalization parameters utilized. Further study would likely improve the predictability obtainable with this methodology.

Obtaining specificity for targets containing beyond two components may prove challenging. Although the linear decay rate and DERY approaches have been demonstrated as readily pertinent to two component targets, addition of a third component would increase the number of fitting parameters, potentially reducing confidence in results. However, it is possible that utilization of an additional inspection energy could overcome this challenge, taking advantage of different unique photofission cross-section responses, as demonstrated for the Dual Energy yield method. This would be particularly relevant for consideration of isotopics with vastly different cross-section responses at several energies. For example, in a three-component target, it may be possible to highlight one contributor at a probe energy where its cross-section

is reasonably substantial, but where the remaining two components have negligible photofission probability. Having obtained relative content information regarding one of the components, it becomes much easier then to potentially resolve the remaining two components. Alternately, distinct time regions of the delayed neutron response could be analyzed to provide further content information; this essentially attempts to directly capture delayed neutron Group information. However, this may prove challenging in a pulsed environment, especially when attempting to count between the photon flashes as for these studies, as this produces such a high environmental background, which may challenge the capabilities to distinguish unique time region responses. Leveraging time region effects would prove highly challenging utilizing the detector array as constructed for these studies, as neutron moderation effects distort the time responses of the dectectors, typically shifting μsec event time lengths to $m$sec; capturing subtle differences well enough to distinguish isotopic information is highly improbable for this detector array. Further study with faster detector response utilizing this approach would be necessary, but may prove capable of resolving time region effects, and thus of identifying distinct neutron Group information. Fitting across multiple Groups could again reduce the number of free fitting parameters required and thus prove able to resolve targets with greater numbers of components.

4.6 Summary

The unknown composition of any uranium-thorium target may now be extrapolated from measured delayed neutron results on any well-characterized system, using the above specificity approaches. Measurement of the linearized decay rate or of the DERY response would indicate composition information, i.e. the U-Th ratio. The overall target mass can then be extrapolated from the measured yield values using calibrated system mass-yield curves. Thus, these techniques now present a way to detect the presence of fissionable material within a system, and then to identify both the isotopic content and the mass of that material. The adaptation of these techniques to varied security applications is clearly pertinent. Although many potential use-scenarios are relevant, the remaining focus of this work will be limited to consid-

eration of cargo–screening–like applications. While previous works have undertaken full-scale implementation studies [19, 94], this work seeks rather to limit studies to a more generic implementation, and to assess the performance of the characteristic signature results in this potential application scenario. The remaining experimental results will therefore consider the measurement of delayed neutrons at greater standoff distances from targets of interest, the subject of Chapter 5.

Chapter 5

Shielded Target Investigations: Delayed Neutrons plus Delayed γ-Rays, Companion Signatures

The remainder of this work will focus on signatures in a larger detection geometry, and will also utilize delayed γ-ray signatures. The first step is to begin by defining the detection approach and signature characteristics for the γ-ray signal.

5.1 Detection of γ -Rays

An array of five bismuth germinate ($Bi_4Ge_3O_{12}$ or simply BGO) detectors was utilized for the detection of the γ-rays which forms a second signature of fission. Bismuth germinate is an activated inorganic scintillation material which emits light following interaction with ionizing radiation; light is then captured and amplified by a photomultiplier tube (PMT) coupled to the crystal, in order to result in a large detectable electronic signal, indicative of the incident radiation. There are a wide variety of scintillating materials, and the development, characterization, and optimization of scintillating detectors represents an enormous subset of detection science and industry, which is a well-defined field more than a century old [95]. A great deal of detectors are readily available commercially and are considered to be

standard for spectroscopy needs.

The selection of BGO detectors in this case was motivated by a number of decision factors, including but not limited to availability, cost, resolution needs, and rate capabilities. A principle concern of detector selection is the environment in which the signatures will be acquired. As even the large-scale geometry of these campaigns require tolerance of a high-rate and high-background environment, potential activation of the scintillation material was an early experimental design concern. Perhaps the mostly widely used scintillation material, sodium iodide with thallium iodide activator, or NaI(Tl), considered a standard within detection applications, was considered. It is not only readily available (and typically at relatively low-cost), but also has excellent light output (from Knoll's "Scintillation Detector Principles" overview, NaI(Tl) light output is given as 38k photons/MeV, [83]); the use of NaI(Tl) in this case however would be severely limited by the use environment constraints [96]. The crystal may become neutron activated, resulting in severe distortion of the spectral data; as the detectors would be deployed in an active neutron environment where even aggressive shielding designs could not ensure the elimination of activation, sodium iodide detectors were not a prime candidate. While BGO detectors have lower light yield, (again from Knoll's "Scintillation Detector Principles", BGO light output is given as 8200 photons/MeV, [83], a factor of 4 less than the reported NaI(Tl) light yield), in the case of a high–rate environment, this could potentially pose significant advantage over sodium iodide detectors. This comparatively low light yield value is driven primarily by the high refractive index of BGO as a scintillation material [83] which greatly restricts capacity for efficient light collection, but which makes BGO a desirable selection for the consideration of high count–rate needs, where saturation resulting in decreased detection performance is a significant potential concern. BGO energy resolution may not be optimal in the case of high–rate collections, but provided that discrete peak information is not required, the limitations of energy resolution are not a driving decision factor. Parallel studies have investigated the utilization of discrete γ-ray signatures for material identification, with results which have indicated an impressive resource for inspection object characterization [68]. A final aspect of BGO detectors which should be acknowledged as extremely advantageous for this ap-

plication is the overall stopping power of the material. In comparison to other widely available scintillation materials, BGO has a very large density (nearly twice that of sodium iodide), and provides much greater attenuation for γ-rays, thus greatly improving the odds of detecting the full energy of an incident high–energy γ-ray within a given crystal volume. All of these aspects combine to make BGO detectors a prime candidate for the given experimental constraints.

5.1.1 Review of Experimental Set Up

As noted in Chapter 3, these studies utilize much greater stand–off distances, for both the radiator-to-target distance and the target-to-detector distances, than for the previous delayed neutron campaigns. Please reference Figure 3.3 (page 48) if needed; the standoff separation between the target and the BGO array is 2.38 m while the standoff separation between the target and the MHND array is 1.22 m, where the MHND array was divided into two symmetric sections arrayed to either side of the target. Recall that the BGO array is heavily shielded, with the detectors housed inside of borated polyethylene and lead, as well as added shielding wall features, in order to mitigate the high-field accelerator hall environment.

Series of targets of interest were also discussed previously, and summarized in Tables 3.1 and 3.2. As these experimental campaigns focus on the potential application of signatures for detection scenarios such as cargo inspection, relevant vetting includes investigation of target shielding impacts on the signatures. Special efforts were made to investigate these effects. A selected subset of targets which were chosen to facilitate study of both low fission mass targets, on the order of grams, and higher fission mass targets, on the order of kilograms, while facilitating experimental time constraints, were investigated in a number of shielded target configurations. Two materials, borated polyethylene and lead, were used to shield the target, where each target was surrounded by the chosen material on all sides in successive thicknesses from 0 cm to up to 30.48 cm, in order to evaluate the shielding effects as a function of the increasing thickness of shielding materials. Further discussion regarding the shielding follows in subsequent sections.

5.2 A Delayed γ-Rays–Based Signature of Fission

Just as when constructing the delayed neutron signature of fission, consideration of the dynamic behavior of the γ-ray response is of principal interest. However, unlike the neutron response where only time information is acquired, the gamma signature is much more sophisticated: energy information is also acquired for each detection event. Recalling from the Experimental Overview description that all data is recorded in an event-by-event (list mode) approach, acquisition data analysis requirements are minimized, allowing for great flexibility in post-processing analysis of the results. This flexibility is primarily due to the desire to maximize the research analysis potentials; a deployed system would not be constrained to these same needs and could thus be operated with greatly decreased data handling requirements.

Figure 5.1 illustrates several introductory energy spectra, which compare the γ-ray response for the passive (background) nature of a target of interest and the response of the same target under active interrogation. The recorded responses are shown for the BGO detector array, normalized to the energy bin width and the detector array acquisition time as a function of the photon event energy. Spectral responses were recorded for a large metal fissionable material target, consisting of 2.6 kg of depleted uranium. The passive background measurement is shown in black (dashed line), for the spectra recorded in the experimental setup devoid of any photon beam for $\sim$60 minutes. An active measurement of $\sim$5 minutes on the depleted uranium target, with inspection beam parameters of 16 MeV and 7.5 Hz, is shown in red (solid line). As discussed in section 3.2, the acquisition system was triggered by the accelerator gun trigger and results are thus summed over many pulses; the BGO detector array was gated off for the immediate 6 ms following any gun pulse so as to prevent γ-ray acquisition during detector recovery from the large photon pulse in the experimental hall; the active spectra acquisition time is therefore calculated as the inspection time minus the total time for which the detector array was gated off.

A difference is clearly observed in the spectral response under active interrogation. The passive response essentially ends with a peak centered around 2.6 MeV, a background line which is the result of the isotope ^{208}Tl (2614.53 keV), found in the thorium

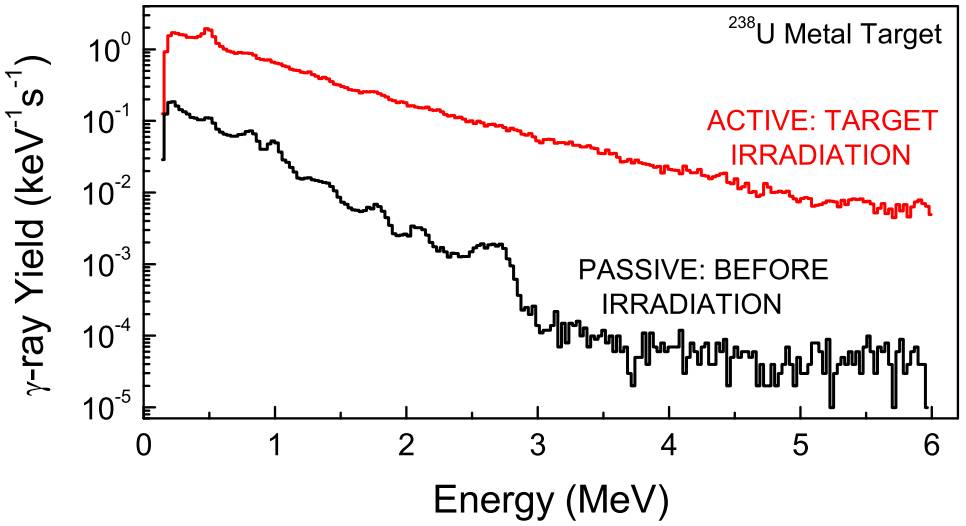

Figure 5.1: The recorded γ-ray spectra for a metal depleted uranium target (2.6 kg), shown for a passive measurement, target in situ but with no accelerator current, recorded for 60 minutes (black), and for an ∼5 min active inspection of the target, with beam parameters of 16 MeV and 7.5 Hz (red). The spectra have been rebinned for visual acuity and normalized by the energy bin width and the total detector array acquisition time.

decay series and very common in many environments as well as potential targets of interest. The active measurement however records a significant number of events well above this energy, the results of the decay of many short-lived fission products which are created in the target during the interrogation measurement. Although there is significant yield recorded for the passive measurement up to nearly 3 MeV, including characteristic peaks observed around 1 MeV, the yield is dramatically increased even for the much shorter active measurement. The difference in measurement times is a factor >10 for the passive measurement, although the spectra have been normalized so as to account for the acquisition times. The overall yield is significantly higher in the measured active spectra, a direct effect from the photon signature due to fission events induced in the target (^{238}U). Discrete peaks are more readily observed in the passive measurement, while the overall increased response of the active spectra makes distinct peaks difficult to observe, at least given this detector array's resolution. The

measured active inspection response is at least a factor $\gtrsim 10$ higher than the passive spectra shown in Figure 5.1, across all recorded energies. This response indicates that the readily induced photon response rate is much more significant in active interrogation as compared to passive measurement of the target of interest. Of particular significance is the response difference in γ-rays with energy greater than ~ 3 MeV; there are a considerable number of recorded high-energy events in the active measurement, a marked difference as compared to this region in the recorded passive spectra. Forming an overall yield by summing the total responses, the active spectra has a yield of 1.53×10^3 s^{-1} as compared to the passive spectra which has a yield of just 9.23×10^1 s^{-1}, a factor of 16.6; this indicates that the recorded passive yield is only 6.0% that of the active measurement yield. In contrast, a high-energy yield may be formed by integrating the response in the region of interest. Integrating the spectral response from 3 MeV and above, the active measurement has a high-energy yield of 5.94×10^1 s^{-1}, while the passive measurement has a high-energy yield of just 1.97×10^{-1} s^{-1}. This is a drastic difference as compared to the overall yield. The difference between the high-energy active and passive yields is a factor of 302, indicating that for the high-energy yield, the recorded passive target response is just 0.33% that of the active inspection high-energy γ-ray response. The response difference of this high-energy region as compared to the full energy range indicates a potential for a signature with increased sensitivity utilizing a measurement formed from the high-energy γ-ray response, and will be revisited momentarily. These results are summarized in Table 5.1.

As for the neutrons, the nature of the time response of the γ-rays is of interest in constructing a viable signature of fission. Figure 5.2 shows the detected response for three targets. Figure 5.2(a) illustrates the time response for all photons recorded following the bremsstrahlung pulse (incident on the target at time $t = 0$ s), for three targets, a 2.6 kg depleted uranium target (spectral data shown previously in Figure 5.1), a 1.5 kg thorium target, and a non-fissionable metal target, 6.0 kg of lead; the corresponding recorded energy spectra for each of the targets are also shown together, Figure 5.2(b). The high density lead target exhibits comparable scattering properties as the large fission targets of interest, and is therefore utilized as an active background

target for the metal depleted uranium and thorium targets. The targets utilized are summarized in Table 5.4, following further target discussions.

As for the previous neutron results, a rapid decrease in the response is observed for all targets within the first few tens of milliseconds, but the yield remains elevated for the ^{238}U and ^{232}Th targets throughout the remainder of the time window, as compared to the lead response, which is utilized for an active background target. Although an elevated yield is observed for the fissionable materials, it is not as strong as the sensitivity observed in the delayed neutron responses studied previously, particularly as these results utilize very large target masses as compared to the previous aqueous targets. Realizing that significantly smaller signals overall would be expected in comparison to the previous studies, due to the experimental geometry, does not diminish an expectation of greater potential sensitivity in distinguishing fissionable targets of interest from background. As the detectors are at much greater distances here than for the previous studies, it is expected that the detectable target emissions will diminish with the decreased solid angle (the emitted flux at the detector will decrease as $1/R^2$ with increasing separation), so too will the beam on target and thus the induced fission events. However, the corresponding decrease in measurable response will affect all targets, and is a distinguishable issue from the capability of the signature to differentiate the presence of fissionable isotopes within the target. This ability to identify the presence of isotopes of interest is a reflection of the sensitivity

Table 5.1: Summary of the yield responses for the active and passive measurements shown in Figure 5.1; the yields are formed utilizing the full energy response of the spectra, and using only high-energy γ-rays , $E_\gamma \geq 3$ MeV.

Active Yield (s^{-1})	Passive Yield (s^{-1})	Ratio of Active to Passive Responses
	Total Yield	
$1.529 \times 10^3 \pm 2.5 \times 10^1$	$9.230 \times 10^1 \pm 1.32 \times 10^0$	16.56
	High-Energy Yield	
$5.944 \times 10^1 \pm 2.029 \times 10^1$	$1.972 \times 10^{-1} \pm 7.36 \times 10^{-2}$	301.5

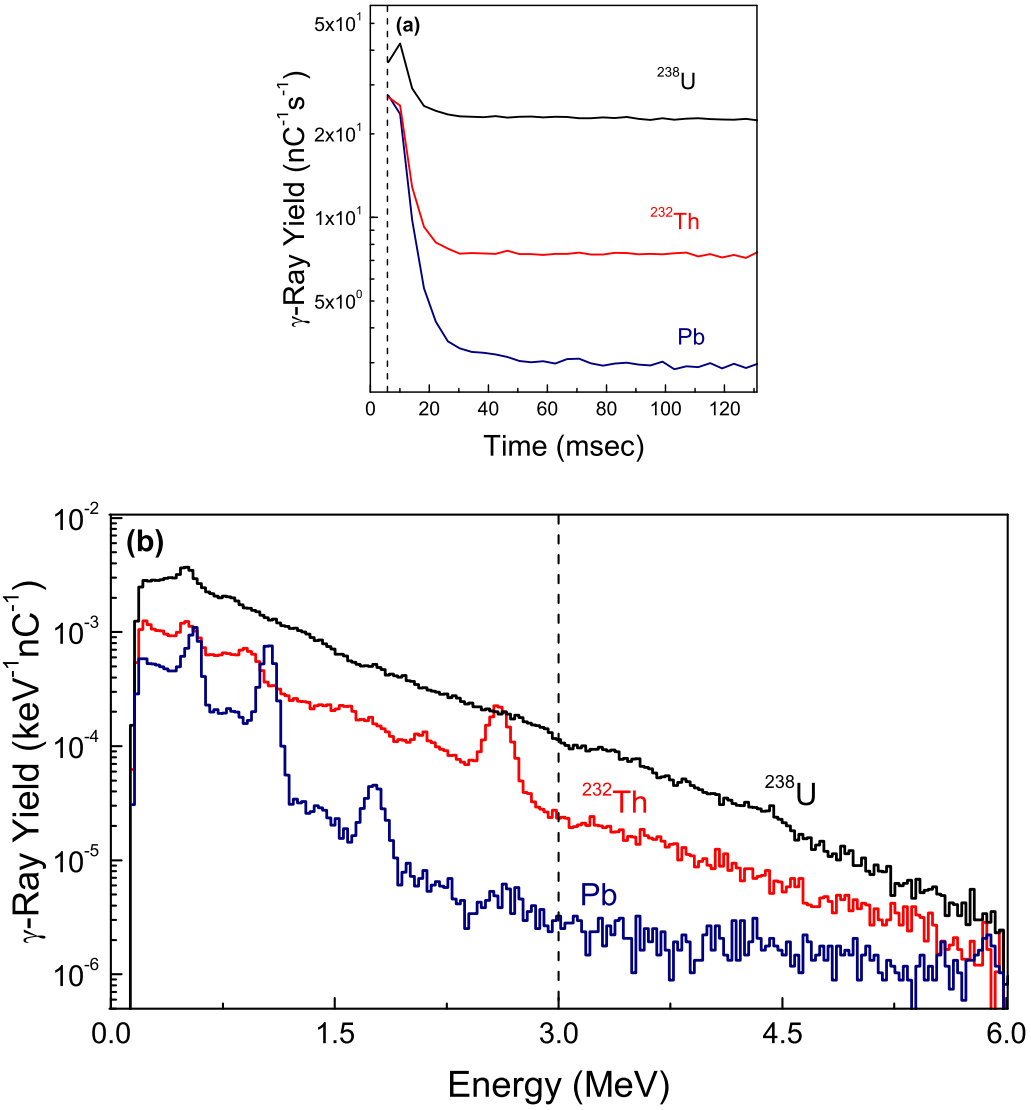

Figure 5.2: (a) The time response behavior of all recorded photons for three metals targets, depleted uranium (2.6 kg), thorium (1.5 kg) and lead (6.0 kg), normalized to the total acquisition charge and the time bin width. The BGO detector array was gated off for the first 6 ms of data acquisition, indicated in the Figure. (b) The corresponding recorded energy spectra are shown for the three targets, with spectra normalized to the total charge on target and the energy bin width; spectra have been rebinned for visual presentation. The 3 MeV energy relevant to the discussion is indicated, although there is no energy cut of the data. Data was recorded for ∼5 minute inspection windows on each target with beam parameters of 16 MeV and 7.5 Hz. The targets utilized are summarized in Table 5.4.

of the signature.

Integrating the γ-ray responses of Figure 5.2(a) from 30 ms and beyond results in a yield of 2.359 nC^{-1} for the depleted uranium target and a yield of 3.123×10^{-1} nC^{-1} for the lead target, the depleted uranium response a factor of 7.55 times greater than the background; the thorium target has a yield of 7.638×10^{-1} nC^{-1}, a factor of just 2.45 times the lead targets active background response. Although a discernable difference in the yields of these targets, a stronger separation of results for fission isotopes is clearly desirable. It is relevant to consider the high–energy γ-ray response as discussed regarding Figure 5.1. Figure 5.2(b) further indicates that the active uranium response is significantly stronger than the active lead response, even extending to the very high energies where there is considerably less yield in the targets. In the low energy region, distinct peaks are observed in the active background (lead) target. Although characteristic peaks would be expected in the uranium spectral response as well, in this case they are obscured by the high yield across the entire energy spectra and by the relatively poor resolution of the BGO detectors; some discrete peaks are observable in the thorium target spectra, attributable to the natural decay chain of thorium and not to discrete fission fragment emissions. It should be noted that the BGO resolution is significantly reduced as compared to other solid state detectors such as high purity germanium (HPGe) detectors, which have been utilized for active inspection discrete peak identification studies [68]; improved detector resolution greatly enhances the experimental capability to identify discrete peaks of interest within high rate spectra. However, for these studies, yield alone suffices to provide relevant signatures, and peak identification is therefore not relevant, beyond noting the significant background contributors. For consideration of defining a high-energy region of interest, the most potentially problematic background contributor is the commonly observed 2.6 MeV ^{208}Tl peak from the thorium natural decay chain and is found in many common materials. The presence of the 2.6 MeV ^{208}Tl decay peak is often indicative of naturally occurring radioactive material (NORM); avoiding inclusion of this peak within the signature definition may prevent false anomalously high responses in otherwise uninteresting targets of inspection. Any target containing significant amounts of fissionable isotopes, even NORM, would be expected to produce

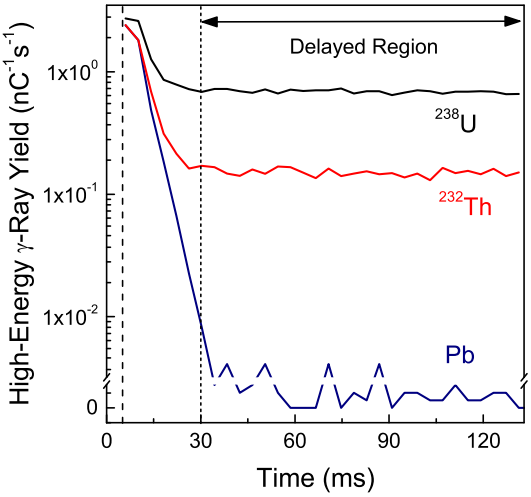

Figure 5.3: The time response behavior of the recorded high-energy γ-ray spectra; data is as for Figure 5.2 but with only photons 3 MeV to 6 MeV selected. Again, data was recorded for $\sim$5 minute inspection windows with beam parameters of 16 MeV and 7.5 Hz for three metals targets, depleted uranium (2.6 kg), thorium (1.5 kg), and lead (6.0 kg); results have been normalized to the total acquisition charge and the time bin width. All BGO detectors are gated off for the first 6 ms, and the delayed region of 30 ms and beyond is indicated in the Figure. The Yield axis has been clipped and indicates a linear scale below the axis break and a logarithmic scale above it, in order to better view the results.

significant delayed neutron signal or higher energy delayed γ-ray responses so as to be otherwise detectable.

Given the spectral responses discussed above, a signature can be considered utilizing only high-energy γ-rays. Selecting 3 to 6 MeV as the energy region of interest, in order to give the 2.6 MeV ^{208}Tl background peak a wide berth, the time response of these high-energy γ-rays may be analyzed. Figure 5.3 shows the time response behavior of the high-energy γ-rays for the same pair of metal targets shown previously; to be explicit, these are the same measurements shown in Figure 5.2, but only incident γ-rays with energy $\geq$ 3 MeV are now considered.

In the case of the high-energy γ-rays, there is now a much stronger partition observed between the fissionable and non-fissionable target time responses. As previ-

ously, following the initial very rapid early time decay, the ^{238}U and ^{232}Th responses remain sustained through the extent of the acquisition time window; the active background lead response now falls away by several orders of magnitude. Thus, by again defining an appropriate time window, a signature of fission may be formed through the use of time–delayed high–energy γ–rays [68, 96–99]. In contrast to the full energy range yields obtained with reference to Figure 5.2(a), there is now significantly more separation between the isotopes of interest and the active background responses, due principally to the significant reduction in the background rate utilized. The total delayed γ-ray yield of the lead background target of 3.123×10^{-1} nC^{-1} amounts to a background count rate of approximately 260.4 counts per second; by comparison, the high-energy delayed γ-ray yield is 2.110×10^{-4} nC^{-1}, which amounts to a background count rate of just 1.759×10^{-1} s^{-1}, a change in the signal's background rate by more than three orders of magnitude. The greatly reduced background signal translates to significantly improved detection sensitivity. Integrating the high-energy γ-ray responses from 30 ms and beyond results in high-energy yield values of 7.151×10^{-2} nC^{-1} for ^{238}U, 1.566×10^{-2} nC^{-1} for ^{232}Th, and 2.110×10^{-4} nC^{-1} for lead; this represents a ^{238}U signal 338.8 times stronger than that of the active background and a ^{232}Th signal 74.19 times stronger than that of the active background, an improvement in the overall detection sensitivity by a factor of 30.33 for thorium and 44.86 for uranium, or of at least 3000%.

The delayed γ-ray signature utilized for the remainder of these results employs the use of these high-energy γ-ray responses, and is defined as all recorded γ-rays with energy 3 – 6 MeV occurring at time $t \geq$30 ms, as the delayed γ-ray time window was selected for these measurements to be 30 ms and beyond.

Further characterization of the delayed γ-ray signature of fission is of clear interest. Additional experimental studies outside of this work have been completed in parallel within the academic group of this dissertation's advisor, Dr. Alan Hunt. The detailed thesis outcomes of these studies are recommended for further reading as relates to the study of the high-energy delayed γ-ray signatures of fission. The Master's thesis of E.S. Cárdenas, Idaho State University (2009) [96], focused on the detection of fissionable materials utilizing bismuth germanate and sodium iodide detectors for

high-energy delayed γ-ray signatures. The Master's thesis of E.T.E. Reedy, Idaho State University (2011) [68], utilized discrete delayed γ-rays for isotopic identification relevant to nuclear forensics applications.

5.3 Signature Responses to Mass

Further characterization of the signature is of clear interest. The inference of potential detection capabilities built on delayed signatures requires assessment of the relevant signal strengths, in order to determine the feasibility of measurements. Establishing the signature response dependencies on changing target mass is of principle importance in establishing whether or not the delayed signatures may be utilized to extract target information, beyond the detection of fissionable isotopes.

5.3.1 The Mass-Yield Relation of the Delayed γ-Ray Response

The aqueous targets defined in Table 3.1 were utilized to study the delayed γ-ray yield response as a function of the fissionable mass of the target within the low mass region of interest. Data was acquired on each target for a $\sim$10 minute inspection window with beam parameters of 16 MeV and 7.5 Hz, and all BGO detectors were gated off for the first 6 ms following the accelerator gun trigger; the delayed γ-ray yield has been defined previously to be $E_\gamma \geq 3$ MeV, $t \geq 30$ ms. All yield responses have been normalized to the total acquisition charge and are active background subtracted, using either a water target response for the aqueous solution targets or a lead target response for the metal targets. The response of the aqueous uranium targets are shown in Figure 5.4(a), where a very linear yield increase is observed with increasing ^{238}U target mass; a least squares linear regression value of $dY/dm = 7.121 \times 10^{-5}$ nC^{-1}·g^{-1} $\pm$ 5.7×10^{-7} nC^{-1}·g^{-1} with $R^2 = 0.9997$ were obtained, and the fit is indicated in the figure. Similarly, the response of the aqueous thorium targets are shown in Figure 5.4(b), where a very linear yield increase is again observed with increasing ^{232}Th target mass; least squares linear regression value of

Table 5.2: Summary of the high-energy delayed γ-ray target yield response to fissionable mass, results of Figure 5.4. Results for the aqueous uranium series were obtained from the linear regression illustrated in Figure 5.4(a), and results for the aqueous thorium series were obtained from the linear regression illustrated in Figure 5.4(b).

Isotope	Intercept $nC^{-1} \cdot g^{-1}$	dY/dm $nC^{-1} \cdot g^{-1}$	$\sigma_{dY/dm}$ $nC^{-1} \cdot g^{-1}$	R^2
^{232}Th	$(5.625 \pm 7.534) \times 10^{-5}$	2.893×10^{-5}	$\pm 1.05 \times 10^{-6}$	0.9948
^{238}U	$(0.834 \pm 3.589) \times 10^{-5}$	7.121×10^{-5}	$\pm 5.7 \times 10^{-7}$	0.9997

$dY/dm = 2.893 \times 10^{-5}$ nC^{-1}·g^{-1} $\pm$ 1.05×10^{-6} nC^{-1}·g^{-1} with $R^2 = 0.9948$ were obtained, and the fit is indicated in the figure. However, extending the mass-yield response to the high target mass region of the metal targets clearly illustrates deviations; at high mass, the observed yields are no longer linearly correlated to the target mass. The low mass uranium targets and extended dY/dm fit obtained from Figure 5.4(a) are shown with the metal depleted uranium target yield in Figure 5.4(c), where the uranium metal target yield is observed to be significantly lower than would be calculated using the dY/dm value obtained. A yield of 1.852×10^{-1} nC^{-1} $\pm$ 1.5×10^{-3} nC^{-1} would be expected for a target mass equal to 2.6 kg, but a net yield of just 7.333×10^{-2} nC^{-1} $\pm$ 5.3×10^{-4} nC^{-1} was observed, only 39.6% of the expected value. A similar effect is seen when the thorium metal target is considered. The low mass thorium targets and extended dY/dm fit obtained from Figure 5.4(b) are shown with the metal thorium target yield in Figure 5.4(d), where the thorium metal target yield is also observed to be significantly lower than the extended dY/dm value; a yield of 4.346×10^{-2} nC^{-1} $\pm$ 1.58×10^{-3} nC^{-1} would be expected for a target mass equal to 1.5 kg, but a net yield of just 1.575×10^{-2} nC^{-1} $\pm$ 2.6×10^{-4} nC^{-1} was observed, only 36.2% of the expected value. The dY/dm values obtained from the linear regression fits are summarized in Table 5.2.

The attenuation of photons within the target is significant, and results in the observed reduced yield values. The mass attenuation coefficient for uranium, given

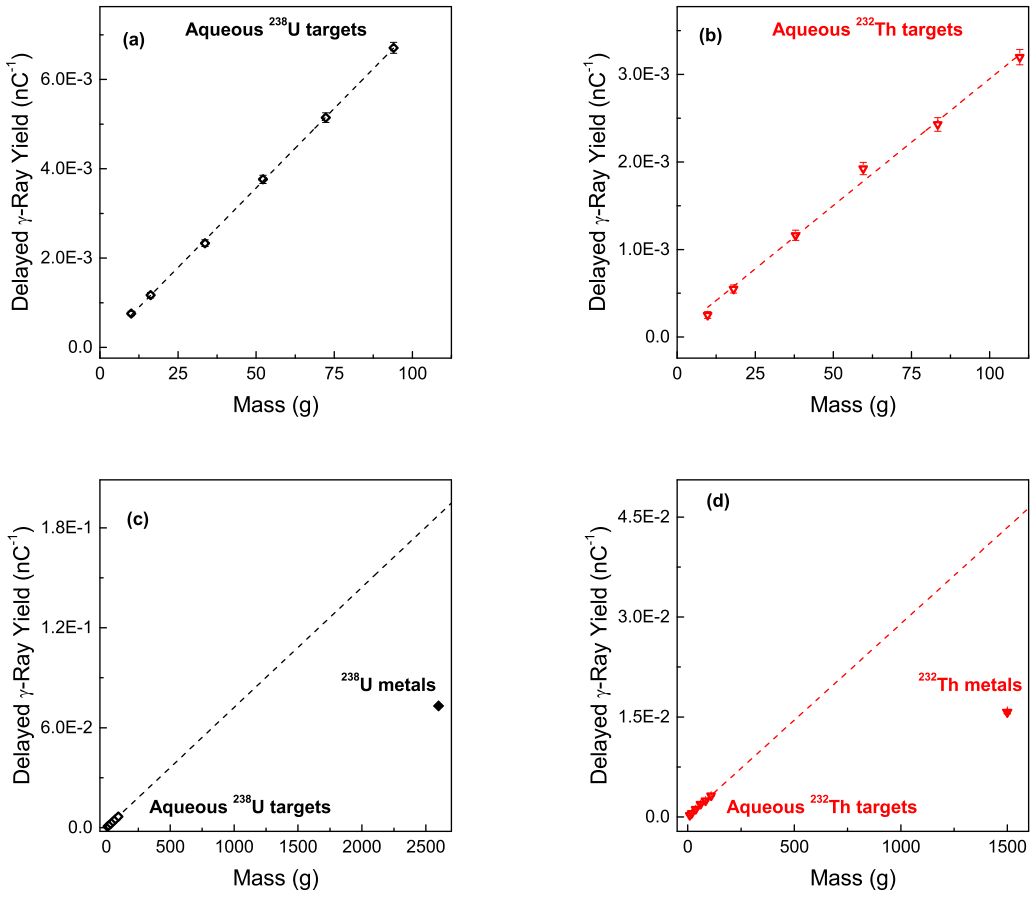

Figure 5.4: The net delayed γ-ray yields shown as a function of the fissionable mass present in the target, for two isotopes of interest, (a), (c) ^{238}U and (b), (d) ^{232}Th. (a)-(b) The low mass aqueous targets, as defined in Table 3.1, were utilized to study the delayed γ-ray yield response as a function of the fissionable mass of the target. Very linear correlations are observed between the yields and the target masses for both (a) ^{238}U and (b) ^{232}Th; least squares linear fits were obtained for each and are indicated in the respective Figures. (c)-(d) Extending the dY/dm linear fits obtained from the aqueous targets to the high mass regions presents a notable issue: the observed delayed γ-ray yield is much lower than would be expected, indicating non-linear yield response to mass, with suppressed yield observed in both (c) a 2.6 kg metal ^{238}U target and (d) a 1.5 kg metal ^{232}Th target. All yield responses have been normalized to the total acquisition charge and have been active background subtracted, using a water target for the low mass solutions and a lead target for the metal fissionable targets. Data was acquired on each target for a $\sim$10 minute inspection window with beam parameters of 16 MeV and 7.5 Hz, and all BGO detectors are gated off for the first 6 ms following the accelerator gun trigger; the delayed γ-ray region was defined previously to be all $E_\gamma \geq 3$ MeV at $t \geq 30$ ms.

by the NIST Standard Reference Database 126 [100], would indicate an average half-depth of only 0.61 cm for even 15 MeV photons. The depleted uranium target utilized for these measurements consisted of two 9.1 cm square plates, placed back to back to form a single target, calculated to be approximately 1.64 cm thick; this target thickness connotes low probability that even high-energy bremsstrahlung photons would penetrate the full target thickness to induce fission, thus reducing the overall fissionable mass available for detection. Further, resultant 'deep-target' γ-rays would be shielded from the detector array by attenuation within the target itself. Using as an example 5 MeV delayed γ-rays and the corresponding mass attenuation coefficient, the calculated probability of escaping 1.64 cm of depleted uranium is only $\sim 24.7\%$. The additional metal targets considered, thorium and lead, are also very high density materials, and similar attenuation effects are encountered in these targets. As these potential effects were well know prior to the experimental execution, some efforts were made to mitigate their impact. The large mass plate targets, lead and depleted uranium, were placed at a 45° angle with respect to the beam, exposing a target face to the BGO detector array, and minimizing the combined reaction penetration and escape distances involved. The thorium target consisted of a series of cylinders, so modification of their physical placement was not required. Although these self-shielding effects likely contribute the large fraction of the reduced yield results observed, it is also possible that the overall photon flux available to the target may be insufficient at the distances involved. If the photon beam flux is unable to saturate the target then the overall fission rate within the target would be quenched, reducing the total fissionable mass available for detection. The potential contribution of photon flux effects was not investigated as part of these experimental campaigns, although it seems unlikely that this would be a significant contributor. Further studies monitoring the photon flux utilizing an array of beam flux monitors or activation foils placed at various points with respect to the target could prove informative, but are not central to the desired outcomes of these studies.

The delayed γ-ray signal responses are linear and strongly correlated to the fissionable target mass in the low mass region, up to $\sim$100 g. Although the delayed γ-ray signal responses are not linearly correlated to fission mass in the high mass

Table 5.3: Summary of the delayed neutron target yield response to fissionable mass, results of Figure 5.5. Results for the aqueous uranium series were obtained from the linear regression illustrated in Figure 5.5(a), and results for the aqueous thorium series were obtained from the linear regression illustrated in Figure 5.5(b).

Isotope	Intercept $nC^{-1} \cdot g^{-1}$	dY/dm $nC^{-1} \cdot g^{-1}$	$\sigma_{dY/dm}$ $nC^{-1} \cdot g^{-1}$	R^2
^{232}Th	$(7.0 \pm 6.0) \times 10^{-5}$	6.286×10^{-5}	$\pm\ 8.3 \times 10^{-7}$	0.9993
^{238}U	$(3.1 \pm 1.5) \times 10^{-4}$	1.735×10^{-4}	$\pm\ 2.4 \times 10^{-6}$	0.9992

region beyond this, there is still a strong signal, indicating the presence of both fission isotopes considered, ^{238}U and ^{232}Th. Thus the signal may clearly be utilized for detection, but extrapolating fission mass information beyond the low mass regime is compromised. This presents evidence to consider the shielded target studies as two distinct scenarios, separating low mass target detection and high mass target detection, but does not diminish the capability of the delayed γ-ray signal to infer the presence of fissionable material.

5.3.2 The Mass-Yield Relation of the Delayed Neutron Response

As for the previous γ-ray results, the aqueous targets defined in Table 3.1 were utilized to study the delayed neutron yield response as a function of the fissionable target mass. All yield responses have again been normalized to the total acquisition charge and active background subtracted, using either the water target response for the aqueous solution targets or the lead target response for the metal targets. The response of the low mass uranium targets are shown in Figure 5.5(a), where a very linear yield increase is observed with increasing ^{238}U target mass, as was observed for the previous delayed neutron results, in the much tighter experimental geometry; least squares linear regression values of $dY/dm = 1.735 \times 10^{-4}$ nC^{-1}·g^{-1} $\pm\ 2.4 \times 10^{-6}$ nC^{-1}·g^{-1} with $R^2 = 0.9992$ were obtained, and the fit is indicated

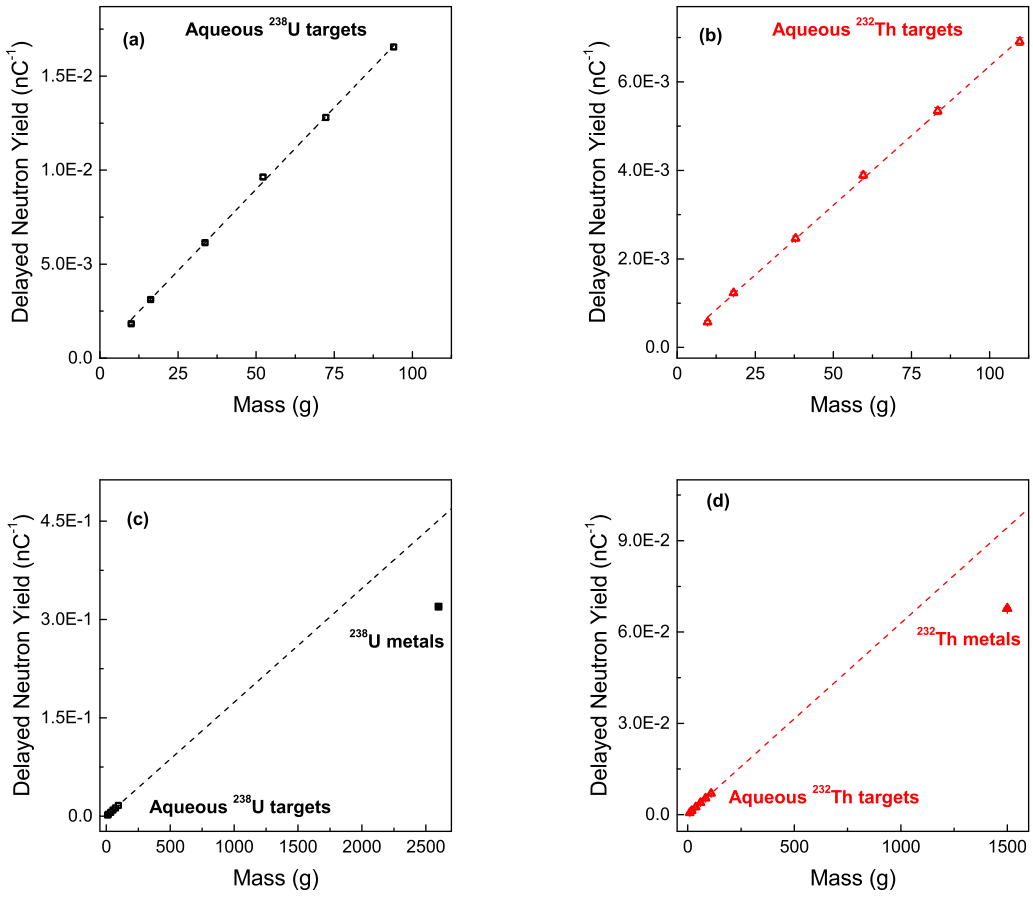

Figure 5.5: The net delayed neutron yields shown as a function of the fissionable mass present in the target for two isotopes of interest, (a), (c) ^{238}U and (b), (d) ^{232}Th. (a)-(b) The low mass aqueous targets, as defined in Table 3.1, were utilized to study the net delayed neutron yield response as a function of the fissionable mass of the target. The yield responses have been normalized to the total acquisition charge and background subtracted, utilizing the water target as the active background. Very linear correlations are observed between the delayed neutron yields and the target masses for both (a) ^{238}U and (b) ^{232}Th; least squares linear fits were obtained for each and are indicated in the respective figures. (c)-(d) Just as was observed in the delayed γ-ray signature, extending the neutron dY/dm results obtained from the aqueous targets to the high mass regions presents a notable issue: the observed yields are lower than expected, indicating non-linear yield response to mass, with suppressed yield observed in both (c) a 2.6 kg metal ^{238}U target and (d) a 1.5 kg metal ^{232}Th target. Metal target responses have been normalized to the total charge on target and active background subtracted using a 6.0 kg lead target for the background. Data was acquired on each target for a ∼10 minute inspection window with beam parameters of 16 MeV and 7.5 Hz; the delayed neutron region was defined previously to be all $t \geq 30$ *ms*.

in the figure. The response of the low mass thorium targets are shown in Figure 5.5(b), where a very linear yield increase is also observed with increasing ^{232}Th target mass; least squares linear regression values of $dY/dm = 6.286 \times 10^{-5}$ nC^{-1}·g^{-1} $\pm$ 8.3×10^{-7} nC^{-1}·g^{-1} with $R^2 = 0.9993$ were obtained, and the fit is again indicated in the figure. Extension of the yield per mass response to the high mass region indicates nonlinear deviation in the yield response, as for the delayed γ-ray signal, although the suppression in expected results is not as significant. The results for the uranium dY/dm response is shown together with the metal depleted uranium target yield in Figure 5.5(c); an expected yield of 1.852×10^{-1} nC^{-1} $\pm$ 1.5×10^{-3} nC^{-1} may be calculated for the 2.6 kg target mass, while a yield of 7.333×10^{-2} nC^{-1} $\pm$ 5.3×10^{-4} nC^{-1} was observed, approximately 70.9% of the expected yield. The results for the metal thorium target prove to be similar. Figure 5.4(d) indicates the extended dY/dm fit obtained from Figure 5.4(b) with the metal thorium target yield; an expected yield of 9.44×10^{-2} nC^{-1} $\pm$ 1.3×10^{-3} nC^{-1} is calculated for the 1.5 kg target, while a net yield of 6.772×10^{-2} nC^{-1} $\pm$ 2.6×10^{-4} nC^{-1} was observed, approximately 71.8% of the expected yield. Thus it is clear that although the non-linearity effects observed are not as significant as for the delayed γ-ray response, they still serve to prevent direct correlation between the total observed delayed neutron yield and the fissionable target mass beyond the well-characterized low mass regions. As for the delayed γ-ray discussion previously, target self attenuation is culpable for the non-linear response of the delayed neutron signal to fission mass. Thus the delayed neutron signature may be utilized to elucidate the presence of fissionable isotopes of interest, but care should be taken when trying to extrapolate further target information, at least in the case of suspected large mass objects.

5.4 Signature Responses Under Shielding Effects

Two distinct yet parallel signatures of fission have now been defined, utilizing delayed neutrons and high-energy delayed γ-rays to construct the approaches. Although further characterization of the γ-ray signature could prove of interest, as these methods of detection and identification would be redundant to the delayed neutron

characterization methods previously defined, a study contrasting the detection capabilities as defined by these signatures was preferred. Further, as applications such as cargo screening are of clear interest, an experimental campaign which focused on the potential shielding of detection signatures was undertaken.

Two materials were chosen for the target shielding studies, a low-Z material, borated polyethylene, and a high-Z material, lead, to highlight the contrasting natures of potential shielding concerns due to neutron and γ transport effects in material. The low-Z shielding material, polyethylene, has high hydrogen content and thus serves as a fairly opaque scattering target for neutrons, but has a low density which ineffectively scatters high-energy γ-rays. In contrast, the high-Z shielding material, lead, much more effectively scatters high-energy γ-rays, but results in a relatively large neutron interaction path length. These two materials were selected to provide information for extreme limiters of each signature for potential shielding considerations. Further study of other materials which may serve to provide simultaneous signature moderation for both gamma and neutron effects, or a study of mixed or alternated shielding material effects, would be warranted for system specific characterization, and likely would be optimally studied under through simulation. However, the potential for these combined shielding effects lies beyond the scope of this experimental campaign and will not be discussed further.

Signature responses were studied at a number of thicknesses for each shielding material. Standard beam parameters of 7.5 Hz at 16 MeV for 5-minute interrogation windows were selected for each target, as determined by previous studies. Lead shielding thicknesses of (0 cm), 2.54 cm, 5.08 cm, 10.16 cm, 15.24 cm, and 20.32 cm were utilized, and borated polyethylene thicknesses of (0 cm), 5.08 cm, 10.16 cm, 15.24 cm, 20.32 cm, 25.40 cm, and 30.48 cm were utilized. At each shielding configuration, six targets were investigated. Three aqueous targets were utilized to investigate low-mass signatures, a pure water target for active background measurements, and two solutions containing fissionable mass, 59.6 g of ^{232}Th (target $Th-5$) and 72.3 g of ^{238}U (target $U-6$). Three additional metal were utilized to investigate a higher mass region, consisting of a 6.0 kg lead target for active background measurements, and two fissionable mass targets, 2.6 kg of depleted uranium and 1.5 kg of thorium

Table 5.4: Summary of experimental targets utilized for shielded signature studies.

Target	Isotope of Interest	Fissionable Mass
	Aqueous Targets	
Th-5	^{232}Th	59.6 g
U-6	^{238}U	72.3 g
H_2O		
	Metal Targets	
Th cylinders	^{232}Th	1.5 kg
DU plate	^{238}U	2.6 kg
Pb brick (6.0 kg)		

metal. As greater fissionable mass results in increased signature response, simultaneous investigation of low-mass targets (i.e. gram levels of fissionable material) and high-mass targets (i.e. kg levels) under shielding allows a systematic probe of the effects of shielding on signatures for two distinct scenario studies. Although high-mass material may potentially pose more illicit transport risk, the resultant signature levels are likely to be much more readily detectable. In contrast, the low-mass targets have smaller signature. However, the previous results (delayed neutron studies) have indicated strong detection capabilities; testing these potential capabilities under shielding pertubations is pertinent to the applicability of the signature. The shielded target campaign targets which were utilized are summarized in Table 5.4.

5.4.1 Effects of Shielding on the Delayed γ-Ray Signal

The high-energy delayed γ-ray yield responses are shown as a function of shielding thickness for several scenarios in Figure 5.6(a)-(d). The delayed γ-ray responses are indicated for the high mass metal targets as a function of target shielding thickness for 5.6(a) borated polyethylene shielding and 5.6(b) lead shielding. Figures 5.6(c) and 5.6(d) indicate the delayed γ-ray response for the low mass aqueous targets, again shown as a function of target shielding thickness for 5.6(c) borated polyethylene

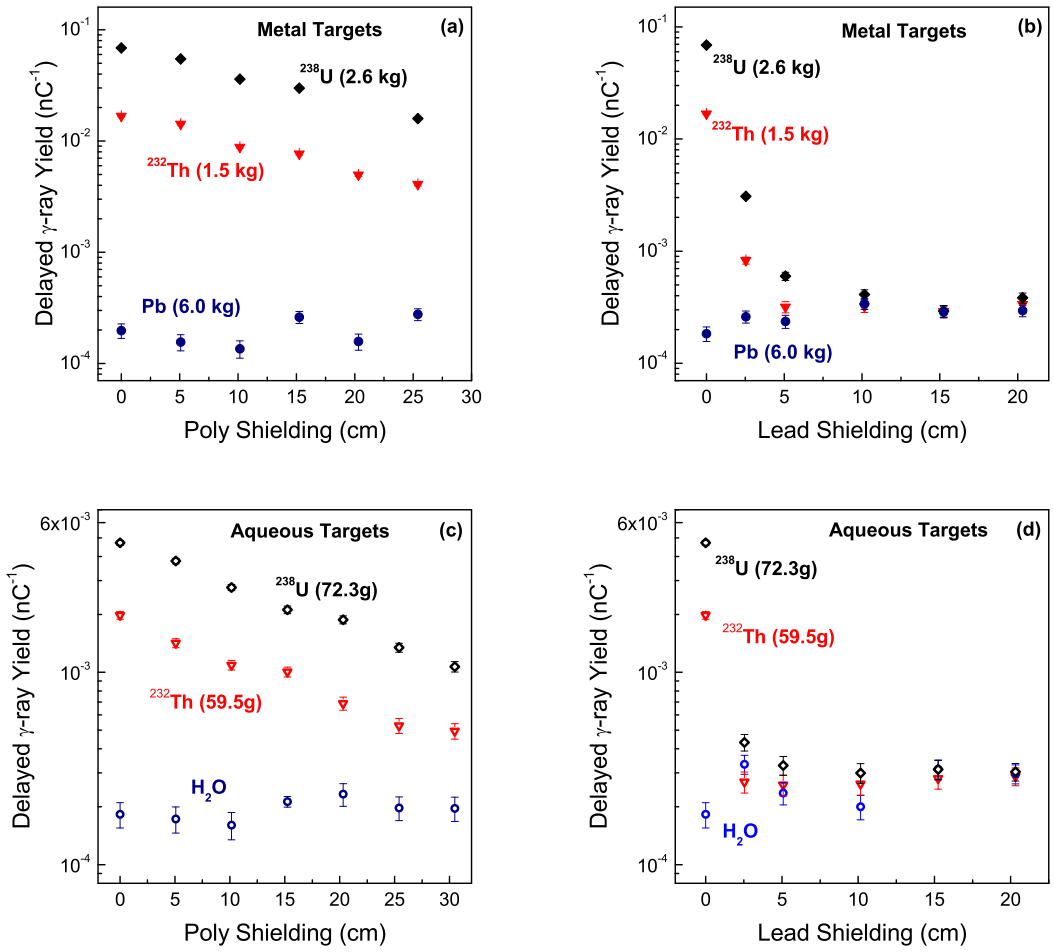

Figure 5.6: The high-energy delayed γ-ray yield responses shown as a function of thicknesses for two shielding materials, in each of two target scenarios, high mass metal targets and low mass aqueous solution targets. (a)-(b) The delayed gray yield responses for three metal targets, 1.5 kg of ^{232}Th, 2.6 kg of ^{238}U and a 6.0 kg lead target utilized for active background, shown as a function of the shielding thickness for (a) borated polyethylene shielding and (b) lead shielding. (c)-(d) The delayed γ-ray yield responses for three aqueous targets, solutions containing 72.3 g of ^{238}U and 59.5 g of ^{232}Th, and a pure water target utilized for active background, shown as a function of the shielding thickness for (c) borated polyethylene shielding and (d) lead shielding. The delayed γ-ray yields are obtained for each target configuration by summing the high-energy delayed γ-ray response for the detector array, normalized to the total charge incident on the radiator, as a proxy for the bremsstrahlung intensity. Data was recorded for inspection windows of ∼5 minutes on each target with beam parameters of 16 MeV and 7.5 Hz.

shielding and 5.6(d) lead shielding. It is clear from these figures that the delayed γ-ray signature survives quite well through even significant amounts of polyethylene, but falls off dramatically with lead shielding. The characteristic behavior of the responses is consistent between the high mass and the low mass targets. At 0 cm of shielding, the metal yields are ^{238}U: $(6.871 \pm 0.054)\times10^{-2}$ nC^{-1}, ^{232}Th: $(1.673 \pm 0.026)\times10^{-2}$ nC^{-1}, and Pb: $(1.971 \pm 0.291)\times10^{-4}$ nC^{-1}. The lead responses are included to provide clear representation of the background environment, rather than active background subtracting the fissionable mass responses. The yield response of any target without shielding may be denoted as Υ_0 and will be referenced for the comparison of further shielding results against these values. By 10.16 cm of borated polyethylene shielding, the yield values have dropped to 52.4% of Υ_0 for ^{238}U, 52.6% of Υ_0 for ^{232}Th, and 68.8% of Υ_0 for Pb. At even 30.48 cm of borated polyethylene the yield values are still strong indicators of the presence of fissionable material, measuring 17.8% of Υ_0 for ^{238}U, 16.6% of Υ_0 for ^{232}Th, and 75.2% of Υ_0 for Pb; the measured yield for the uranium target is still a factor of 82.6 or 52.94σ above the lead background, and the thorium signal a factor of 18.79 or 23.18σ above background. The drop in signal with respect to increasing polyethylene shielding is a slow and steady decrease, with a separation which is still differentiable even at significant thicknesses. The response of the low mass targets to the borated polyethylene shielding is similar. At 30.48 cm of shielding the measured yield values are 22.7% of Υ_0 for ^{238}U, 25.0% of Υ_0 for ^{232}Th, and 107% of Υ_0 for H_2O (H_2O: 1.96×10^{-4} nC^{-1} $\pm$ 2.8×10^{-5} nC^{-1}); the uranium solution in this case is a factor of 5.458 or 12.60σ above the background yield, the thorium solution a factor of 2.526 or 5.916σ above the background yield.

Fissionable material detection can also be considered in terms of the critical decision level, as defined in Equation 2.51. For the cases relevant to this discussion, the error in the water and lead target active backgrounds define the detection limits; the background may be considered in each case as the average of the series of recorded backgrounds at each shielding configuration, $\overline{\sigma_{bkg}}$, in order to better account for the spread of the measured background response. Utilizing symmetric false tolerances of 95% confidence levels, the calculated detection limits are $L_D = 1.702 \times 10^{-4}$ nC^{-1} for water and $L_D = 1.787 \times 10^{-4}$ nC^{-1} for lead. These calculated values define the

threshold for the detectable yield of the system with a 95% confidence in the detection capability. The experimentally measured yield responses to shielding thickness may be fit utilizing an exponential decay form; this is the known γ-ray attenuation form and corresponds to the visual linear correlations which Figure 5.6(a) and Figure 5.6(c) indicate. These fit parameters can then be utilized to extrapolate the shielding thickness at which the signal strength would be just equal to the calculated detection limit, establishing system detection constraints. The maximum borated polyethylene shielding thickness at which detection of the 2.6 kg ^{238}U metal target with a 95% confidence could be ensured would be ∼103.9 cm; this confidence limit would be reached at ∼77.2 cm of borated polyethylene for the 1.5 kg metal ^{232}Th target. The maximum borated polyethylene thickness at which a 95% confidence in the detection response could be ensured would be ∼68.29 cm for the ^{238}U solution and ∼51.7 cm for the ^{232}Th solution. To be clear, this result indicates that under these measurement conditions, using a stand off distance of ∼2.38 m, there is a 95% confidence in detecting the 72.3 g solution of ^{238}U surrounded by ∼68.3 cm of borated polyethylene utilizing the defined high-energy delayed γ-ray signature. Thus, the delayed γ-ray signature clearly survives very well against borated polyethylene shielding.

In contrast, at just 2.54 cm of lead shielding the delayed γ-ray yield appears to be already significantly compromised. The metal target yields have fallen to just 4.48% of Υ_0 for ^{238}U and 4.93% of Υ_0 for ^{232}Th, while the lead background signal is ∼132% of Υ_0, or a value of $(2.60 \pm 0.32)\times10^{-4}$ nC^{-1}. The metal targets, shown in Figure 5.6(b), are already within 1σ of the measured active background target at 10.08 cm of lead shielding; beyond this thickness of target shielding, there is no visible difference discernable between any of the targets. At 5.08 cm of lead shielding, the measured yield responses have fallen to 0.871% of Υ_0 for ^{238}U, 1.90% of Υ_0 for ^{232}Th; the measured active background lead target measures ∼120% of Υ_0. These results indicate very strong suppression of the delayed γ-ray signal.

Given their low fission mass and thus smaller signature to begin with, the aqueous targets prove difficult to discern at even 2.54 cm of lead shielding, using the delayed γ-ray responses. At 2.54 cm of lead shielding, the uranium solution has a measured

value of 9.17% of Υ_0, and lies within 1.47σ of the measured background response at 2.54 cm of shielding with a pure H_2O target; this background is ∼182% of the measured Υ_0 water response. The thorium solution yield, 13.62% of Υ_0, is indistinguishable from background. From the results of the small mass solutions, it is clear that the background yield responses increase from 0 cm to 2.54 cm of lead shielding, indicating higher detection rates of delayed γ-rays; this was also observed to be the case in the metal background lead target response, although it was a smaller fraction and therefore more difficult to discern. However, this small effect could be indicative of the increase of the bremsstrahlung scattering target, due to the lead target shielding placed upstream of the target; drawing any strong conclusions is challenging, given the small number of total counts involved. For example, the water target has a high-energy delayed γ-ray count rate at 0 cm of shielding of just 0.145 ± 0.022 sec^{-1}, compared to the high-energy delayed γ-ray count rate of 0.257 ± 0.029 sec^{-1} at 2.54 cm; this is a rate difference of a factor of 1.77, but a difference of only 34 total counts for the two different acquisitions. The delayed regions do not appear to be compromised, as can be seen in Figure 5.7, which shows the time response of the active background measurements, the water target at 0 cm, 2.54 cm, and 5.08 cm of lead shielding, and the lead target at 0 cm and 2.54 cm of lead shielding, for (a) the full acquisition time width and (b) the acquisition time width to 60 ms, to better illustrate the early time response; the spectra are not rebinned so as to convey the few counts nature of the late time region, where many zero count bins are observed. Given the small numbers of counts involved though, it is possible that some of the delayed time region events originate from events due to the increased scattering target of the lead shielding, such as (γ, n) to (n, γ) events which result in high-energy γ-rays at times longer than 30 ms; capturing even a small number of these events could plausibly affect the background count rates significantly enough to be noticeable, while further increases of shielding would mask this occurrence. Further investigation of lead shielding effects at thinner steps than 2.54 cm may be warranted in order to expand on potential ramifications of these effects.

A consequence of the lead shielding is the significant attenuation of the bremsstrahlung beam, which decreases the induced fission rates of the targets. As the

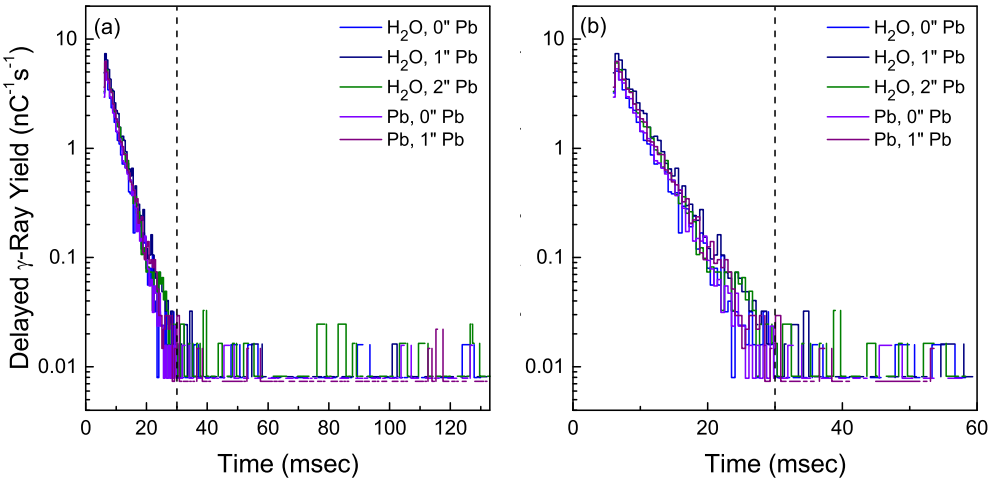

Figure 5.7: The delayed γ-ray time response behavior shown for a number of active background measurements, the water target at 0 cm, 2.54 cm, and 5.08 cm of lead shielding and the lead target at 0 cm and 2.54 cm of lead shielding. The responses are shown for (a) the full acquisition window of $\sim$ 133 ms and (b) the acquisition window to only 60 ms, with 30 ms indicated. The delayed time region does not appear to be compromised. Data was recorded for $\sim$ 5 minute inspection windows on each target with beam parameters of 16 MeV and 7.5 Hz.

shielding surrounds the target on all sides, the probing radiation must penetrate the increasing thicknesses of shielding material before reaching the interrogation target. Attenuation of the interrogation beam was expected to greatly challenge the detection capabilities; the effects were observed in the significantly decreased target yields at even the first 2.54 cm step of target shielding. Given that the mass-attenuation coefficient (for lead) is energy dependent, the beam attenuation varies with energy, but is sufficiently strong across the entire photon energy range so as to be problematic. At 2.54 cm of lead shielding, the approximate photofission threshold energy of 6 MeV (for ^{238}U, ^{232}Th) would have a photon intensity reduced by more than 70%; at 15 MeV the photon intensity is reduced by at least 80%. Nonetheless, fission events are still induced in the target, resulting in detectable delayed signals. Although these results seem daunting for potential detection scenarios, the delayed γ-ray response is only one of the fission signatures considered. It is beneficial to next consider the

delayed neutron yield responses to the target shielding materials.

5.4.2 Effects of Shielding on the Delayed Neutron Signal

The delayed neutron yield responses are now considered as a function of shielding thickness for the same shielded target scenarios, Figure 5.8(a)-(d). The responses are indicated for the high mass metal targets as a function of target shielding thickness for 5.8(a) borated polyethylene shielding and 5.8(b) lead shielding. Figure 5.8(c) and 5.8(d) indicate the delayed neutron response for the low mass aqueous targets, again shown as a function of target shielding thickness for 5.8(c) borated polyethylene shielding and 5.8(d) lead shielding. The figures indicate that the delayed neutron signature exhibits a steep decrease in response to both shielding materials; however, closer inspection of the data is clearly warranted.

Figure 5.8(a) illustrates the delayed neutron response of the metal targets to increasing borated polyethylene thickness; although the targets remain clearly detectable above background at 15.24 cm of shielding, by 20.32 cm of shielding the uranium lies only 1.891σ above the lead background and the thorium target response is no longer separable from background; beyond the 20.32 cm of target shielding, there is no discernable difference between any of the target responses. At 15.24 cm of borated polyethylene, the measured metal target delayed neutron yields are just 0.533% of Υ_0 for ^{238}U, only 0.789% of Υ_0 for ^{232}Th, and ~135% of Υ_0 for lead; the depleted uranium target is a factor of 17.2 or 4.64σ above the measured background, the thorium metals a factor of 5.00 or 2.16σ above the measured active background. Beyond this, at 20.32 cm of borated polyethylene, the depleted uranium target yield is just 0.135% of Υ_0, and a factor of only 5.96 or 1.89σ above the background yield; the measured active background lead target yield is ~99.23% of the Υ_0 obtained for lead; neither metal target is reasonably distinguishable from an active background measurement beyond 20.32 cm of borated polyethylene shielding. These results concur with the extrapolated shielding thicknesses at which the critical decision level threshold occurs, 26.69 cm of borated polyethylene for a 95% confidence of the 2.6 kg metal ^{238}U detection and 24.30 cm of borated polyethylene for a 95% confidence of the

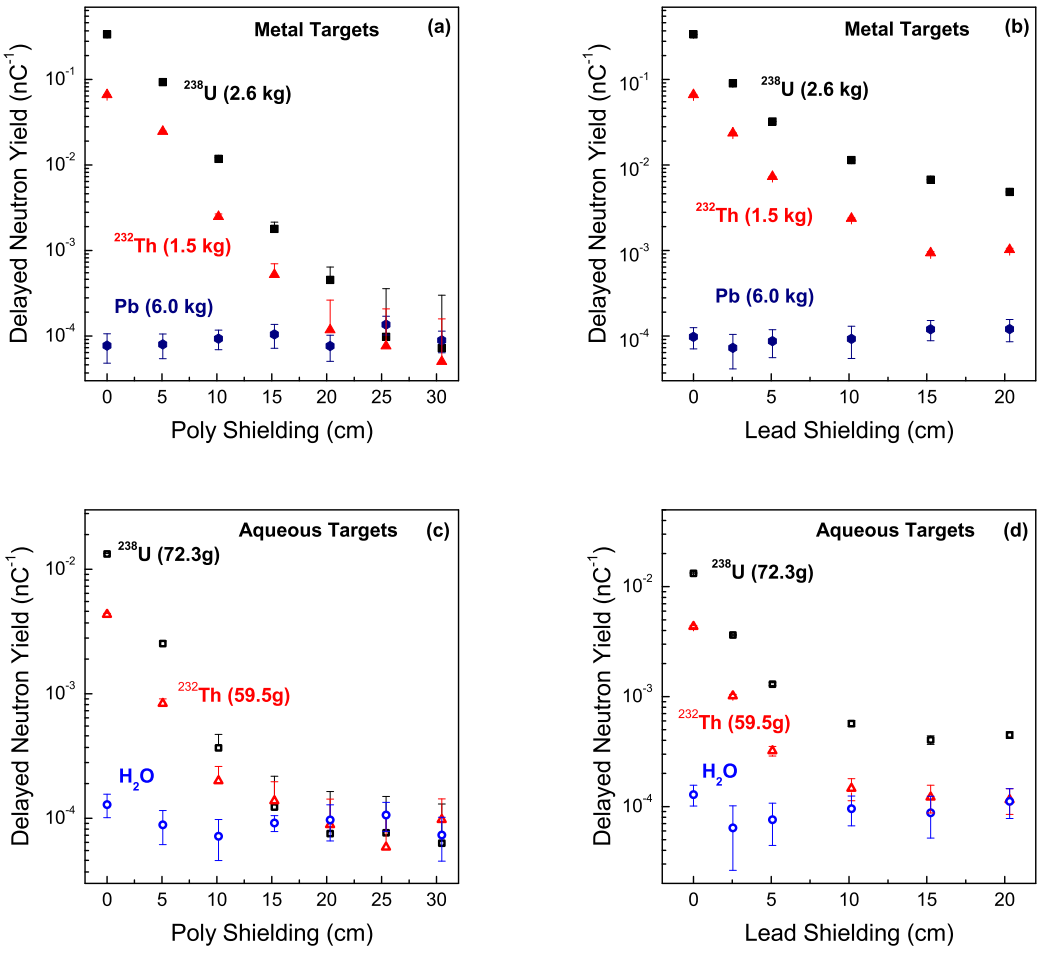

Figure 5.8: The delayed neutron yield responses shown as a function of thicknesses for two shielding materials, in each of two target scenarios, high mass metal targets and low mass aqueous solution targets. (a)-(b) The delayed neutron yield responses for three metal targets, 1.5 kg of ^{232}Th, 2.6 kg of ^{238}U and a 6.0 kg lead target utilized for active background, shown as a function of the (a) borated polyethylene shielding and (b) lead shielding thicknesses. (c)-(d) The delayed neutron yield responses for three aqueous targets, solutions containing 72.3 g of ^{238}U and 59.5 g of ^{232}Th, and a pure water target utilized for active background, shown as a function of the (c) borated polyethylene shielding and (d) lead shielding thicknesses. The yields are obtained for each target configuration by summing the delayed neutron response of the detector array, normalized to the total acquisition charge. Data was recorded for ∼5 minute inspection windows on each target with beam parameters of 16 MeV and 7.5 Hz.

1.5 kg metal ^{232}Th detection. The aqueous target responses are quenched even more rapidly by the target shielding due to their lesser fissionable masses. At 10.16 cm of borated polyethylene the measured uranium solution yield is just 2.78% of Υ_0, only 5.12 times higher or 2.60σ above background; the shielded active background response at 10.16 cm was ∼55.9% of Υ_0. The thorium solution yield, 3.76% of Υ_0, lies only 1.64σ above the active background, seen in the figure where the 1σ errors are indicated. Neither of the aqueous targets are distinguishable from an active background measurement beyond 10.16 cm of borated polyethylene shielding. Figure 5.8(b) and Figure 5.8(d) illustrate the delayed neutron signal responses to lead shielding of the target. In the case of the metal targets, Figure 5.8(b), it is clear that although the recorded results decrease rapidly with increasing shielding thickness, the detection of the depleted uranium target actually survives even 20.32 cm of lead target shielding; the thorium target does as well. At 20.32 cm of lead shielding the measured yield results for the metal targets are 1.44% of Υ_0 for ^{238}U, 1.55% of Υ_0 for ^{232}Th; the measured active background lead target response is ∼156% of Υ_0. At this maximum lead shielding thickness the depleted uranium target yield is still a factor of 40.15 or 116.7σ above the measured active background yield, and the thorium target is a factor of 8.498 or 23.14σ above the measured background yield, significant separation, and certainly quantifiable as detectable. Note that each of the delayed neutron yield values for the metal targets measured at 20.32 cm of lead shielding are in fact higher than the corresponding target yields measured at just 15.24 cm of borated polyethylene shielding. Thus, it is clear that the neutron signal succumbs to effects of borated polyethylene shielding much more rapidly than for lead shielding.

The aqueous target detection does not fare quite as well as the smaller yield responses are quenched more rapidly by the increasing target shielding, although the ^{238}U solution target response is still separable from the active background even at the full 20.32 cm of lead shielding. At 20.32 cm of lead shielding the measured aqueous target yields are 3.38% of Υ_0 of ^{238}U and 2.66% of Υ_0 of ^{232}Th; the active background is 86.77% of the H_2O Υ_0. This correlates to a uranium solution yield which is a factor of 4.01 or 9.48σ above the measured active background, although the measured thorium solution yield is approximately equal to the active background measurement

and therefore indistinguishable. The thorium target is in fact indistinguishable from background beyond 10.16 cm of lead shielding, where the yield measures $(1.46 \pm 0.33)\times10^{-4}$ nC^{-1} as compared to the active background water yield, which measures $(9.57 \pm 2.88)\times10^{-5}$ nC^{-1}, a separation of the thorium target above active background by a factor of only 1.53 or 0.651σ.

It is important to highlight again the significant effect which the lead shielding has on the induced fission rate within the target. The lead shielding's attenuation of the interrogating bremsstrahlung beam is the principle reason behind the reduced delayed neutron responses, rather than a shielding of the target neutron emissions. Even given a severe amount of lead target shielding, 20.32 cm surrounding the target on all sides, it is significant to reiterate that these results indicate that the metal targets of 2.6 kg ^{238}U and 1.5 kg ^{232}Th remain clearly detectable. The lower mass targets, the aqueous solutions, also remain detectable in the ^{238}U response although not in the ^{232}Th response. As to concerns for potential application space, consideration of significant target shielding is of clear relevance. However, a significant reduction in the photon flux would be expected to be strongly visible downstream of the target in the case of the presence of significant high-Z target shielding within the interrogation beam.

5.4.3 Direct Comparisons of the Delayed γ-Ray and Delayed Neutron Signal Responses to Shielding

It is useful to directly compare the results of the delayed signature responses to each other. The measured yield responses are indicated, where each delayed signature response has been normalized to the total solid angle subtended the detector array. Figure 5.9 indicates the responses of the metal targets to borated polyethylene for (a) the delayed γ-ray yield responses and (b) the delayed neutron yield responses, shown as a function of the shielding thickness. These figures elucidate the survival of the delayed γ-ray signature, with nearly two orders of magnitude in separation between the depleted uranium target and the lead target at the maximum 30.48 cm of shielding; in contrast, the delayed neutron signature is strongly quenched by the

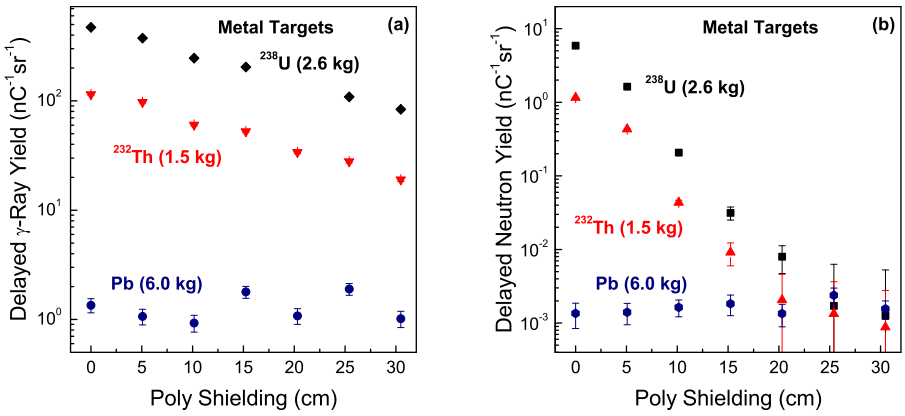

Figure 5.9: A comparison of the delayed signature responses shown as a function of the borated polyethylene shielding thickness for three metal targets, 1.5 kg of ^{232}Th, 2.6 kg of ^{238}U, and a 6.0 kg lead target utilized for active background, indicated for (a) the delayed γ-ray responses and (b) the delayed neutron responses. All yields are normalized to the total acquisition charge and the detector array solid angle; 1σ values are indicated for each measurement. Data was recorded for ∼5 minute inspection windows on each target with beam parameters of 16 MeV and 7.5 Hz.

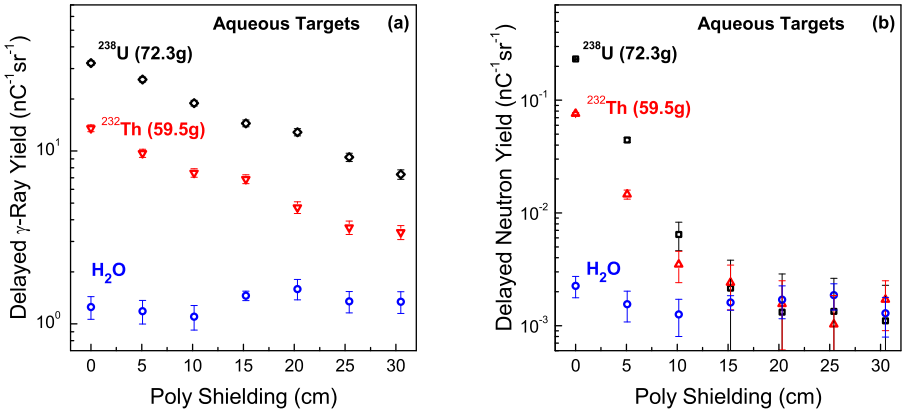

Figure 5.10: A comparison of the delayed signature responses shown as a function of the borated polyethylene shielding thickness for three aqueous targets, 72.3 g of ^{238}U, 59.5 g of ^{232}Th, and a water target utilized for active background, indicated for (a) the delayed γ-ray responses and (b) the delayed neutron responses. All yields are normalized to the total acquisition charge and the detector array solid angle; 1σ values are indicated for each measurement. Data was recorded for ∼5 minute inspection windows on each target with beam parameters of 16 MeV and 7.5 Hz.

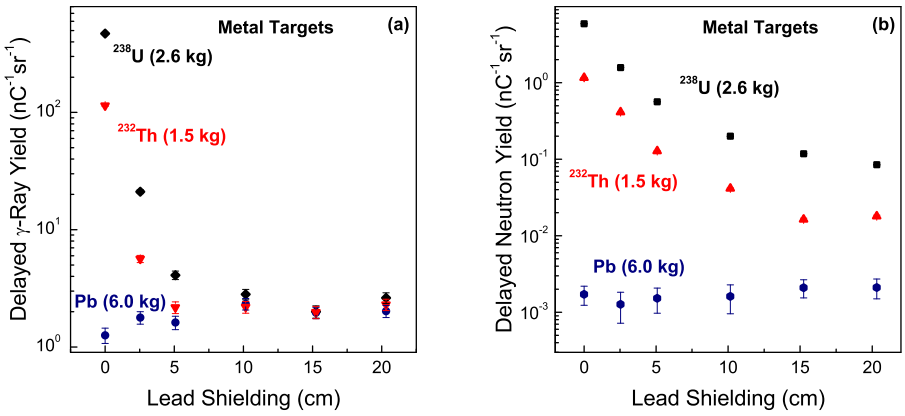

Figure 5.11: A comparison of the delayed signature responses shown as a function of the lead shielding thickness for three metal targets, 1.5 kg of ^{232}Th, 2.6 kg of ^{238}U, and a 6.0 kg lead target utilized for active background, indicated for (a) the delayed γ-ray response and (b) the delayed neutron response. All yields are normalized to the total acquisition charge and the detector array solid angle; 1σ values are indicated for each measurement. Data was recorded for ∼5 minute inspection windows on each target with beam parameters of 16 MeV and 7.5 Hz.

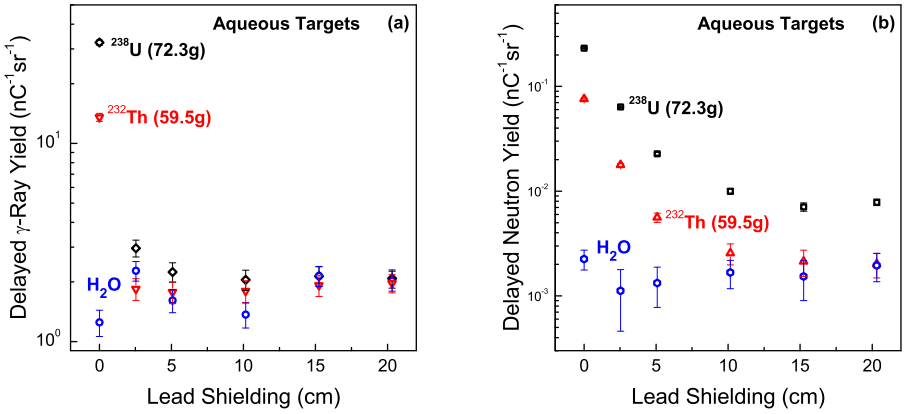

Figure 5.12: A comparison of the delayed signature responses shown as a function of the lead shielding thickness for three aqueous targets, 72.3 g of ^{238}U, 59.5 g of ^{232}Th, and a water target utilized for active background, indicated for (a) the delayed γ-ray response and (b) the delayed neutron response. All yields are normalized to the total acquisition charge and the detector array solid angle; 1σ values are indicated for each measurement. Data was recorded for ∼5 minute inspection windows on each target with beam parameters of 16 MeV and 7.5 Hz.

borated polyethylene shielding. The aqueous target responses show similar qualitative behavior responses; results are shown in Figure 5.10 for the three aqueous targets as a function of the borated polyethylene shielding thickness for (a) the delayed γ-ray yield responses and (b) the delayed neutron yield responses.

Figure 5.11 indicates the responses of the metal targets to lead shielding for (a) the delayed γ-ray yield responses and (b) the delayed neutron yield responses, shown as a function of the target shielding thickness. These figures indicate the detection capability of the delayed neutron response at even 20.32 cm of lead target shielding, where nearly two orders of magnitude of separation are observed between the depleted uranium target yield and the active background lead target yield; in contrast, the delayed γ-ray response decreases rapidly with the first few target shielding steps, and no separation is discernable between the target responses beyond 5.08 cm of shielding. The aqueous target responses show similar qualitative behavior responses; results are shown in Figure 5.12 for the three aqueous targets as a function of the lead shielding thickness for (a) the delayed γ-ray yield responses and (b) the delayed neutron yield responses.

These results highlight the contrasting nature of the two delayed signal responses to the selected shielding materials. For a target shielded by lead, the detection of the fissionable material by delayed γ-ray signal is compromised, but the detection of the material using delayed neutrons survives, even against significant amounts of shielding. Conversely, for a target which is shielded by borated polyethylene, the delayed neutron signal is compromised but the γ-ray signal survives. Thus, the incorporation of both signatures for detection can be leveraged to provide improved detection of fissionable materials.

5.5 Conclusions Regarding the Delayed γ-Ray and Delayed Neutron Signal Responses

It is clear from this investigation that that the delayed γ-ray signature and the delayed neutron signature present nearly orthogonal responses to the selected shielding

materials. Although delayed neutrons and delayed high–energy γ-rays have both been previously studied and are often proposed for detection studies, their complementary nature is not generally considered nor exploited for potential implementation. These results would certainly argue that combined detection utilizing both signatures should be strongly considered as it not only provides dual confirmation of the presence of fissionable material, but may also serve to enhance detection in potentially obscured target scenarios.

Chapter 6

Conclusions

Signatures for the detection and characterization of fissionable materials have been presented. Results were shown for a number of targets, using distinct geometries to investigate several scenarios. Delayed fission neutrons from induced reactions have been shown to be an incredibly effective means to detect the presence of fissionable material, and results were investigated at a number of different bremsstrahlung end point energies. Figure 6.1 illustrates the results of the delayed neutron yields for several small mass aqueous targets utilizing a detection array which was deployed very close to the inspection objects of interest, shown as a function of the bremsstrahlung beam end point energy for interrogation energies from 6 MeV to 19 MeV. The fission rate of the target increases with the congruence of the bremsstrahlung beam energy spectra and the photofission cross section, resulting in the rising delayed neutron responses observed with increasing beam energy. This greatly enhanced delayed neutron yield, which increases by nearly three orders of magnitude from the bremsstrahlung beam end point energies of 6 MeV to 19 MeV, prescribes higher interrogation energies for improved fissionable target response. However, the rapid rise of the response of a water target utilized as active background is noted at the higher bremsstrahlung beam energies; this response is due to a competing reaction on ^{18}O that produces delayed neutrons and which has a threshold energy of 15.9 MeV and. Maintaining the interrogation parameters to avoid production of these non-fission delayed neutrons is crucial to ensuring overall system sensitivity. Thus, an optimal interrogation

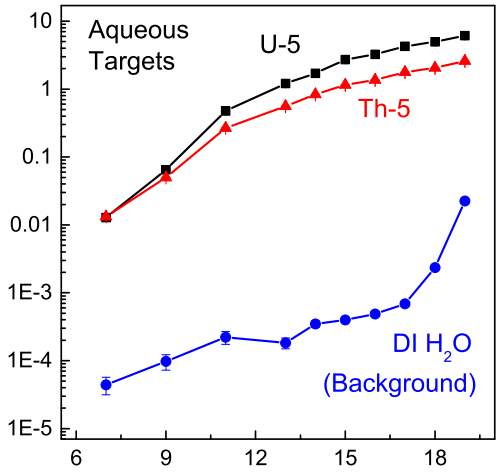

Figure 6.1: The delayed neutron yield for three aqueous targets of interest, U-5, Th-5, and a pure water target utilized for active background measurements, shown as a function of the bremsstrahlung end–point energy for inspections from 6 MeV to 19 MeV. Data was recorded for ∼5 minutes on each target with an accelerator repetition rate of 7.5 Hz.

energy was determined to be 16 MeV. At selected operating parameters of 16 MeV and 7.5 Hz for 5 min inspections, an aqueous target which contained just 52.2 grams of ^{238}U was shown to have a yield a factor of more more than 6671 or 982σ above an active background measurement, while an aqueous target containing just 59.6 grams of ^{232}Th was shown to have a yield a factor of 2811 or 540σ above the measured active background yield; these results infer strong signals of fissionable material and thus incredibly strong detection capabilities.

The time response of the delayed neutron signal was utilized to extrapolate a linearized decay rate of the target, which was shown to be correlated to the fission and neutron emission rates and thus a unique isotopic identifier. The results for a series of aqueous targets of interest are shown in Figure 6.3 The measured linearized decay rates are shown for a ^{238}U target, a ^{232}Th target, and a series of four targets which contained both ^{238}U and ^{232}Th in various combinations; the extrapolated linear decay rates showed strong agreement with the predicted response for any isotopic ratio of ^{238}U and ^{232}Th, indicated as the solid curve in the figure. Although this

approach indicated a strong capacity for the identification of the isotopic composition of targets, it was noted that relatively long inspection times were needed to acquire enough statistics for accurate fits. In the case of these results, target inspection times ∼75 minutes were used for target identification, as opposed to target detection times of just 5 minutes.

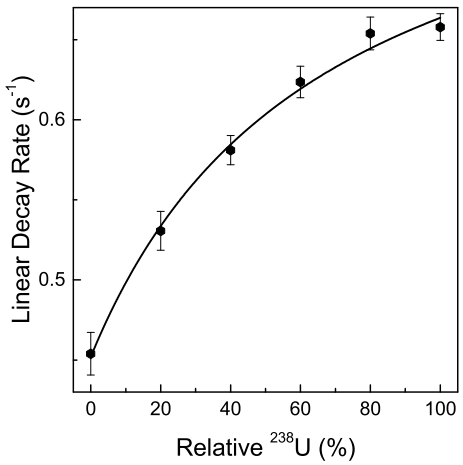

Figure 6.2: The normalized linear decay rates shown as a function of the fraction f of the ^{238}U component for the four silicon oxide mixed component targets and the single component U-6 ^{238}U and Th-6 ^{232}Th targets. The function shown is the predicted linear decay rate for a bi–component solution using the single component decay rate values obtained experimentally; the function form is given by Equation 4.2. Data was collected at 16 MeV at a repetition rate of 7.5 Hz for ∼75 minutes. Least squares linear fits were performed to determine the linear decay rates of the targets; results were summarized in Table 4.7. Error bars indicate 1σ for each target.

An alternative, much more rapid method of identification which utilized the ratio of delayed neutron responses at a standard inspection energy and a lower fiducial inspection energy was defined. The Dual Energy Relative Yield, or DERY value, was defined for these experimental campaigns to be the ratio of the yield from a standard 5 minute inspection at 16 MeV (7.5 Hz) and the yield from a 5 minute inspection at 11 MeV; thus target identification utilizing DERY requires only 10 minutes of total inspection time. Although significantly more scatter was observed in the identification of the isotopic composition of targets utilizing this method, Figure 6.3, the

greatly reduced measurement time still makes DERY a strong candidate, particularly if determining rough isotopic content may be determine further target analysis steps.

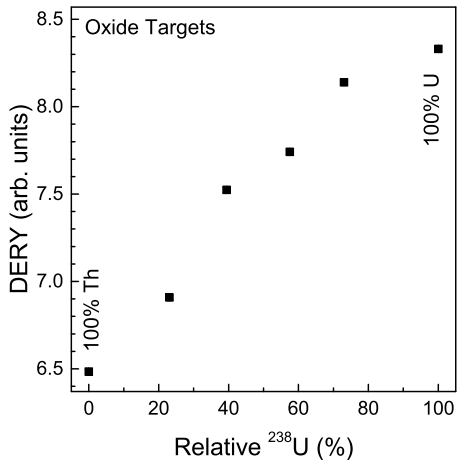

Figure 6.3: The DERY values shown as a function of the fraction f of the ^{238}U component for the four aqueous mixed component targets and the single component U-5 ^{238}U and Th-5 ^{232}Th targets. Data was collected at 11 MeV and 16 MeV at a repetition rate of 7.5 Hz for $\sim$5 minute inspection windows. Least squares linear fits were performed to determine the linear decay rates of the targets; results were summarized in Table 4.6. Error bars indicate 1σ for each target.

Further, the delayed neutron yield response was determined to be linearly correlated to the target fission mass of investigated targets in a mass range up to 150 grams, for both silicon oxide targets and aqueous solutions which contained either ^{238}U or ^{232}Th in varying amounts. Thus, an unknown mass of a target can be extrapolated from the measured delayed neutron yield, allowing further characterization of fissionable material detected. Utilizing either the linearized decay rate or the defined much more rapid Dual Energy Relative Yield (DERY) value to identify the isotope(s) present in an unknown sample, both the isotopic composition and mass of a sample can be deduced.

The sensitivity of the delayed neutron signature's detection capabilities was quantified through the use of minimal detectable mass, or MDM, determined to be directly dependent on the error of a corresponding background measurement for any given

target. Thus the threshold for detection of a system can be thought of as being determined by the fluctuations within the measurement system due to all responses other than those from fission, a logical outcome. In an environment where many neutrons are present at late times in the measurement system, whatever the reason, the detection capability for small masses will be greatly reduced. If however the environment is well-controlled, and very limited background effects are present, the system would be expected to be much more sensitive to small fission masses. Minimal Detectable Mass values were calculated for the measured energy responses for several targets, the results of which are presented in Figure 6.4.

A second signal of fission was identified through the use of high energy delayed γ-rays, defined to be all $E_\gamma \geq 3$ MeV at $t \geq 30$ msec; detection results investigated the parallel signal responses to target shielding utilizing borated polyethylene or lead shielding which surrounded the target on all sides. Results of the inspections are summarized for the delayed neutron detector array and the delayed γ-ray detector array as a function of shielding thickness for the two shielding materials in Figure 6.5 through Figure 6.8.

These results indicate the success of the signals for fission detection, even in cases of significant target shielding. The potential benefits of combined signals as a basis for fissionable material detection are readily apparent.

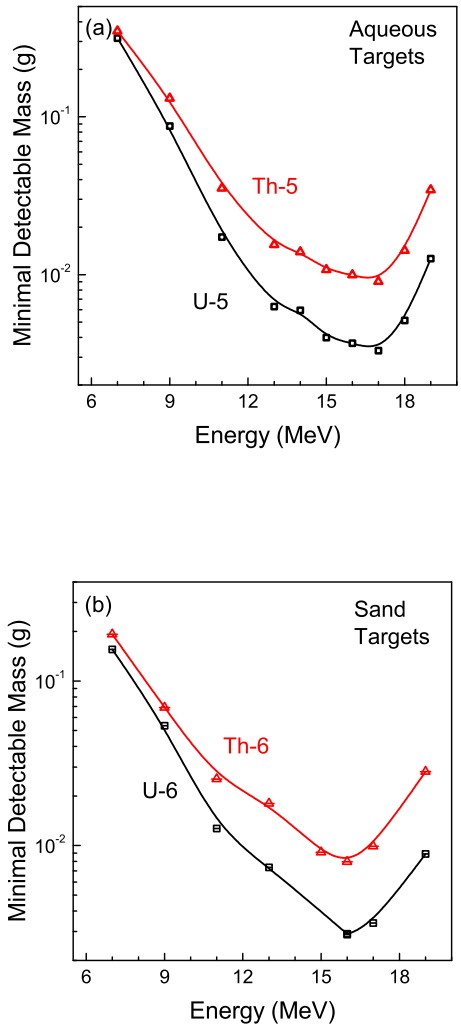

Figure 6.4: The calculated minimal detectable masses are shown as a function of the interrogation energy for (a) the aqueous targets and (b) the oxide targets. Table 4.4 summarized the minimal detectable mass values obtained. The calculations assumed experimental parameters of 7.5 Hz repetition rate with $\sim$ 100 nC charge per pulse for a 5 min inspection. The notable upturn at high energies is due to a competing background reaction and is discussed in detail in the results. The optimal operating energy was chosen to be 16 MeV where the detection thresholds are 9.970 mg for aqueous ^{232}Th, 3.679 mg for aqueous ^{238}U, 7.970 mg for oxide ^{232}Th, and 2.870 mg for oxide ^{238}U.

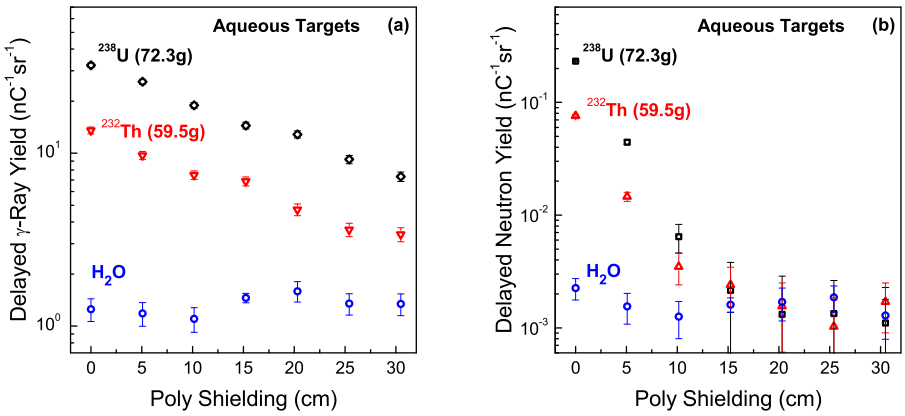

Figure 6.5: A comparison of the delayed signature responses shown as a function of the borated polyethylene shielding thickness for three aqueous targets, 72.3 g of ^{238}U, 59.5 g of ^{232}Th, and a water target utilized for active background, indicated for (a) the delayed γ-ray responses and (b) the delayed neutron responses. All yields are normalized to the total acquisition charge and the detector array solid angle; 1σ values are indicated for each measurement. Data was recorded for $\sim$5 minute inspection windows on each target with beam parameters of 16 MeV and 7.5 Hz.

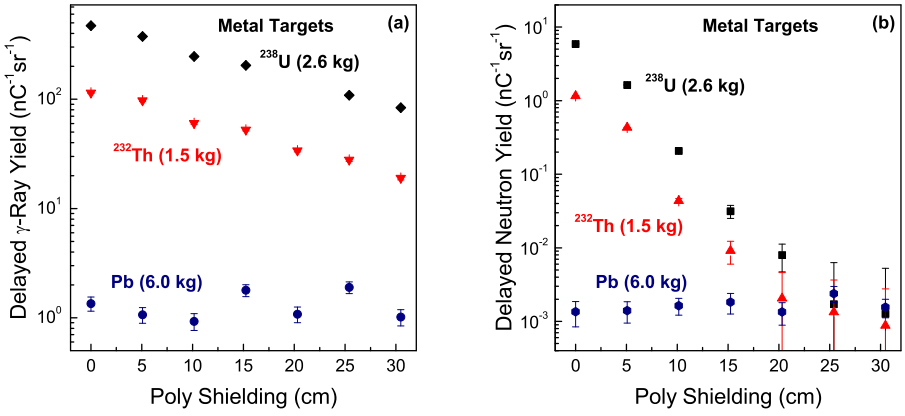

Figure 6.6: A comparison of the delayed signature responses shown as a function of the borated polyethylene shielding thickness for three metal targets, 1.5 kg of ^{232}Th, 2.6 kg of ^{238}U, and a 6.0 kg lead target utilized for active background, indicated for (a) the delayed γ-ray responses and (b) the delayed neutron responses. All yields are normalized to the total acquisition charge and the detector array solid angle; 1σ values are indicated for each measurement. Data was recorded for $\sim$5 minute inspection windows on each target with beam parameters of 16 MeV and 7.5 Hz.

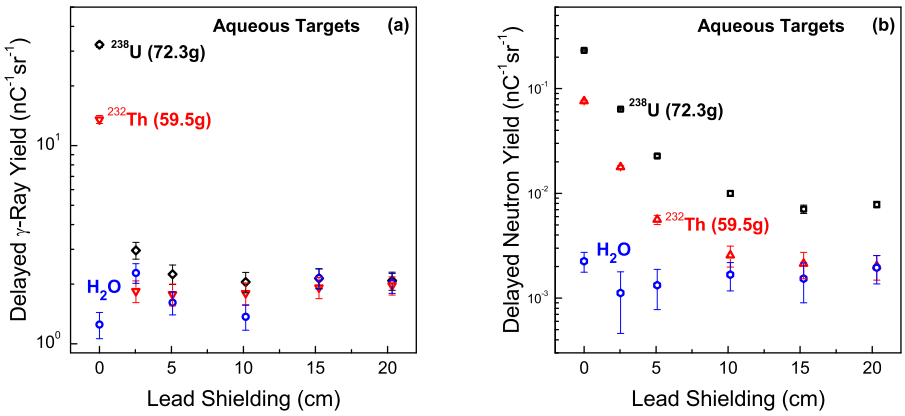

Figure 6.7: A comparison of the delayed signature responses shown as a function of the lead shielding thickness for three aqueous targets, 72.3 g of ^{238}U, 59.5 g of ^{232}Th, and a water target utilized for active background, indicated for (a) the delayed γ-ray response and (b) the delayed neutron response. All yields are normalized to the total acquisition charge and the detector array solid angle; 1σ values are indicated for each measurement. Data was recorded for $\sim$5 minute inspection windows on each target with beam parameters of 16 MeV and 7.5 Hz.

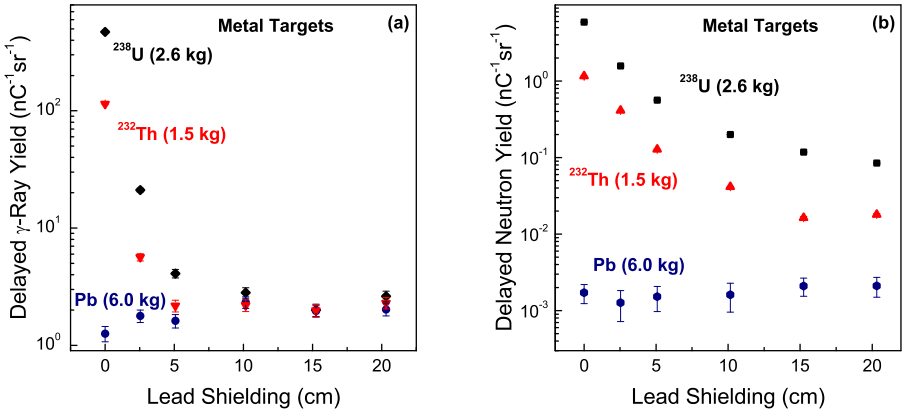

Figure 6.8: A comparison of the delayed signature responses shown as a function of the lead shielding thickness for three metal targets, 1.5 kg of ^{232}Th, 2.6 kg of ^{238}U, and a 6.0 kg lead target utilized for active background, indicated for (a) the delayed γ-ray response and (b) the delayed neutron response. All yields are normalized to the total acquisition charge and the detector array solid angle; 1σ values are indicated for each measurement. Data was recorded for $\sim$5 minute inspection windows on each target with beam parameters of 16 MeV and 7.5 Hz.

Bibliography

[1] Evaluated Nuclear Data File Library ENDF/B-VI.8. Final release October 2001.

[2] R.W. Waldo, R.A. Karam, and R.A. Meyer. Delayed neutron yields: Time dependent measurements and a predictive model. *Phys. Rev. C*, 23(3):1113, 1981.

[3] R.W. Waldo. *A Study of Calculated and Measured Time-Dependent Delayed Neutron Yields*. PhD thesis, Georgia Institute of Technology, 1980.

[4] G. R. Keepin, T. F. Wimett, and R. K. Zeigler. Delayed neutrons from fissionable isotopes of uranium, plutonium, and thorium. *Phys. Rev.*, 107:1044–1049, Aug 1957.

[5] M.C. Brady. *Evaluation and application of delayed neutron precursor data*. PhD thesis, Texas A&M University, 1988.

[6] M. C. Brady and T. R. England. Delayed neutron data and group parameters for 43 fissioning systems. *Nucl. Sci. Eng.*, 103:129, 1989.

[7] L.A. Kull, R.L. Bramblett, T. Gozani, and D.E. Rundquist. Delayed neutrons from low energy photofission. *Nucl. Sci. Eng.*, 39:163, 1970.

[8] D. Doré, J-C. David, M-L. Giacri, J-M. Laborie, X. Ledoux, M. Petit, D. Ridikas, and A. Van Lauwe. Delayed neutron yields and spectra from photofission of actinides with bremsstrahlung photons below 20 mev. *Journal of Physics: Conference Series*, 41(1):241–247, 2006.

[9] M.T. Kinlaw. *Delayed Neutron Group Parameters from Photofission.* PhD thesis, Idaho State University, 2007.

[10] F. Jallu, A. Lyoussi, C. Passard, E. Payan, H. Recroix, G. Nurdin, A. Buisson, and J. Allano. The simultaneous neutron and photon interrogation method for fissile and non-fissile element seperation in radioactive waste drums. *Nucl. Instrum. Methods B*, 170:489, 2000.

[11] A. Lyoussi, J. Romeyer-Dherbey, F. Jallu, E. Payan, A. Buisson, G. Nurdin, and J. Allano. Transuranic waste detection by photon interrogation and on-line delayed neutron counting. *Nucl. Instrum. Methods B*, 160(2):280 – 289, 2000.

[12] D.C. Glasgow. Delayed neutron activation analysis for safeguards. *J. Radioanal. Nucl. Chem.*, 276(1):207–211, 2008.

[13] R.B. Roberts, L.R. Hafstad, R.C. Meyer, and P. Wang. The delayed neutron emission which accompanies fission of uranium and thorium. *Phys. Rev.*, 55:664–664, Apr 1939.

[14] R.B. Roberts, R.C. Meyer, and P. Wang. Further observations on the splitting of uranium and thorium. *Phys. Rev.*, 55:510–511, 1939.

[15] D. Saphier, D. Ilberg, S. Shalev, and S. Yiftah. Evaluated delayed neutron spectra and their importance in reactor calculations. *Nucl. Sci. Eng.*, 62:660–694, 1977.

[16] W.M. Stacey. *Nuclear reactor physics.* John Wiley and Sons, Inc., New York, NY, USA, 2007.

[17] S.T. Hsue, T.W. Crane, W.L. Talbert, and J.C. Lee. *Nondestructive Assay Methods for Irradiated Nuclear Fuels.* Los Alamos Scientific Laboratory, LA–6923, 1978.

[18] C.E. Moss amd C.L. Hollas, G.W. McKinney, and W.L. Myers. Comparison of active interrogation techniques. *IEEE Trans. Nucl. Sci.*, 53(4):2242, 2006.

[19] D.R. Norman, J.L. Jones, W.Y. Yoon, K.J. Haskell, J.W. Sterbentz, J.M. Zabriskie, A.W. Hunt, F. Harmon, and M.T. Kinlaw. Inspection applications with higher electron beam energies. *Nucl. Instrum. Methods B*, 241:787–792, 2005.

[20] J.L. Jones, B.W. Blackburn, S.M. Watson, D.R. Norman, and A.W. Hunt. High-energy photon interrogation for nonproliferation applications. *Nucl. Instrum. Methods B*, 261:326–330, 2007.

[21] B.W. Blackburn, J.L. Jones, C.E. Moss, J.T. Mihalczo, A.W. Hunt, F. Harmon, S.M. Watson, and J.T. Johnson. Utilization of actively-induced, prompt radiation emission for nonproliferation applications. *Nucl. Instrum. Methods B*, 261:341–346, 2007.

[22] I. Gauld and M. Francis. Investigation of passive gamma spectroscopy to verify spent nuclear fuel content. Institute of Nuclear Materials Management, 51^{st} Annual Meeting, January 2010.

[23] P. Blanc, S.J. Tobin, S. Croft, H.O. Menlove, M.T. Swinhoe, and T. Lee. Optimization of the combined delayed neutron and differential die-away prompt neutron signal detection for characterization of spent nuclear fuel assemblies - 11419. Waste Management, WM2011 Annual Symposia, 2011. Also released as LA–UR 10–08013.

[24] M.M. May, R. Abedin-Zadeh, D. Barr, A. Carnesale, P.E. Coyle, J. Davis, W. Dorland, W. Dunlop, S. Fetter, A. Glaser, I.D. Hutcheon, F. Slakey, and B. Tannenbaum. Nuclear forensics: role, state of the art, program needs. Technical report, Nuclear Forensics Working Group of the American Physical Society's Panel on Public Affairs and the American Association for the Advancement of Science, Washington, D.C., 2008.

[25] S. Tobin, H.O. Menlove, D. Bracken, M. Swinhoe, H. Trellue, L.W. Campbell, B. Castle, M. Humphrey, B. Broadhead, A. Belian, et al. Update on the next

generation safeguard initiative project to determine Pu mass in spent fuel assemblies. Institute of Nuclear Materials Management, 53^{rd} Annual Meeting, July 2012. Also released as LA–UR–12–25113.

[26] I.C. Gauld, S.M. Bowman, B.D. Murphy, and P. Schwalbach. Applications of ORIGEN to spent fuel safeguards and non-proliferation. Institute of Nuclear Materials Management, 47^{th} Annual Meeting, July 2006.

[27] M. Tarvainen, L. Ferenc, T.E. Valentine, M. Abhold, and B. Moran. NDA techniques for spent fuel verification and radiation monitoring. Technical report, Finland Radiation and Nuclear Safety Authority (STUK), STUK-YTO-TR 133, August 1997, August 1997.

[28] V. Henzl, H.O. Menlove, and J. Thron. Differential die-away self-interrogation for treaty verification applications. Technical report, Los Alamos National Laboratory (LANL), LA–UR–12–26232, 2012.

[29] S.L. Stewart. *Investigating Correlated Neutrons from Pulsed Photonuclear Interrogation for Treaty Verification Applications.* PhD thesis, Texas A&M University, 2013.

[30] J. Brennan, R. Cooper, M. Gerling, P. Marleau, N. Mascarenhas, and S. Mrowka. Applying the neutron scatter camera to treaty verification and warhead monitoring. In *IEEE 2010 NSS/MIC Conf. Pub.*, volume 1, pages 691–694. IEEE Nuclear Science Symposium & Medical Imaging Conference (NSS/MIC), December 2010.

[31] D.E. Archer, C.L. Britton Jr., R.J. Carter, R.F. Lind, J.T. Mihalczo, J.A. Mullens, J.E. Radle, and M.C. Wright. Fieldable nuclear material identification system. Institute of Nuclear Materials Management, 51^{st} Annual Meeting, 2010.

[32] D.L. Chichester, J.T. Johnson, and E.H. Seabury. High-resolution fast-neutron spectrometry for arms control and treaty verification. Institute of Nuclear Materials Management, 53^{rd} Annual Meeting, Jul 2012. Also Released as INL/CON–12–24554.

[33] R.A. August, G.W. Phillips, S.E. King, and J.H. Cutchin. Neutron signatures' [weapons treaty verification]. 1992 IEEE Nuclear Science Symposium and Medical Imaging Conference (NSS/MIC). *IEEE Trans. Nucl. Sci.*, 40(4):114–116, 1992.

[34] U.S. Department of State Bureau of Arms Control, Verification, Compliance: Office of Verification, Planning, and Outreach (AVC/VPO). 2015 Verification technology research and development needs. Available online, http://www.state.gov/documents/organization/216413.pdf. Last accessed: September 2015.

[35] IAEA Incident and Trafficking Database (ITDB): Incidents of nuclear and other radioactive material out of regulatory control Fact Sheet 2013. International Atomic Energy Agency, 2013.

[36] U.S. Department of Transportation, Research and Innovative Technology Administration, Bureau of Transportation Statistics. America's Container Ports: Linking markets at home and abroad. Technical report, January 2011. Available online, http://www.bts.gov/publications/americas_ container_ ports/2011/. Last accessed: September 2015.

[37] "Implementing Recommendations of the 9/11 Commission Act of 2007", Public Law 110–53, Section 1701, 121 Statute 489, August 2007.

[38] IAEA Safeguards Glossary, 2001 Edition: International Nuclear Verification Series No. 3. Technical report, International Atomic Energy Agency, Vienna, Austria, 2002.

[39] J. Medalia. Detection of Nuclear Weapons and Materials: Science, Technologies, Observations. Technical report, Congressional Research Service (CRS) Report for Congress, 2010.

[40] R.C. Lanza. Homeland security and contraband detection. In H.Z. Bilheux, R. McGreevy, and I.S. Anderson, editors, *Neutron Imaging and Applications*,

Neutron Scattering Applications and Techniques, pages 319 – 338. Springer, U.S., 2009.

[41] R.T. Kouzes, E.R. Siciliano, J.H. Ely, P.E. Keller, and R.J. McConn. Passive neutron detection for interdiction of nuclear material at borders. *Nucl. Instrum. Methods A*, 584(23):383 – 400, 2008.

[42] D.R. Slaughter, M.R. Accatino, A. Bernstein, P. Biltoft, J.A. Church, M.A. Descalle, J.M. Hall, D.R. Manatt, G.J. Mauger, T.L. Moore, et al. The nuclear car wash: A system to detect nuclear weapons in commercial cargo shipments. *Nucl. Instrum. Methods A*, 579(1):349–352, 2007.

[43] J.L. Jones, K.J. Haskell, J.M. Hoggan, D.R. Norman, and W.Y. Yoon. Photonuclear-based detection of nuclear smuggling in cargo containers. 17^{th} Int. Conf. Appl. Accs. Res. Ind. (CAARI). *AIP Conf. Proc.*, 680(1):947–952, 2003.

[44] W. Bertozzi and R.J. Ledoux. Nuclear resonance fluorescence imaging in non-intrusive cargo inspection. *Nucl. Instrum. Methods B*, 241(1):820–825, 2005. The Application of Accelerators in Research and IndustryProceedings of the Eighteenth International Conference on the Application of Accelerators in Research and Industry (CAARI 2004)Eighteenth International Conference on the Application of Accelerators in Research and Industry.

[45] C.E. Moss, C.A. Goulding, C.L. Hollas, and W.L. Myers. Linear accelerator-based active interrogation for detection of highly enriched uranium. 17^{th} Int. Conf. Appl. Accs. Res. Ind. (CAARI). *AIP Conf. Proc.*, 680(1):900–904, 2003.

[46] K.A. Jordan and T. Gozani. Pulsed neutron differential die away analysis for detection of nuclear materials. *Nucl. Instrum. Methods B*, 261(12):365 – 368, 2007. Proceedings of the Nineteenth International Conference on The Application of Accelerators in Research and Industry.

[47] C. Hill, J. O'Malley, P. Martin, K. Marshall, R. Maddock, J. Threadgold, R. Commisso, S.L. Jackson, J. Schumer, B. Phlips, P. Ottinger, D. Mosher,

J. Apruzese, F. Young, and J. Davis. Active detection of special nuclear material – Recommendations for interrogation source approach for UK prototype active detection system. In *IEEE 2012 NSS/MIC Conf. Pub.*, pages 732–737. IEEE Nuclear Science Symposium and Medical Imaging Conference (NSS/MIC), Oct 2012.

[48] C.L. Morris, C.C. Alexander, J.D. Bacon, K.N. Borozdin, D.J. Clark, R. Chartrand, C.J. Espinoza, A.M. Fraser, M.C. Galassi, J.A. Green, J.S. Gonzales, J.J. Gomez, N.W. Hengartner, G.E. Hogan, A.V. Klimenko, M.F. Makela, P. McGaughey, J.J. Medina, F.E. Pazuchanics, W.C. Priedhorsky, J.C. Ramsey, A. Saunders, R.C. Schirato, L.J. Schultz, M.J. Sossong, and G.S. Blanpied. Tomographic imaging with cosmic ray muons. *Science & Global Security*, 16(1-2):37–53, 2008.

[49] S. Riggi, V. Antonuccio, M. Bandieramonte, U. Becciani, F. Belluomo, M. Belluso, S. Billotta, G. Bonanno, B. Carbone, A. Costa, G. Fallica, V. La Monaca, P. La Rocca, E. Leonora, F. Longhitano, D. Lo Presti, P. Massimino, M. Mazzillo, G.S. Pappalardo, C. Petta, A. Piana, C. Pistagna, C. Pugliatti, M. Puglisi, N. Randazzo, F. Riggi, S. Riggi, G.V. Russo, D. Sanfilippo, G. Santagati, G. Valvo, and A. Zaia. A large area cosmic ray detector for the inspection of hidden high-z materials inside containers. 23^{rd} Eur. Cosmic Ray Symp. (ECRS). *J. Phys. Conf. Ser.*, 409(1):012046, 2013.

[50] U.S. Customs and Border Protection. Radiation portal monitors safeguard America from nuclear devices and radiological materials. http://www.cbp.gov/border-security/port-entry/cargo-security/cargo-exam/rad-portal1. Last Accessed: September 2015.

[51] U.S. Department of State Office of Second Line of Defense. Partnership Opportunities [*Briefing, August 2012*]. Available online, http://www.state.gov/documents/organization/202453.pdf. Last Accessed: September 2015.

[52] R.T. Kouzes. Detecting Illicit Nuclear Materials: The installation of radiological monitoring equipment in the United States and overseas is helping thwart nuclear terrorism. *Amer. Sci.*, 93(5):422 – 427, 2005.

[53] Department of Homeland Security (DHS): DHS health and safety report on Non-Intrusive Imaging (NII) container scanning technology. Technical report, Prepared by Domestic Nuclear Detection Office and U.S. Customs and Border Protection, July 2007. Available online, http://www.aapaports.org/files/PDFs/NII Health and Safety Report to Congress 7 6 2007 - Final.pdf. Last Accessed: August 2015.

[54] G. Janssens-Maenhout, F. De Roo, and W. Janssens. Contributing to shipping container security: can passive sensors bring a solution? *J. Environ. Radioact.*, 101:95–105, 2010.

[55] R.C. Runkle, A. Bernstein, and P.E. Vanier. Securing special nuclear material: Recent advances in neutron detection and their role in nonproliferation. *J. Appl. Phys.*, 108(111101):1 – 21, 2010.

[56] Presidential Report on Radiation Protection Advice: Screening of Humans for Security Purposes Using Ionizing Radiation Scanning Systems. Technical Report SC 01-12, National Council on Radiation Protection, 2003.

[57] National Council on Radiation Protection and Measurements (NCRP). Limitation of exposure to ionizing radiation. NCRP Report No. 116, 1993. Supersedes NCRP Report No. 91.

[58] National Council on Radiation Protection and Measurements (NCRP). Radiological health protection issues associated with use of active detection technology systems for detection of radioactive threat materials. NCRP Commentary No. 22, 2011.

[59] International Commission on Radiation Protection (ICRP). Individual monitoring for intakes of radionuclides by workers. *Ann. ICRP*, 19(1-3), 1989. Also released as ICRP Publication 54. Superseded by ICRP Publication 78.

[60] International Commission on Radiation Protection. Individual monitoring for internal exposure of workers (preface and glossary missing). *Ann. ICRP*, 27(3-4), 1997. Also released as ICRP Publication 78.

[61] D.A. Cool, E. Lazo, P. Tattersall, G. Simeonov, and S. Niu. Radiological protection in security screening. *Ann. ICRP*, 43(2), 2014. Also released as ICRP Publication 125.

[62] U.S. Customs and Border Protection. Container Security Initiative (CSI). http://www.cbp.gov/border-security/ports-entry/cargo-security/csi/csi-brief. Last Accessed: September 2015.

[63] M.F. James. Energy released in fission. *J. Nucl. Energy*, 23(9):517 – 536, 1969.

[64] Tsien San-Tsiang, Ho Zah-Wei, R. Chastel, and L. Vigneron. On the new fission processes of uranium nuclei. *Phys. Rev.*, 71:382–383, Mar 1947.

[65] C.A. Bertulani and P. Danielewicz. *Introduction to Nuclear Physics*. Graduate Student Series in Physics. Institute of Physics Publishing, 2004.

[66] K.S. Krane. *Introductory Nuclear Physics*. Wiley, 1988.

[67] H.A. Bethe and R.F. Bacher. Nuclear physics a. stationary states of nuclei. *Rev. Mod. Phys.*, 8(2):82–229, April 1936.

[68] E.T.E. Reedy. Discrete γ–rays from photofission for nuclear forensics applications. Master's thesis, Idaho State University, 2011.

[69] M.T. Kinlaw and A.W. Hunt. Fissionable isotope identification using the time dependence of delayed neutron emission. *Nucl. Instrum. Methods A*, 562(2):1081–1084, 2006.

[70] D.J. Loaiza and F.E. Haskin. Dominant delayed neutron precursors to model reactivity predictions for multiple fissioning nuclides. *Nucl. Sci. Eng.*, 134(1):22–36, 2000.

[71] E.L. Chu and L.I. Schiff. Recent progress in accelerators. *Annu. Rev. Nucl. Sci.*, 2(1):79–92, 1953.

[72] K. Strauch. Recent studies of photonuclear reactions. *Annu. Rev. Nucl. Sci.*, 2(1):105–128, 1953.

[73] L. Katz, T. M. Kavanagh, A. G. W. Cameron, E. C. Bailey, and J. W. T. Spinks. Photofission of ^{238}U. *Phys. Rev.*, 99:98–106, Jul 1955.

[74] H.A. Bethe and L.C. Maximon. Theory of bremsstrahlung and pair production. I. Differential cross section. *Phys. Rev.*, 93:768–784, Feb 1954.

[75] Y.S. Tsai and Van Whitis. Thick-target bremsstrahlung and target considerations for secondary-particle production by electrons. *Phys. Rev.*, 149:1248–1257, Sep 1966.

[76] B. Pfeiffer, K.-L. Kratz, and P. Möller. Status of delayed-neutron precursor data: Half-lives and neutron emission probabilities. *Prog. Nucl. Energy*, 41(1):39–69, 2002.

[77] D. Loaiza and F.E. Haskin. Observations regarding fixed decay constants on the reactivity prediction for the fast fission of ^{235}U. 1997 ANS Winter Meeting. *Trans. Am. Nucl. Soc.*, 77:392 – 394, 1997.

[78] J. Svarny. Information about the new 8-group delayed neutron set preparation. In *Proc. 8^{th} Atom. Energy Res. Symp. (AER)*, page 143, 1998.

[79] G. Rudstam, Ph. Finck, A. Filip, A. DAngelo, R.D. McKnight, and J. Svarny. Delayed neutron data for the major actinides. Technical report, Nuclear Energy Agency, Working Party on International Evaluation Cooperation Volume 6: Report NEA/WPEC–6, 2002.

[80] D.J. Loaiza and E. Haskin. Technique for the identification of dominant delayed neutron precursors. Technical report, Los Alamos National Laboratory (LANL), LA–UR–01–6612, prepared for PHYSOR 2002 Int. Conf., 2001.

[81] R. J. Tuttle. Delayed-neutron data for reactor-physics analysis. *Nucl. Sci. Eng.*, 56:37, 1975.

[82] L.A. Currie. Limits for qualitative detection and quantitative determination. *Anal. Chem.*, 40(3):586–593, 1968.

[83] G.F. Knoll. *Radiation detection and measurement.* John Wiley and Sons, Inc., New York, NY, USA, 2000.

[84] L.A. Currie. Detection and quantification limits: origins and historical overview. *Anal. Chim. Acta*, 391(2):127–134, 1999.

[85] M.M.R. Williams. *The slowing down and thermalization of neutrons.* John Wiley and Sons, Inc., New York, NY, USA, 1966.

[86] T.W. Bonner. Collisions of neutrons with atomic nuclei. *Phys. Rev.*, 45(9):601–607, May 1934.

[87] E. Fermi. Radioattivit indotta dal bombardamento di neutroni. *La Ricerca Scientifica*, 5:282, 1934.

[88] E. Fermi. Radioactivity induced by neutron bombardment. *Nature*, 133(3368):757, May 1934.

[89] E. Amaldi and E. Fermi. On the absorption and the diffusion of slow neutrons. *Phys. Rev.*, 50:899, 1936.

[90] J.R. Dunning and G.B. Pegram. Scattering and absorption of neutrons. *Phys. Rev.*, 43:497–498, March 1933.

[91] J.R. Dunning. The emission and scattering of neutrons. *Phys. Rev.*, 45:586–600, May 1934.

[92] G. Breit and E. Wigner. Capture of slow neutrons. *Phys. Rev.*, 49:519–531, April 1936.

[93] M.T. Kinlaw and A.W. Hunt. Time dependence of delayed neutron emission for fissionable isotope identification. *Appl. Phys. Lett.*, 86:254104, 2005.

[94] J.M. Hall, S. Asztalos, P. Biltoft, J. Church, M.-A. Descalle, T. Luu, D. Manatt, G. Mauger, E. Norman, D. Petersen, et al. The nuclear car wash: Neutron interrogation of cargo containers to detect hidden SNM. *Nucl. Instrum. Methods B*, 261(1):337–340, 2007.

[95] S.E. Derenzo, M.J. Weber, E. Bourret-Courchesne, and M.K. Klintenberg. The quest for the ideal inorganic scintillator. *Nucl. Instrum. Methods A*, 505(1-2):111–117, 2003.

[96] E.S. Cárdenas. Detection of delayed gamma rays using $Bi_4Ge_3O_{12}$ and NaI(TI) detectors for the identification of fissionable materials. Master's thesis, Idaho State University, 2009.

[97] E.T.E. Reedy, S.J. Thompson, and A.W. Hunt. The detection of delayed γ-rays between intense bremsstrahlung pulses for discriminating fissionable from non-fissionable materials. *Nucl. Instrum. Methods A*, 606(3):811–815, 2009.

[98] E.S. Cárdenas, E.T.E. Reedy, H.A. Seipel, B.H. Failor, and A.W. Hunt. Comparison of fission signatures from β-delayed γ-ray and neutron emissions. *Nucl. Instrum. Methods A*, 792:67–73, 2015.

[99] J.G. Kavouras. Detection and simulation of delayed γ-rays from photofission. Master's thesis, The University of Utah, 2014.

[100] J.H. Hubbell and S.M. Seltzer. Tables of x-ray mass attenuation coefficients and mass energy-absorption coefficients 1 kev to 20 MeV for elements Z=1 to 92 and 48 additional substances of dosimetric interest. Technical report, National Inst. of Standards and Technology, Ionizing Radiation Div., Gaithersburg, MD (United States), 1995.